Soft Lithography
Micro- and Nanofluidic

Lab-on-a-Chip

Soft Lithography

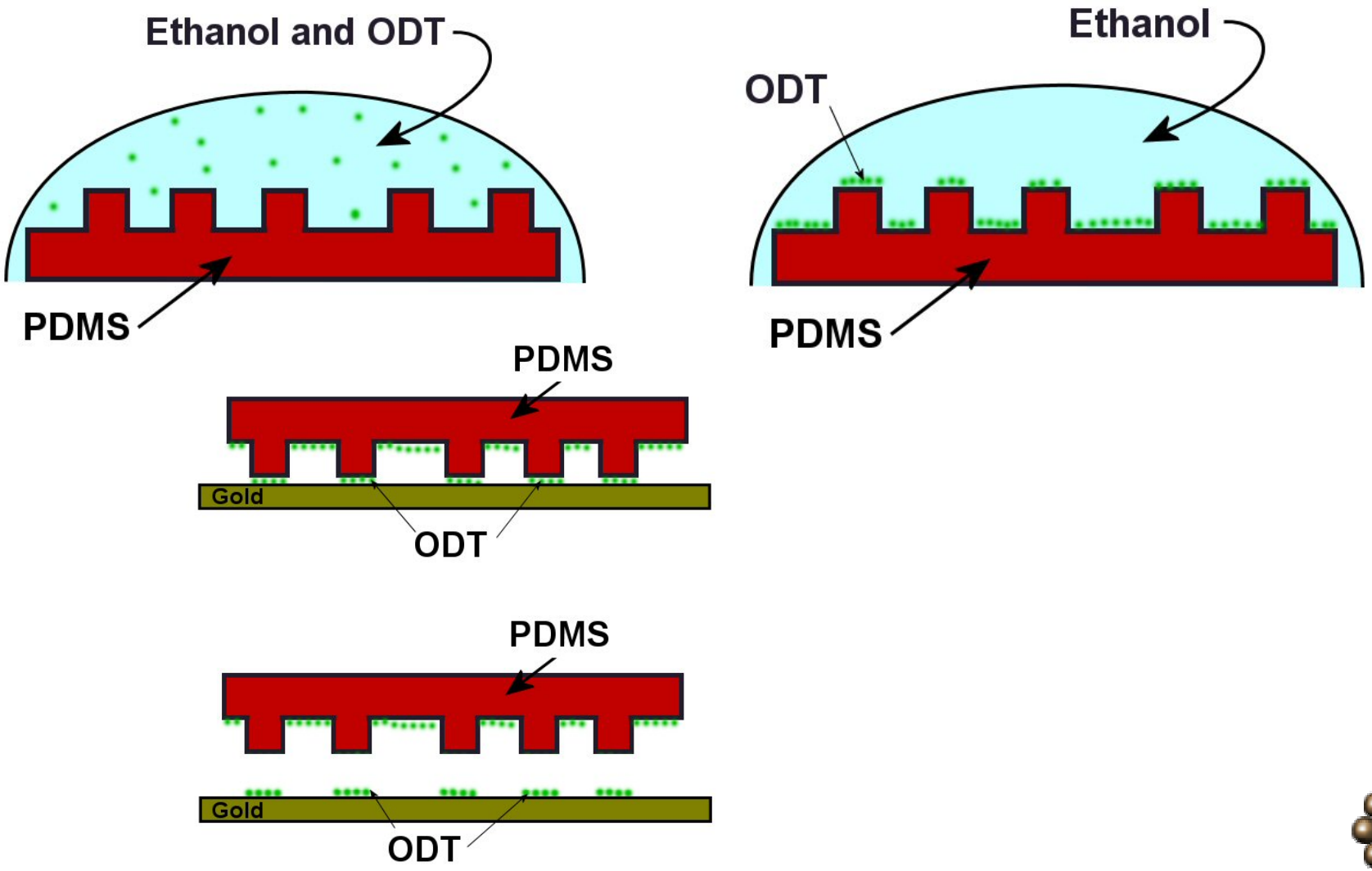

Table 1 Comparison between photolithography and soft lithography

	Photolithography	Soft lithography
Definition of patterns	Rigid photomask (patterned Cr supported on a quartz plate)	Elastomeric stamp or mold (a PDMS block patterned with relief features)
Materials that can be patterned directly	Photoresists (polymers with photo-sensitive additives)	Photoresists[a,e]
	SAMs on Au and SiO_2	SAMs on Au, Ag, Cu, GaAs, Al, Pd, and SiO_2[a] Unsensitized polymers[b–e] (epoxy, PU, PMMA, ABS, CA, PS, PE, PVC) Precursor polymers[c,d] (to carbons and ceramics) Polymer beads[d] Conducting polymers[d] Colloidal materials[a,d] Sol-gel materials[c,d] Organic and inorganic salts[d] Biological macromolecules[d]
Surfaces and structures that can be patterned	Planar surfaces 2-D structures	Both planar and nonplanar Both 2-D and 3-D structures
Current limits to resolution	~250 nm (projection) ~100 nm (laboratory)	~30 nm[a,b], ~60 nm[e], ~1 μm[d,e] (laboratory)
Minimum feature size	~100 nm (?)	10 (?) - 100 nm

[a–e]Made by (a) μCP, (b) REM, (c) μTM, (d) MIMIC, (e) SAMIM. PU:polyurethane; PMMA: poly(methyl methacrylate); ABS: poly(acrylonitrile-butadiene-styrene); CA: cellulose acetate; PS: polystyrene; PE: polyethylene; and PVC: poly(vinyl chloride)

Soft Lithography

Annu. Rev. Mater. Sci. 1998. 28:153–84

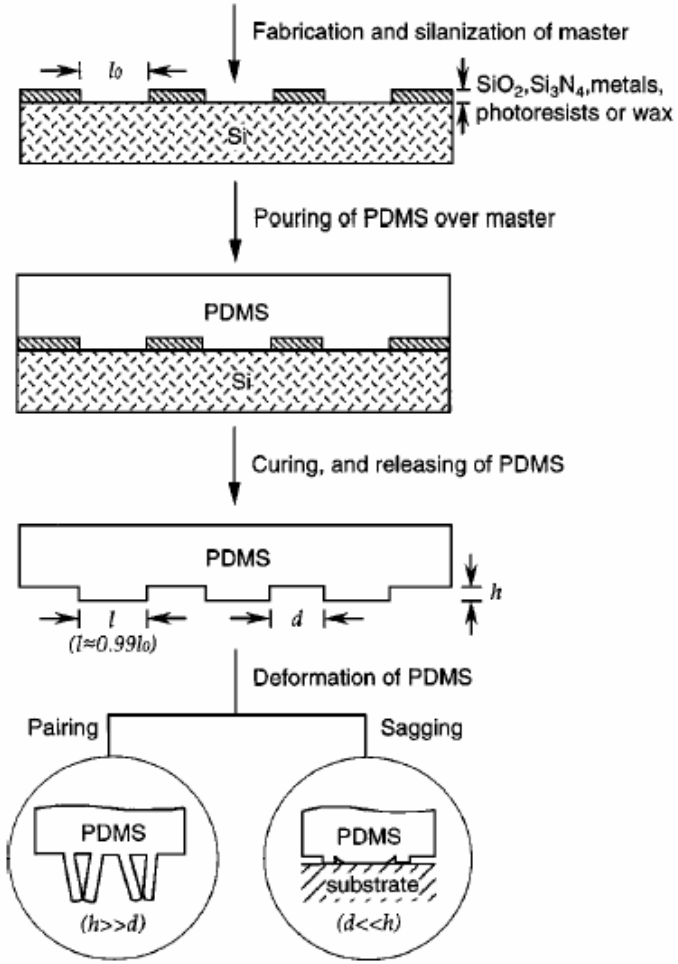

Micro-contact Printing

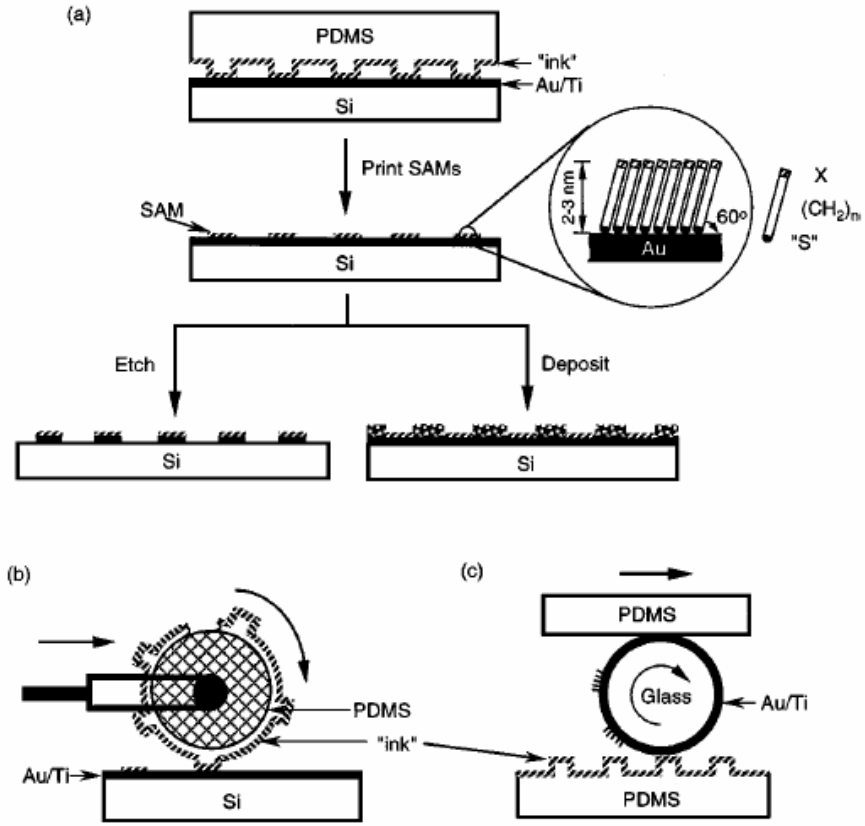

Figure 2 Schematic procedures for μCP of hexadecanethiol (HDT) on the surface of gold: (*a*) printing on a planar surface with a planar stamp (21), (*b*) printing on a planar surface over large areas with a rolling stamp (128), and (*c*) printing on a nonplanar surface with a planar stamp (174).

Micro-contact Printing

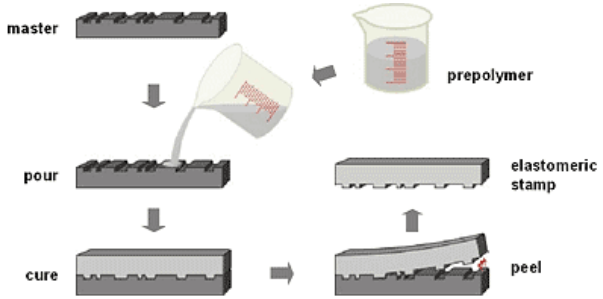

Fig.2 The stamp replication process: A master with a negative of the desired pattern is cast with a pre-polymer. After curing the polymer, the elastomeric stamp is peeled off the master and ready for microcontact printing.

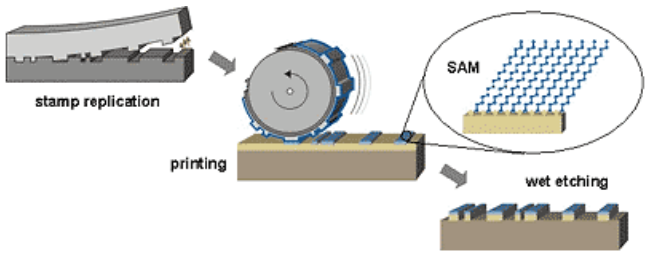

Fig.1 The microcontact printing (μCP) process: An elastomeric stamp is replicated from a master. After inking of the stamp with a suitable ink, it is fixated on a printing machine with help of which it is brought into conformal contact with a substrate. There the ink forms a self-assembled monolayer (SAM) which can be used as a resist in a subsequent wet etching step.

Micro-contact Printing

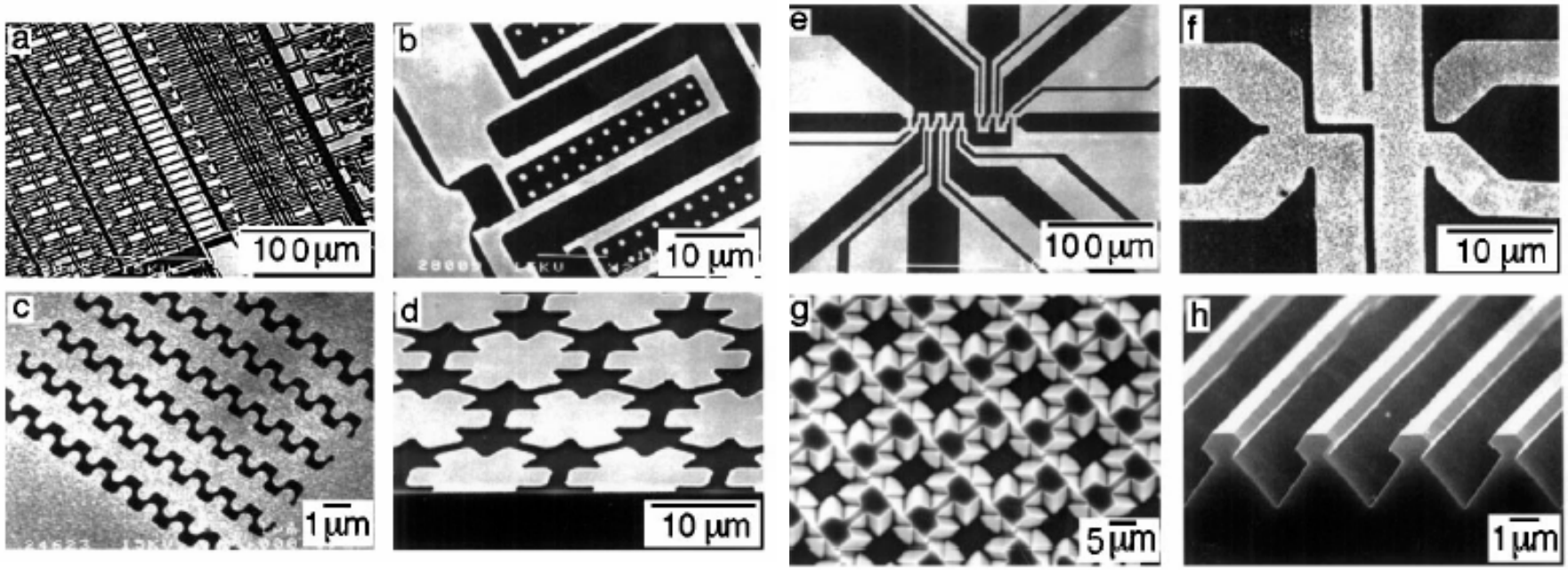

Self-Assemble Monolayer (SAM)

Chem. Rev. **2005**, *105*, 1103–1169

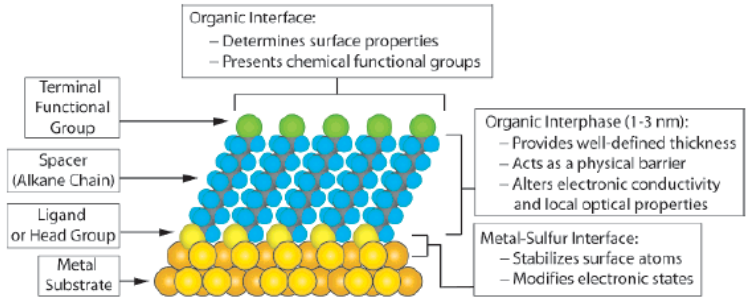

Ligand	Substrates	Morphology of Substrate: Thin Films or Bulk Material	Morphology of Substrate: Nanoparticles or Other Nanostructures
ROH	Fe_xO_y		35
	Si-H	36	
	Si	37	
RCOO-/RCOOH	α-Al_2O_3	38,39	
	Fe_xO_y		40
	Ni		41,42
	Ti/TiO_2	43	
RCOO–OOCR	Si(111):H	44	
	Si(100):H		
Ene-diol	Fe_2O_3		45
RNH_2	FeS_2	46	
	Mica	47	
	Stainless Steel 316L	48	
	$YBa_2Cu_3O_{7-\delta}$	49	
	CdSe		50
RC≡N	Ag	51	
	Au		
R-N≡N$^+$(BF_4^-)	GaAs(100)	52	
	Pd	52	
	Si(111):H	52	
RSH	Ag	26	53,54
	$Ag_{90}Ni_{10}$	55	
	AgS		56
	Au	26	57
	AuAg		58
	AuCu		58
	Au_xPd_{1-x}		58
	CdTe		59
	CdSe		60
	CdS		61,62
	Cu	26	58
	FePt		63-66
	GaAs	67	
	Ge	68	
	Hg	69-71	
	HgTe		72
	InP	73	
	Ir		74
	Ni	75	
	PbS		76-78
	Pd	30	74,79
	PdAg		58
	Pt	32	80
	Ru		81
	Stainless Steel 316L	48	
	$YBa_2Cu_3O_{7-\delta}$	82	
	Zn	83	
	ZnSe	84	
	ZnS		85
RSAc	Au	86	
	Au		87
R–S			
RSR'	Au	88	

Ligand	Substrates	Morphology of Substrate: Thin Films or Bulk Material	Morphology of Substrate: Nanoparticles or Other Nanostructures
RSSR'	Ag	89	90
	Au	20	90-92
	CdS		61
	Pd	30	
	Au	93	
R–S–S			
RCSSH	Au	94	
	CdSe		95
$RS_2O_3^-Na^+$	Au	96	98
	Cu	97	
RSeH	Ag	99	
	Au	100,101	
	CdS		60
	CdSe		102
RSeSeR'	Au	101	
R_3P	Au		103
	FeS_2	46	
	CdS		104
	CdSe		104
	CdTe		104
$R_3P=O$	Co		105,106
	CdS		104
	CdSe		104
	CdTe		104
$RPO_3^{2-}/RP(O)(OH)_2$	Al	107	
	Al-OH	108	
	$Ca_{10}(PO_4,CO_3)_6(OH)_2$	109	
	GaAs	110	
	GaN	110	
	Indium tin oxide (ITO)	111	
	Mica	112	
	TiO_2	113,114	
	ZrO_2	114,115	
	CdSe		116-118
	CdTe		118,119
RPO_4^{2-}	Al_2O_3	120	
	Nb_2O_5	120	
	Ta_2O_3	121	
	TiO_2	120,122	
RN≡C	Pt	123	124
$RHC=CH_2$	Si	37	
RC≡CH	Si(111):H	125	
$RSiX_3$ X = H, Cl, OCH_2CH_3	HfO_2	126	
	ITO	127	
	PtO	128	
	TiO_2	113,126,129	
	ZrO_2	126,129	

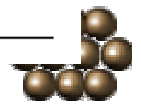

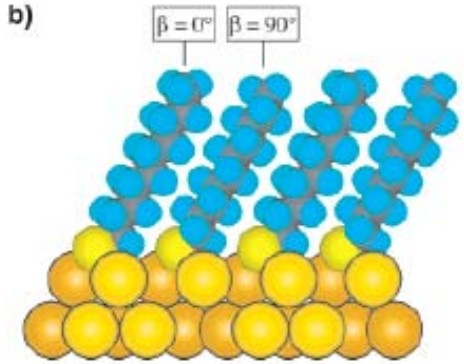

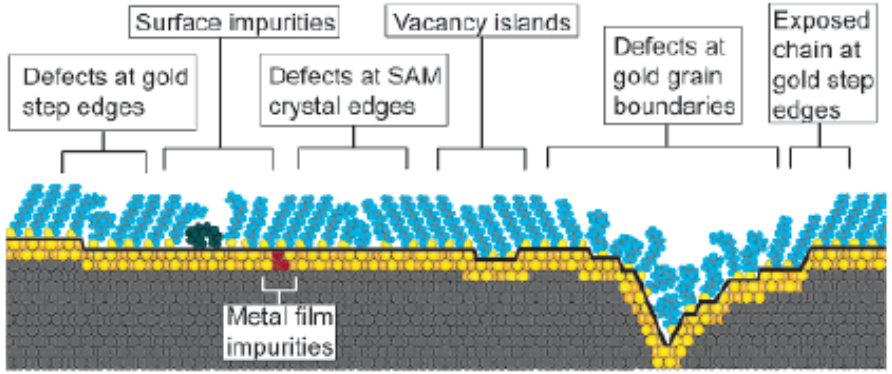

Figure 7. Schematic illustration of some of the intrinsic and extrinsic defects found in SAMs formed on polycrystalline substrates. The dark line at the metal−sulfur interface is a visual guide for the reader and indicates the changing topography of the substrate itself.

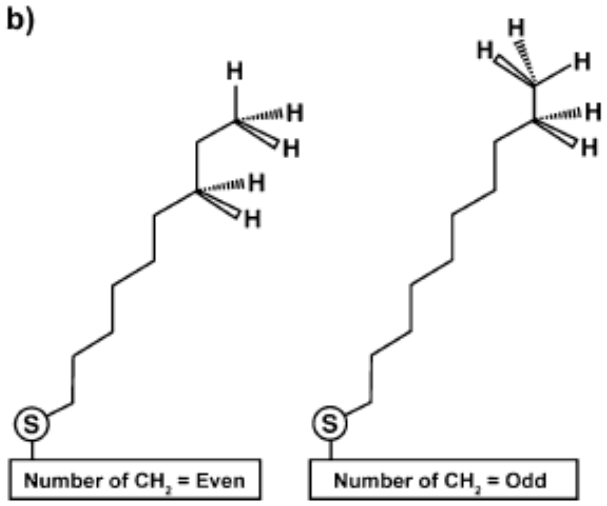

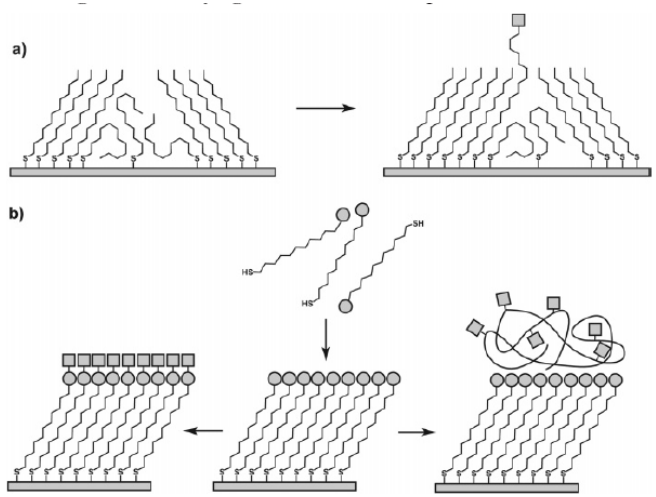

[c] (a) Insertion of a functional adsorbate at a defect site in a preformed SAM. (b) Transformation of a SAM with exposed functional groups (circles) by either chemical reaction or adsorption of another material.

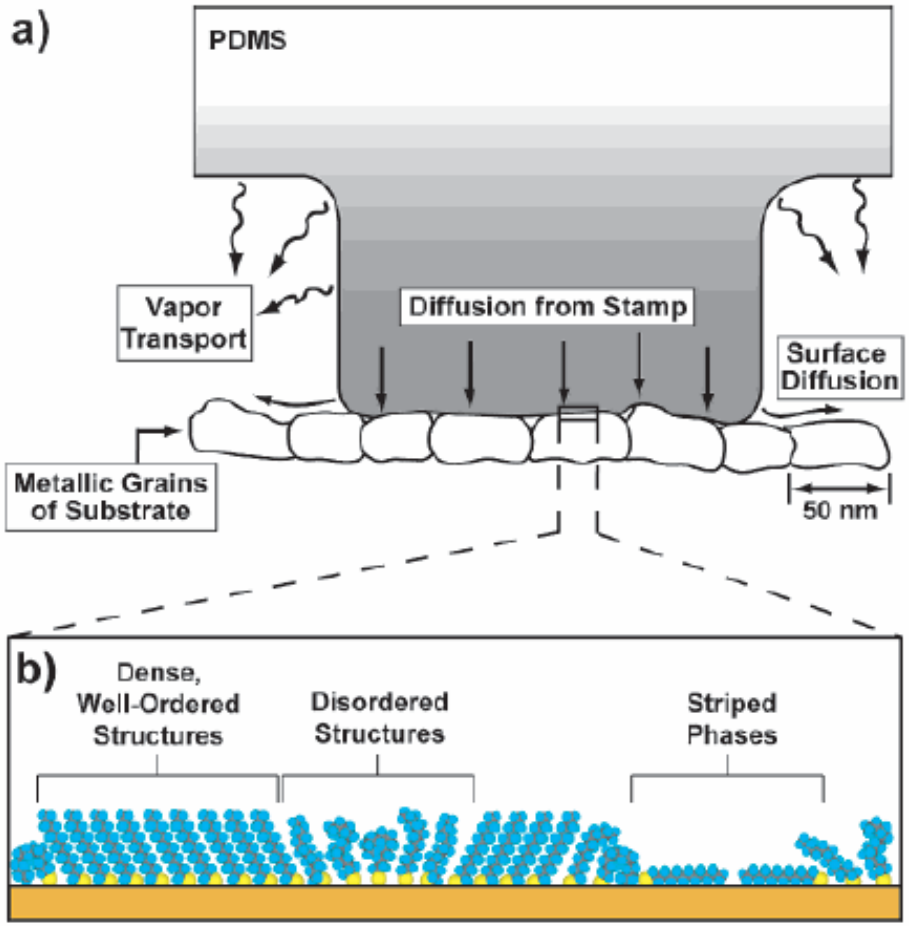

Figure 12. (a) Schematic illustration depicting the application of a PDMS stamp containing thiols to a polycrystalline metal film. The primary mechanisms of mass transport from the stamp to the surface are shown. The grayscale gradient approximates the concentration of thiols adsorbed in the stamp itself. (b) Magnified schematic view that illustrates the variety of structural arrangements found in SAMs prepared by μCP when the stamp is wetted with a 1−10 mM solution and applied to the substrate for 1−10 s.

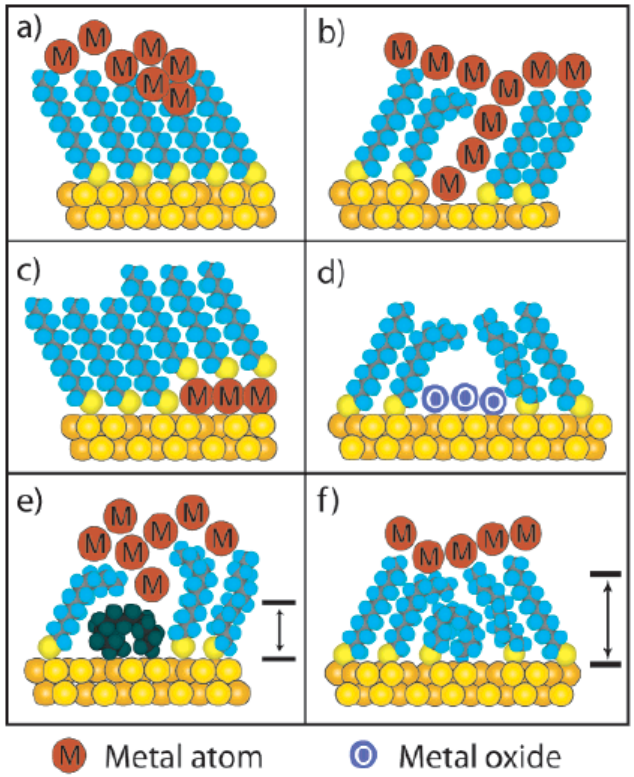

Figure 17. Schematic illustration of the types of defects in SAMs that can influence the rate of electron transfer in two-terminal (or three-terminal) devices. (a) Chemical reaction with the organic component of SAMs during evaporation of metal films. (b) Formation of metallic filaments during evaporation or operation of the device. (c) Deposition of adlayers of metal on the surface of the substrate supporting the SAM. (d) Formation of oxide impurities on the surface. (e) Organic (or organometallic) impurities in the SAM. (f) Thin regions in the SAM resulting from conformational and structural defects. In e and f the dimension normal to the surface that is denoted by the black arrows indicates the approximate shortest distance between the two metal surfaces; note that these distances are less than the nominal thickness of the ordered SAM.

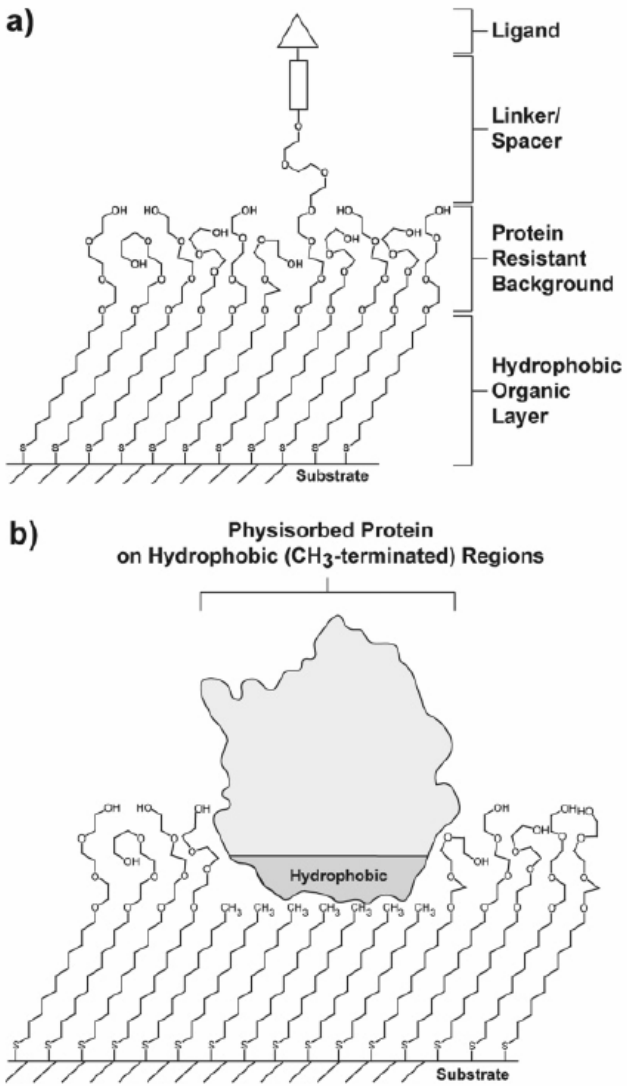

Figure 21. Schematic illustrations of (a) a mixed SAM and (b) a patterned SAM. Both types are used for applications in biology and biochemistry.

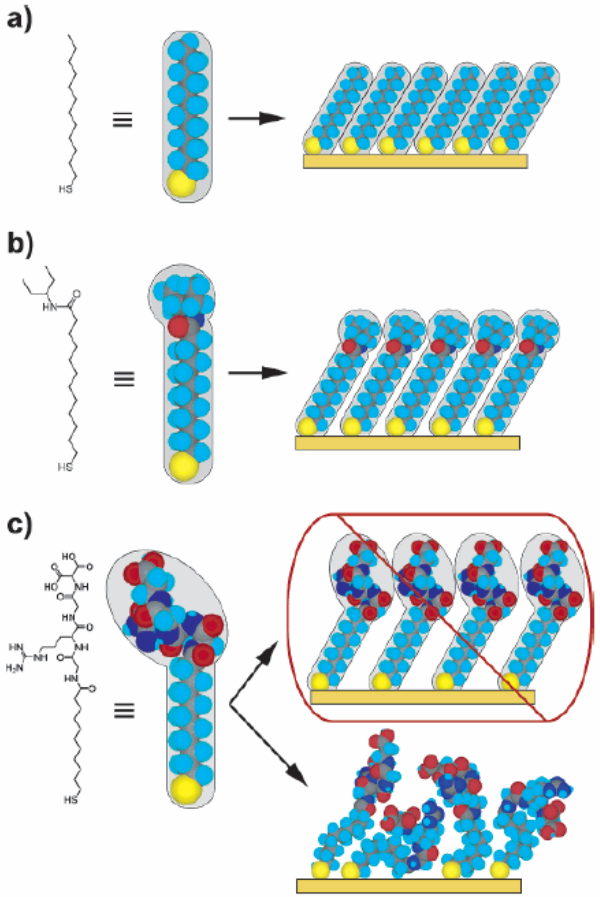

Figure 22. Schematic diagram illustrating the effects that large terminal groups have on the packing density and organization of SAMs. (a) Small terminal groups such as $-CH_3$, $-CN$, etc., do not distort the secondary organization of the organic layer and have no effect on the sulfur arrangement. (b) Slightly larger groups (like the branched amide shown here) begin to distort the organization of the organic layer, but the strongly favorable energetics of metal−sulfur binding drive a highly dense arrangement of adsorbates. (c) Large terminal groups (peptides, proteins, antibodies) sterically are unable to adopt a secondary organization similar to that for alkanethiols with small terminal groups. The resulting structures probably are more disordered and less dense than those formed with the types of molecules in a and b.

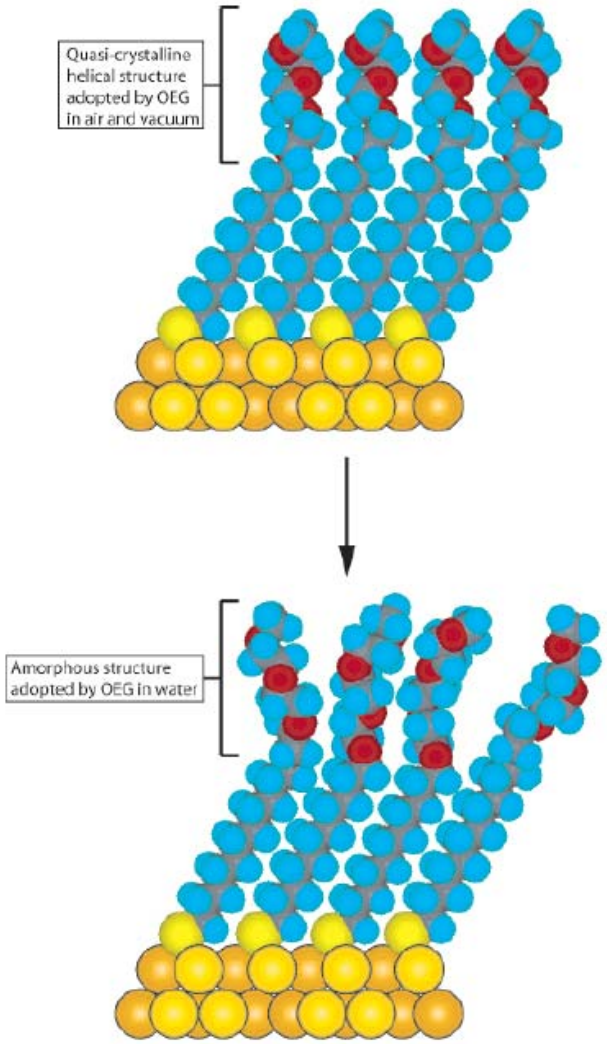

Figure 23. Schematic illustration of the order−disorder transition evidenced by SAMs of alkanethiolates terminated with triethylene glycol. The EG_3 group loses conformational ordering upon solvation in water.

Large On-Off Ratios and Negative Differential Resistance in a Molecular Electronic Device

J. Chen,[1] M. A. Reed,[1]* A. M. Rawlett,[2] J. M. Tour[2]*

19 NOVEMBER 1999 VOL 286 SCIENCE

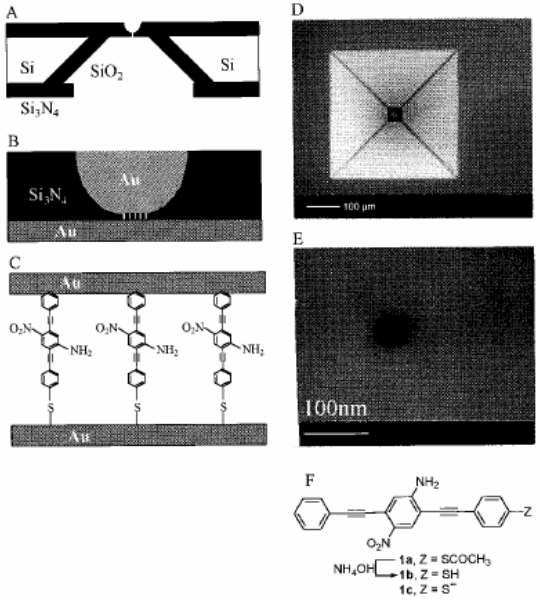

Fig. 1. Schematics of device fabrication. **(A)** Cross section of a silicon wafer with a nanopore etched through a suspended silicon nitride membrane. **(B)** Au-SAM-Au junction in the pore area. **(C)** Blowup of (B) with **1c** sandwiched in the junction. **(D)** Scanning electron micrograph (SEM) of pyramid Si structure after unisotropic Si etching [that is, the bottom view of (A)]. **(E)** SEM of an etched nanopore through the silicon nitride membrane. **(F)** The active molecular compound **1c** and its precursors the free thiol **1b** and the thiol-protected system **1a**.

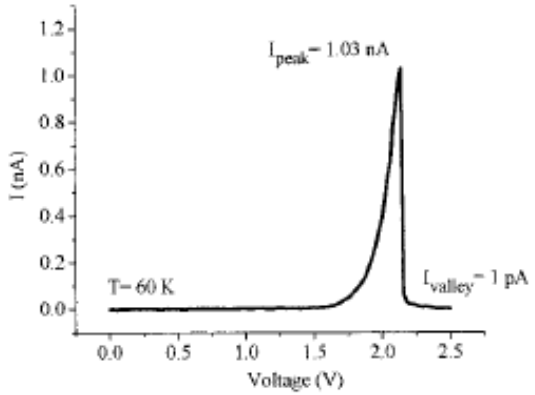

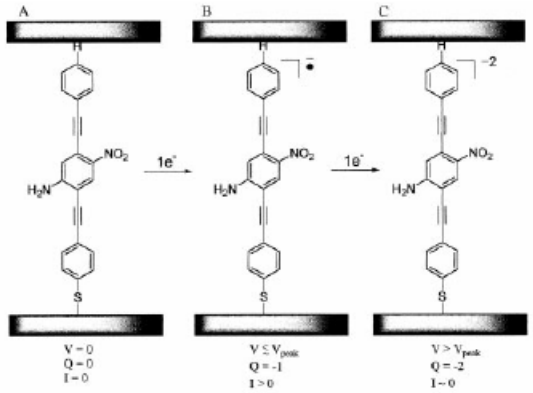

Fig. 4. Potential mechanism for the NDR effect. As voltage is applied, the molecules in the SAM (**A**) undergo a one-electron reduction to form the radical anion (**B**) that provides a conductive state. Further increase of the voltage causes another one-electron reduction to form the dianion insulating state (**C**). Q is the charge.

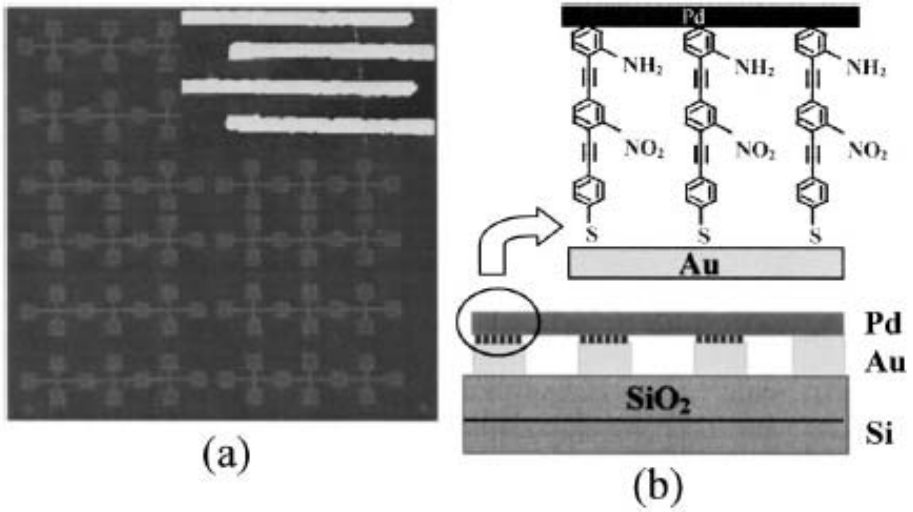

FIG. 1. (a) Optical micrograph of the nanoelectrode array. Inset: AFM image of four Au nanoelectrodes with a Pd nanowire lying across. (b) Schematic diagram of the Pd/molecular wires/Au junctions on a Si/SiO_2 substrate.

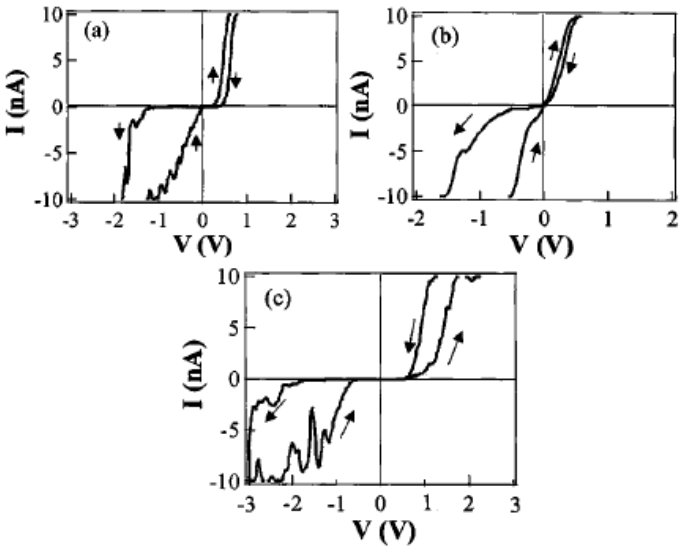

FIG. 3. Typical $I-V$ curves of molecular devices. (a), (b), and (c) correspond to molecules **a**, **b**, and **c** shown in Fig. 2, respectively.

Control of crystal nucleation by patterned self-assembled monolayers

NATURE | VOL 398 | 8 APRIL 1999

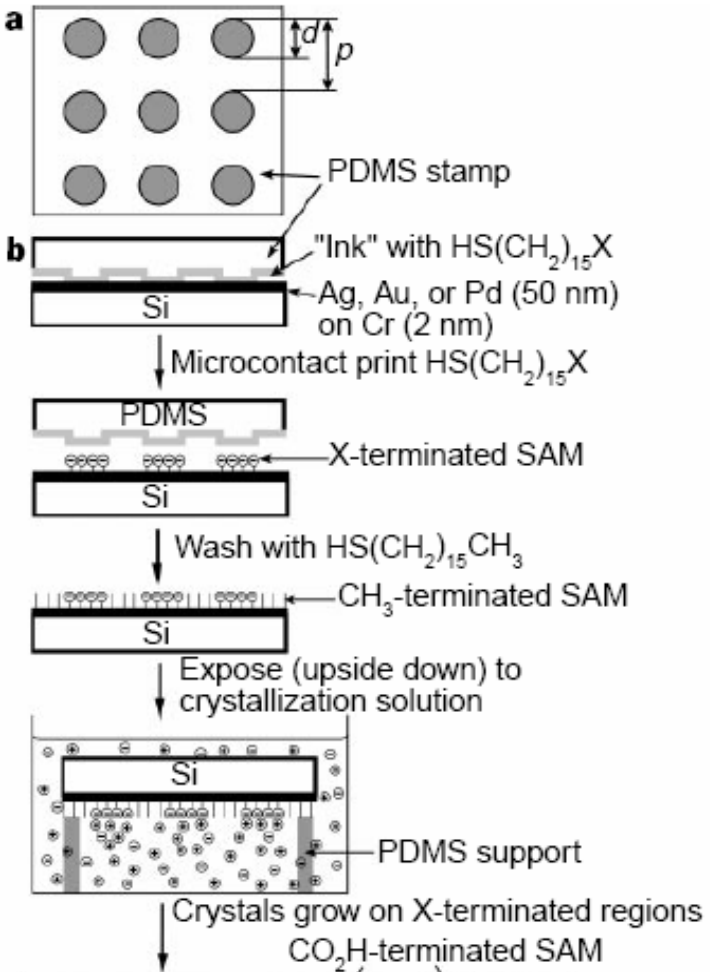

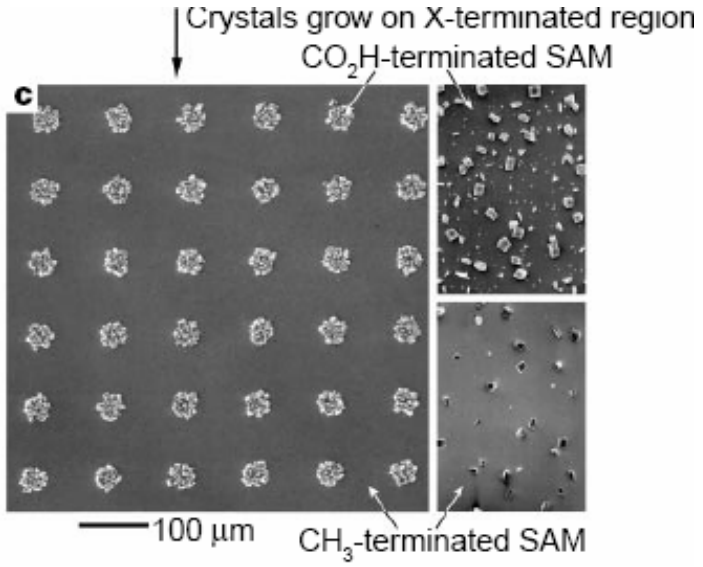

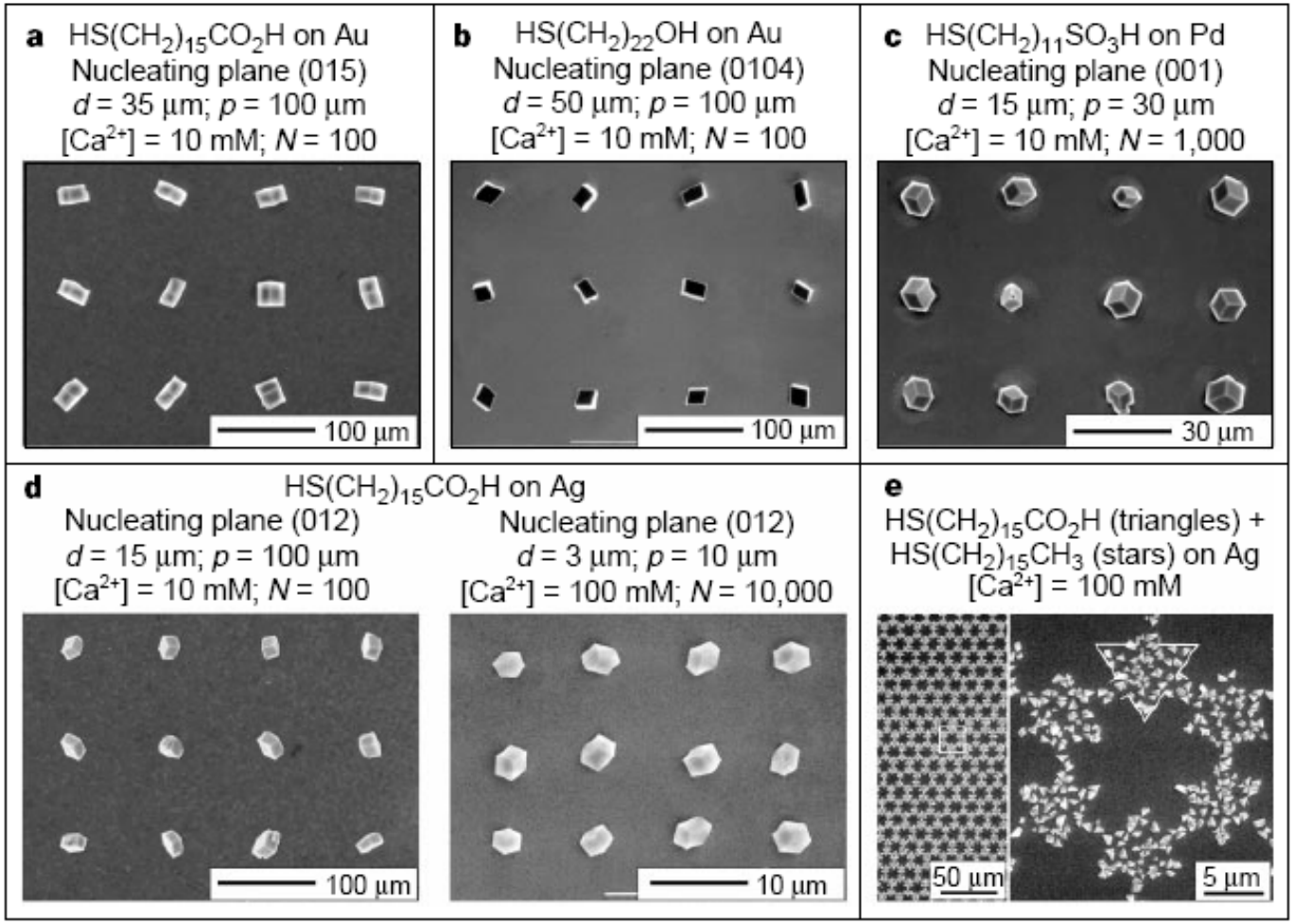
a
HS(CH2)15CO2H on Au
Nucleating plane (015)
d = 35 μm; p = 100 μm
[Ca2+] = 10 mM; N = 100
100 μm
b
HS(CH2)22OH on Au
Nucleating plane (0104)
d = 50 μm; p = 100 μm
[Ca2+] = 10 mM; N = 100
100 μm
c
HS(CH2)11SO3H on Pd
Nucleating plane (001)
d = 15 μm; p = 30 μm
[Ca2+] = 10 mM; N = 1,000
30 μm
d
HS(CH2)15CO2H on Ag
Nucleating plane (012)
d = 15 μm; p = 100 μm
[Ca2+] = 10 mM; N = 100
100 μm
Nucleating plane (012)
d = 3 μm; p = 10 μm
[Ca2+] = 100 mM; N = 10,000
10 μm
e
HS(CH2)15CO2H (triangles) +
HS(CH2)15CH3 (stars) on Ag
[Ca2+] = 100 mM
50 μm
5 μm

Geometric Control of Cell Life and Death

SCIENCE • VOL. 276 • 30 MAY 1997

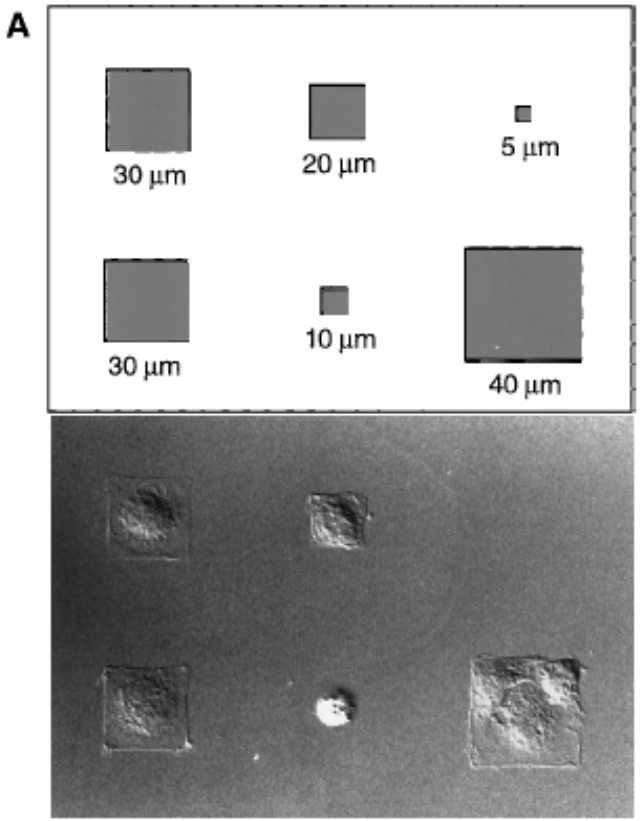

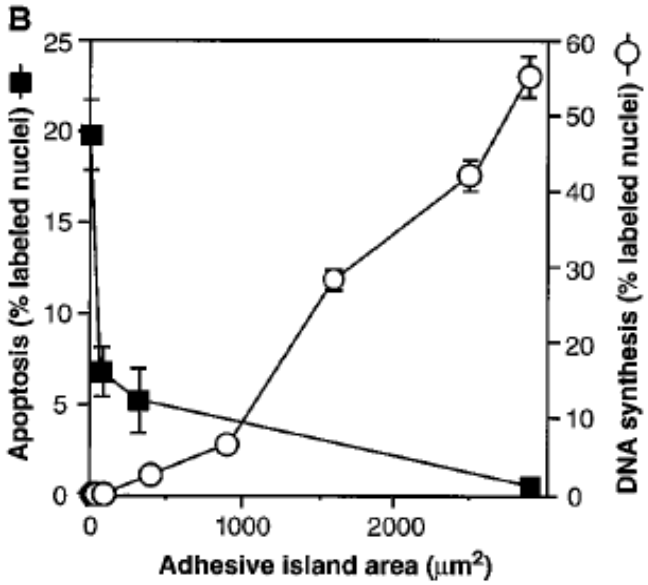

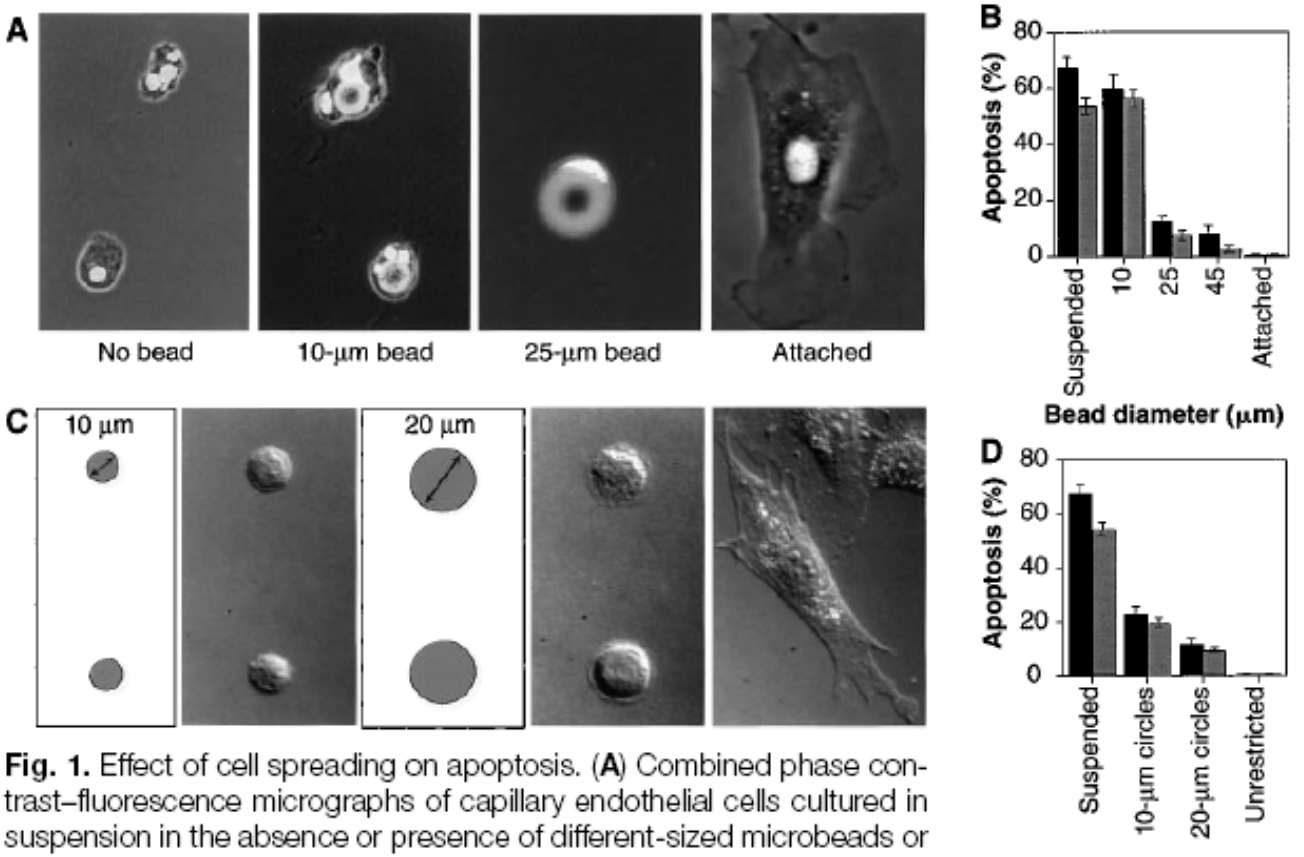

Fig. 1. Effect of cell spreading on apoptosis. (**A**) Combined phase contrast–fluorescence micrographs of capillary endothelial cells cultured in suspension in the absence or presence of different-sized microbeads or attached to a planar culture dish coated with FN for 24 hours (*28*). In the highly spread cell on the 25-μm bead, only the flattened 4′,6′-diamidino-2-phenylindole (DAPI)–stained nucleus is clearly visible. (**B**) Apoptosis in cells attached to different-sized beads, in suspension, or attached to a dish. The apoptotic index was quantitated by measuring the percentage of cells exhibiting positive TUNEL staining (black bars) (Boehringer Mannheim), which detects DNA fragmentation; similar results were obtained by analyzing changes in nuclear condensation and fragmentation in cells stained with DAPI at 24 hours (gray bars). Apoptotic indices were determined only within single cells bound to single beads. Error bars indicate SEM. (**C**) Differential interference-contrast micrographs of cells plated on substrates micropatterned with 10- or 20-μm-diameter circles coated with FN (left), by a microcontact printing method (*29*) or on a similarly coated unpatterned substrate (right). (**D**) Apoptotic index of cells attached to different-sized adhesive islands coated with a constant density of FN for 24 hours; similar results were obtained with human and bovine capillary endothelial cells (*28*). Bars same as in (B).

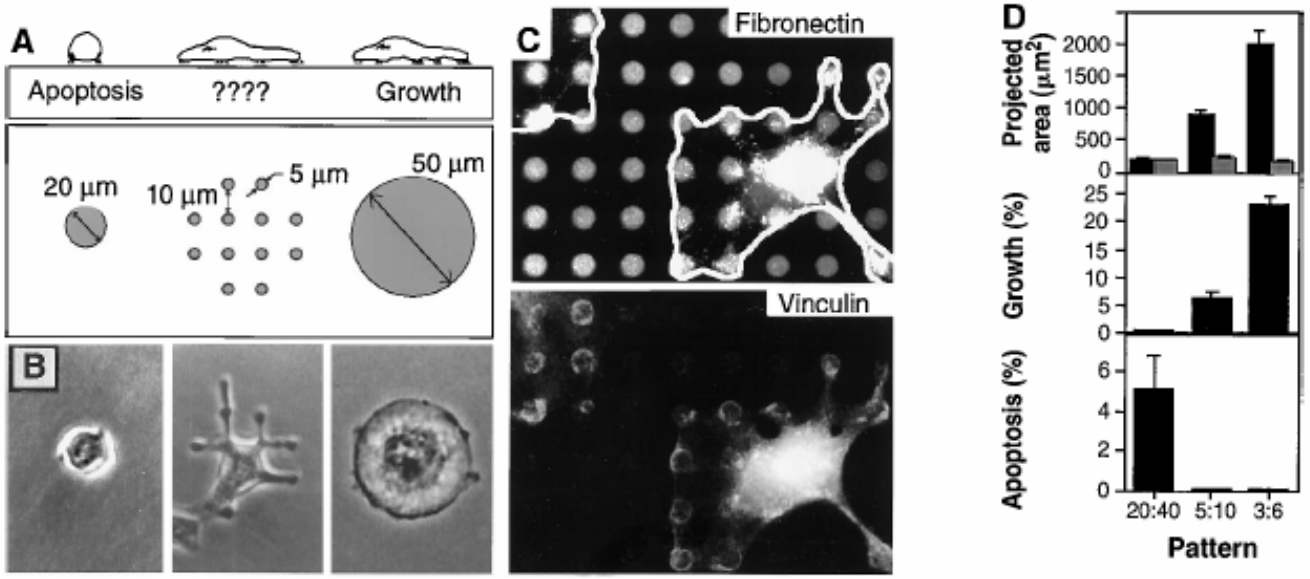

Fig. 3. Cell-ECM contact area versus cell spreading as a regulator of cell fate. (**A**) Diagram of substrates used to vary cell shape independently of the cell-ECM contact area. Substrates were patterned with small, closely spaced circular islands (center) so that cell spreading could be promoted as in cells on larger, single round islands, but the ECM contact area would be low as in cells on the small islands. (**B**) Phase-contrast micrographs of cells spread on single 20- or 50-μm-diameter circles or multiple 5-μm circles patterned as shown in (A). (**C**) Immunofluorescence micrographs of cells on a micropatterned substrate stained for FN (top) and vinculin (bottom). White outline indicates cell borders; note circular rings of vinculin staining, which coincide precisely with edges of the FN-coated adhesive islands. (**D**) Plots of projected cell area (black bars) and total ECM contact area (gray bars) per cell (top), growth index (middle), and apoptotic index (bottom) when cells were cultured on single 20-μm circles or on multiple circles 5 or 3 μm in diameter separated by 40, 10, and 6 μm, respectively.

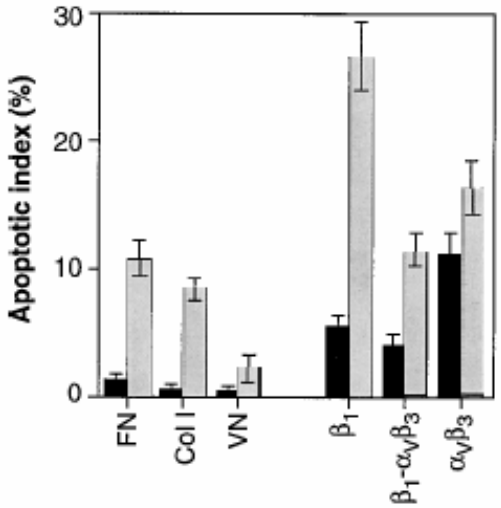

Fig. 4. Role of different integrin ligands in cell shape–regulated apoptosis. Apoptotic indices (percentage positive TUNEL staining) for cells cultured for 24 hours on unpatterned substrates (black bars) or on 20-μm circles (gray bars) coated with FN, type I collagen (Col I), vitronectin (VN), anti-β_1, anti-$\alpha_V\beta_3$, or antibodies to both integrin β_1 and integrin $\alpha_V\beta_3$ (*29*).

hexadecanethiol [$HS(CH_2)_{15}CH_3$] was printed onto gold-coated substrates with a flexible stamp containing a relief of the desired pattern. The substrate was immersed immediately in 2 mM tri(ethylene glycol)-terminated alkanethiol [$HS(CH_2)_{11}(OCH_2CH_2)_3OH$ in ethanol], which coated the remaining bare regions of gold. When these substrates were immersed in a solution of FN, vitronectin, or type I collagen (50 μg/ml in phos-

Directing cell migration with asymmetric micropatterns

http://www.pnas.org/cgi/reprint/102/4/9

PNAS | January 25, 2005 | vol. 102 | no. 4 | 975

Xingyu Jiang*, Derek A. Bruzewicz*, Amy P. Wong*, Matthieu Piel†, and George M. Whitesides*‡

*Department of Chemistry and Chemical Biology, Harvard University, 12 Oxford Street, Cambridge, MA 02138; and †Department of Molecular and Cellu Biology, Harvard University, 16 Divinity Avenue, Cambridge, MA 02138

Contributed by George M. Whitesides, December 2, 2004

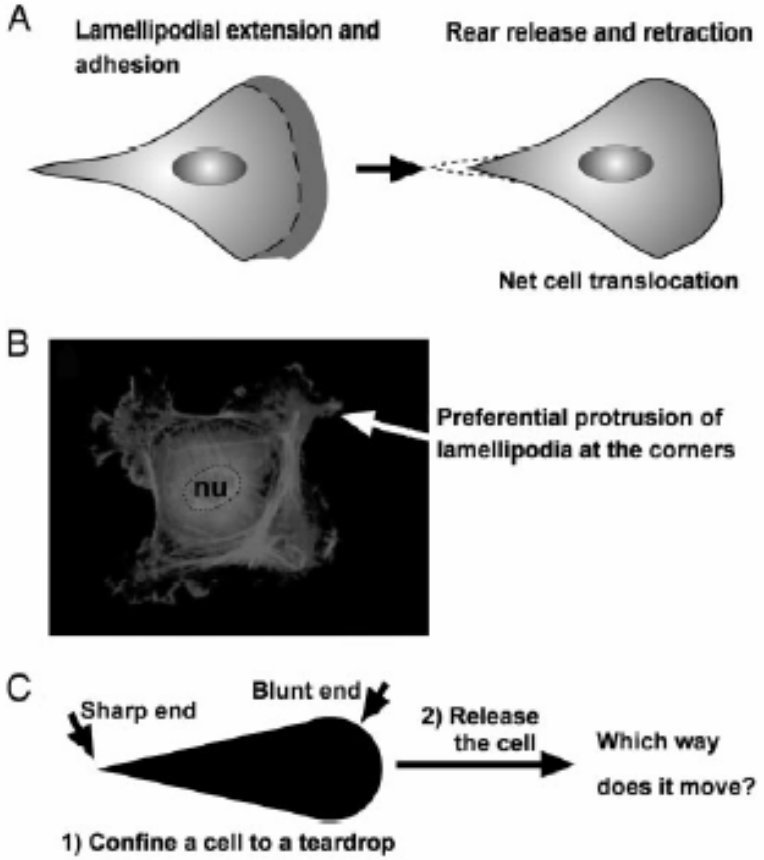

Fig. 1. A problem on cell motility. (*A*) A cartoon illustration of the migration of a typical mammalian cell on a flat surface. This teardrop shape is found in many types of cells. (*B*) Cells confined to squares preferentially extend their lamellipodia from the corners. nu, nucleus. (*C*) If a cell is confined to a shape of teardrop, will the cell preferentially extend its lamellipodia from the sharp end or from the blunt end? If released from confinement, in which direction will it likely move?

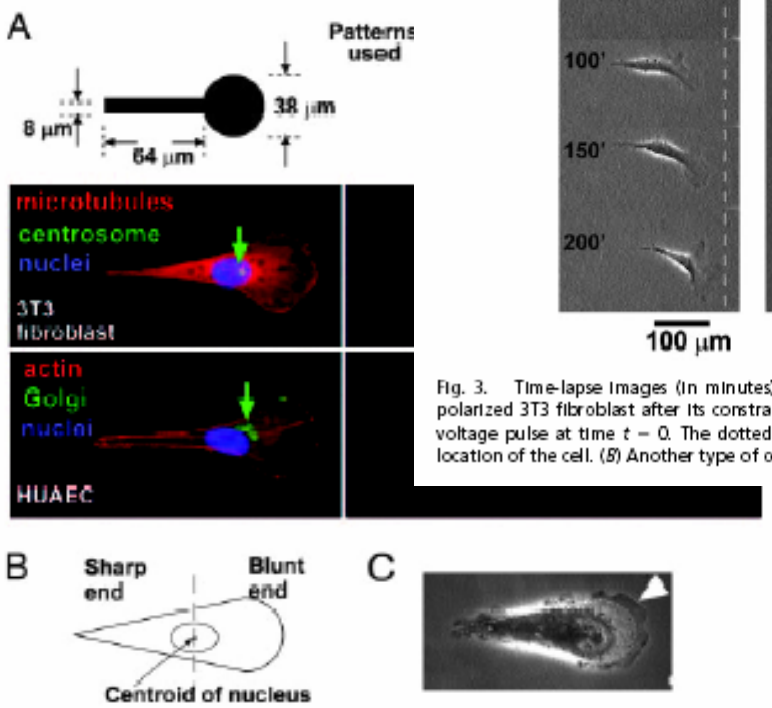

Fig. 2. Asymmetric patterns polarize immobilized cells. (*A*) The Golgi and the centrosome are located closer to the half of a cell with the blunt end. We used phallodin, antigolgin, DAPI, antitubulin, and antipericentrin to identify actin (red), the Golgi (green), the nucleus (blue), microtubules (red), and the centrosome (green), respectively. The green arrows indicate the location of centrosomes in 3T3 cells and Golgi in human umbilical artery endothelial cells (HUAEC). (*B*) We divided the cell into a half with the sharp end and a half with the blunt end by a vertical line drawn at the centroid of the nucleus; >80% ($n = 30$) of the centrosomes and Golgi were localized in the region of the wide end. (*C*) The lamellipodia of immobilized 3T3 cells tended to extend more from the blunt end as well (arrowhead). The dotted line indicates the edges of the adhesive pattern.

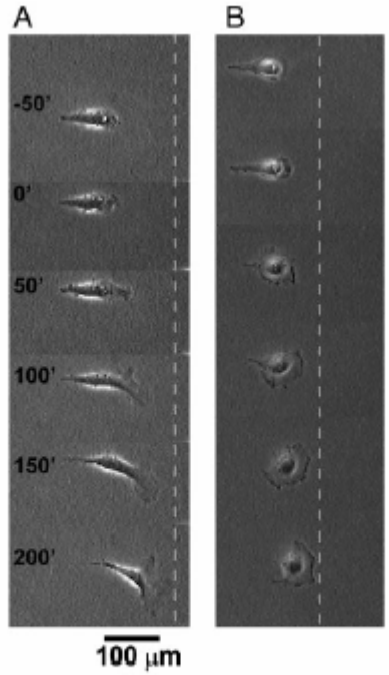

Fig. 3. Time-lapse images (in minutes) show the motility of an initially polarized 3T3 fibroblast after its constraint is released. (*A*) We applied the voltage pulse at time $t = 0$. The dotted line serves as a reference for the location of the cell. (*B*) Another type of cell, COS-7, shows similar behavior.

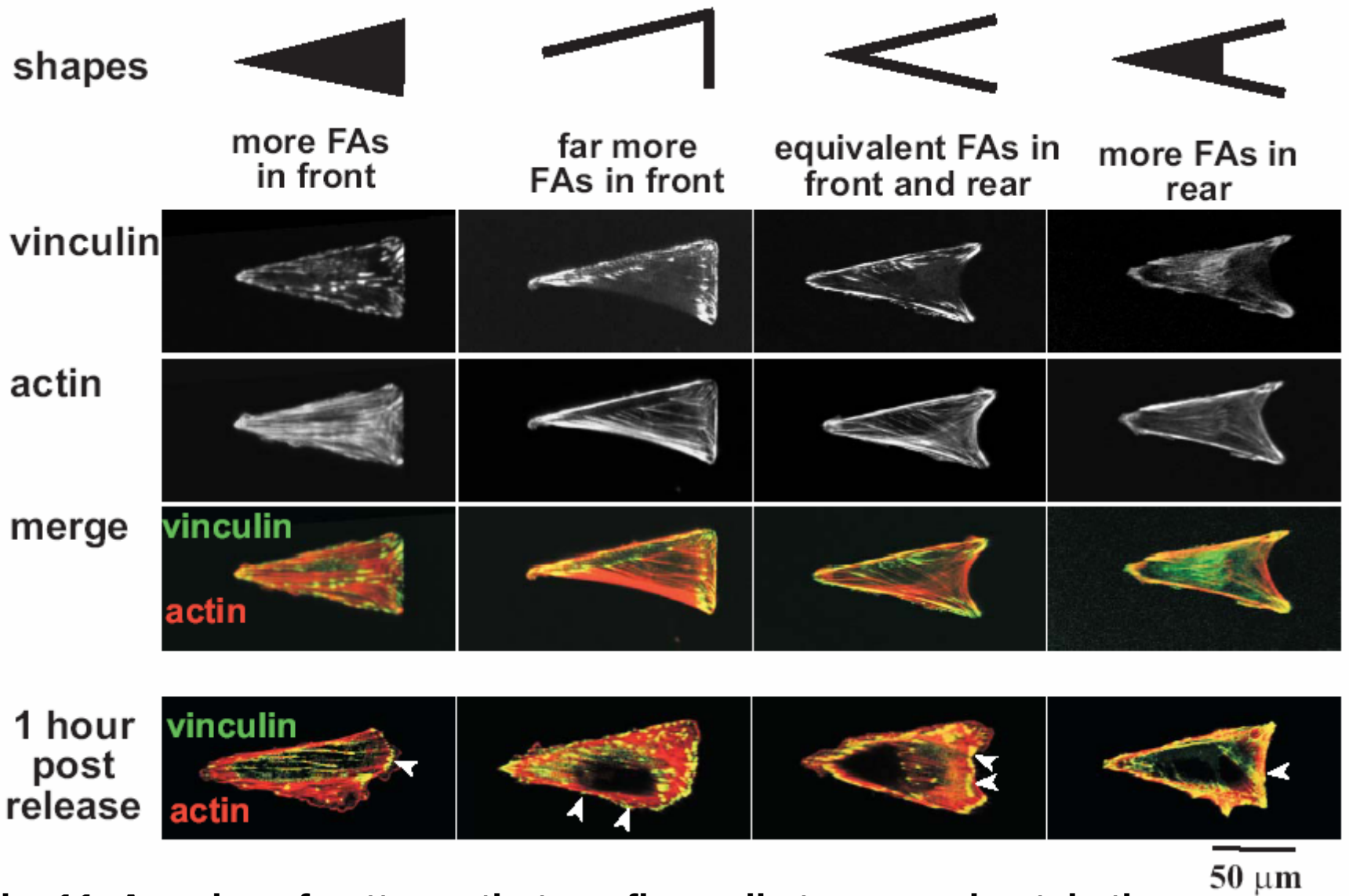

Fig. 11. A series of patterns that confine cells to approximately the same projected geometry (visualized by the actin cytoskeleton) but distribute the focal adhesions (FAs; visualized by immunostaining for vinculin) differently. The bottom row shows that new focal adhesions formed 1 h after release in areas that were inert to attachment of cells prior to release (arrowheads).

Soft-Lithography

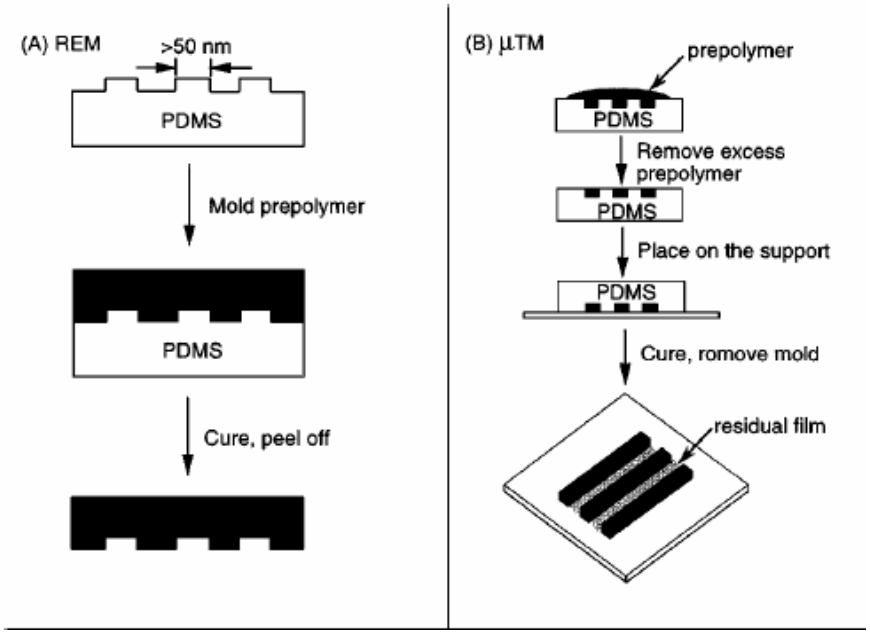

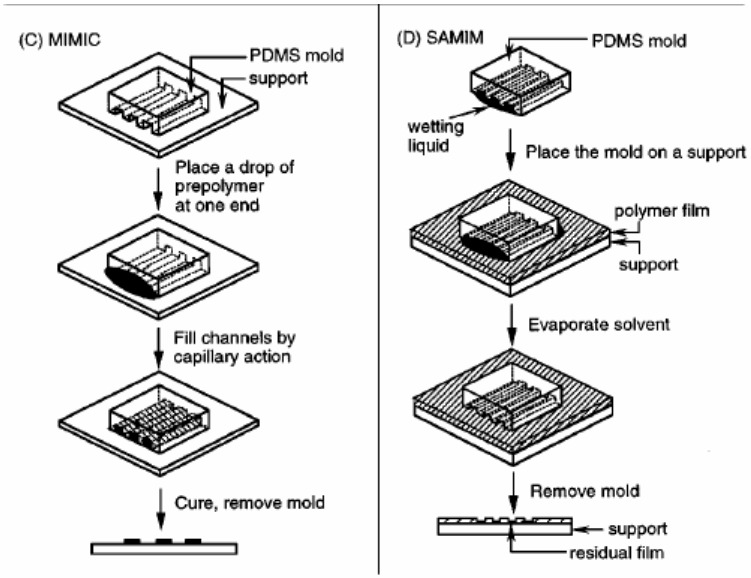

Figure 5 Schematic illustration of procedures for (*a*) replica molding (REM), (*b*) microtransfer molding (μTM), (*c*) micromolding in capillaries (MIMIC), and (*d*) solvent-assisted micromolding (SAMIM).

Electrophoresis 2002, 23, 3461–3473

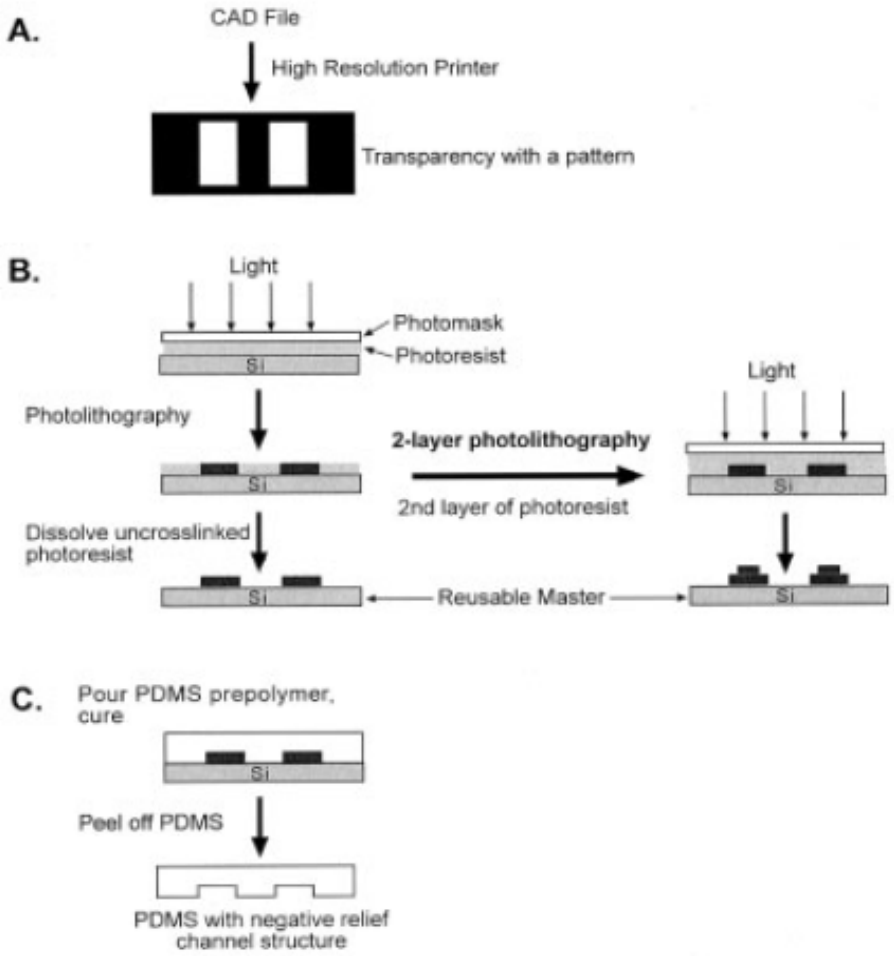

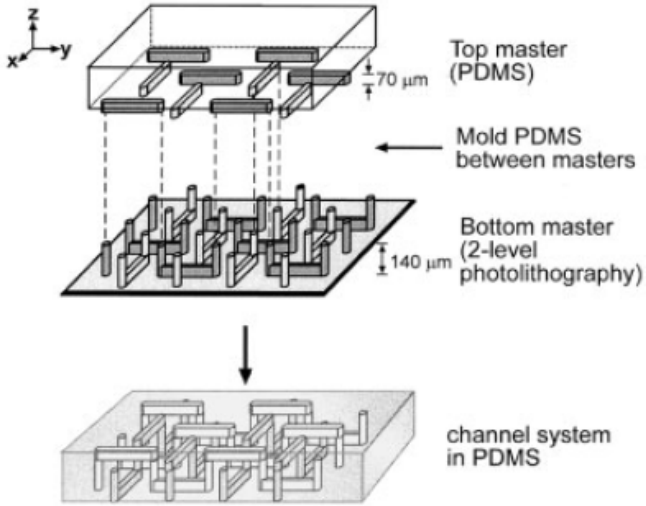

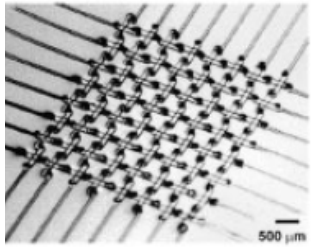

D.

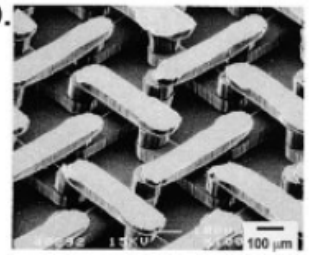

Replication Result

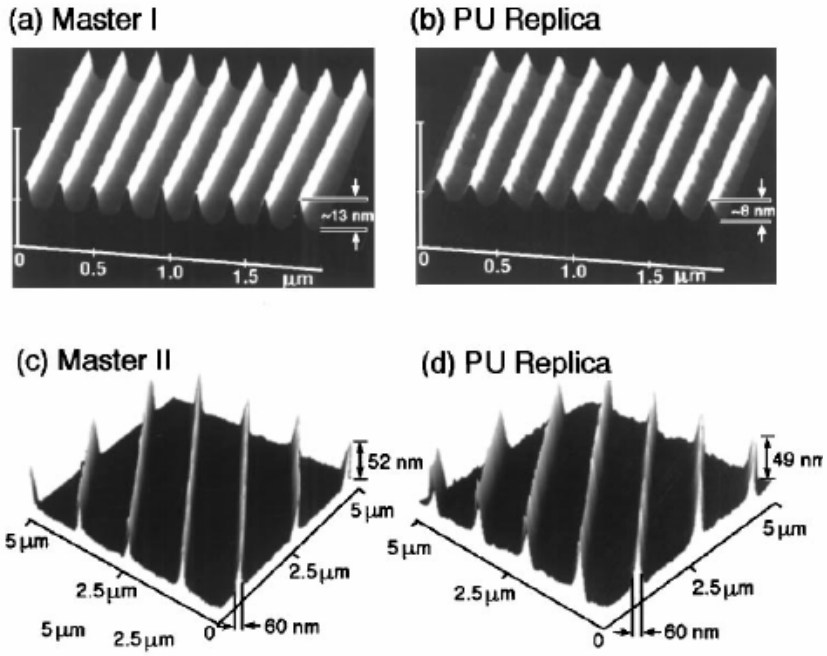

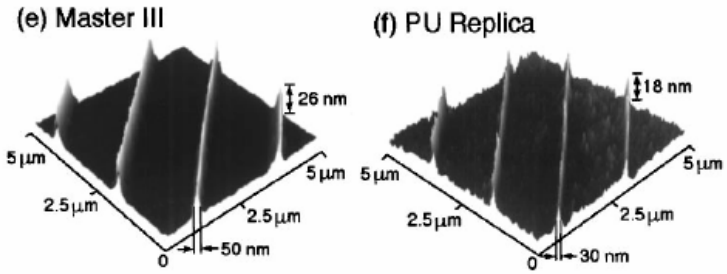

Figure 6 (*a,b*) Atomic force microscopy (AFM) images of Cr structures on a master, and a PU replica prepared from a PDMS mold cast from this master (153). (*c,d*) AFM images of Au structures on another master, and a PU replica produced from a PDMS mold cast from this master. (*e,f*) AFM images of Au structures on a third master, and a PU replica fabricated from a PDMS mold (cast from this master) while this mold was mechanically deformed by bending in a manner that generated narrower lines.

3D Patterning

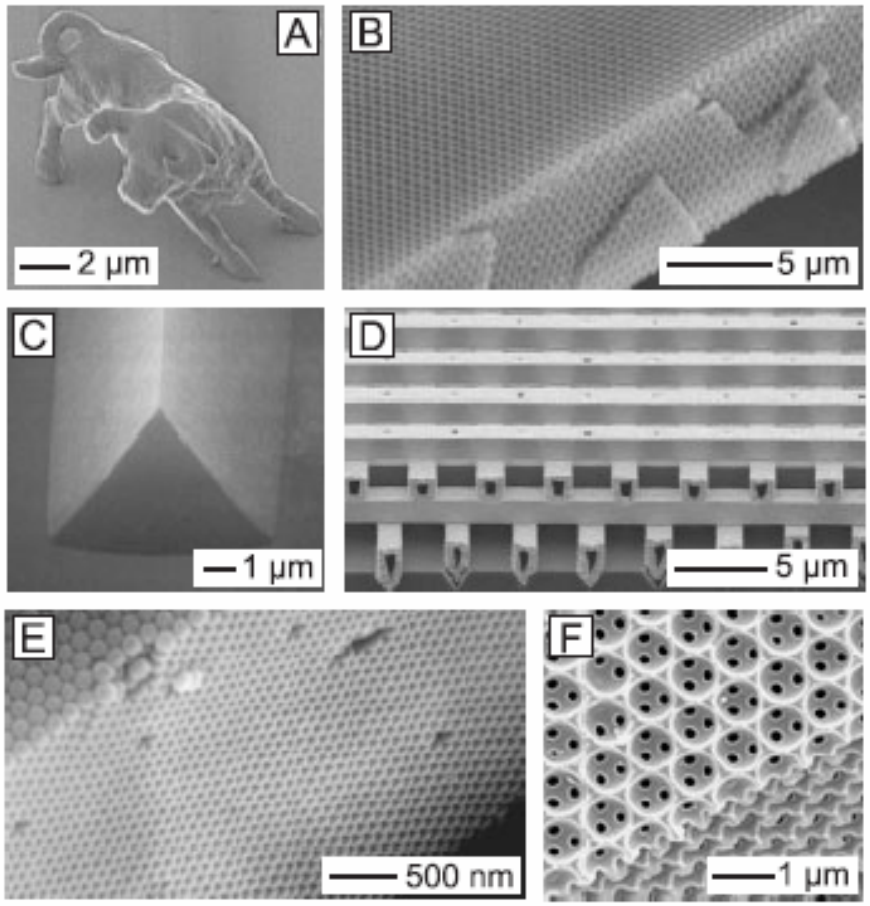

Interference

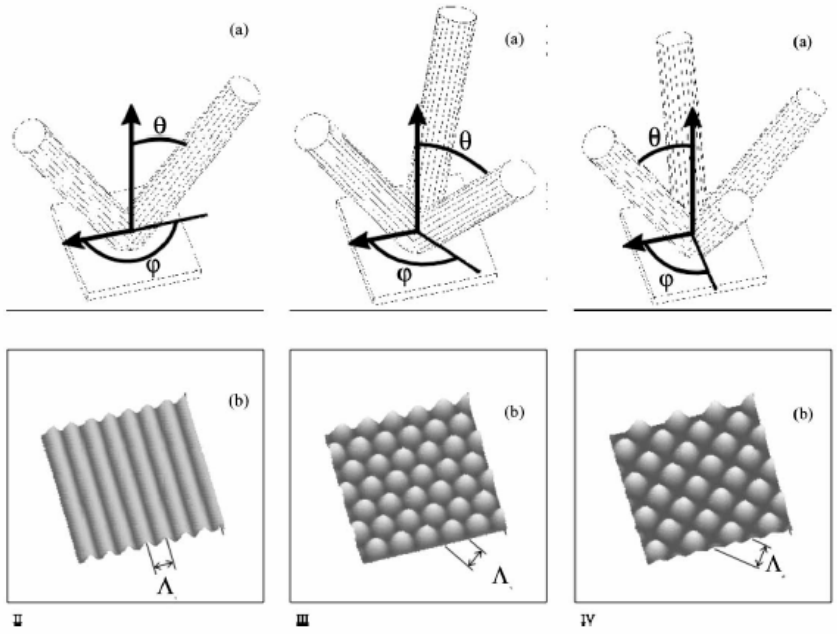

Fig. 1. The orientation of the two (left column), three (middle column) and four (right column) incident beams: (a) and the resulting interference patterns (b).

1. Two beams

$$I_2' = I_1 + I_2 + 2\cos(k(R_2 - R_1))$$

2. Three beams

$$I_3' = I_1 + I_2 + I_3 + 2[\cos(k(R_2 - R_1)) + \cos(k(R_3 - R_1)) + \cos(k(R_3 - R_2))]$$

3. Four beams

$$I_4' = I_1 + I_2 + I_3 + I_4 + 2[\cos(k(R_2 - R_1)) + \cos(k(R_3 - R_1)) + \cos(k(R_3 - R_2)) + \cos(k(R_4 - R_1)) + \cos(k(R_4 - R_2)) + \cos(k(R_4 - R_3))]$$

Interference

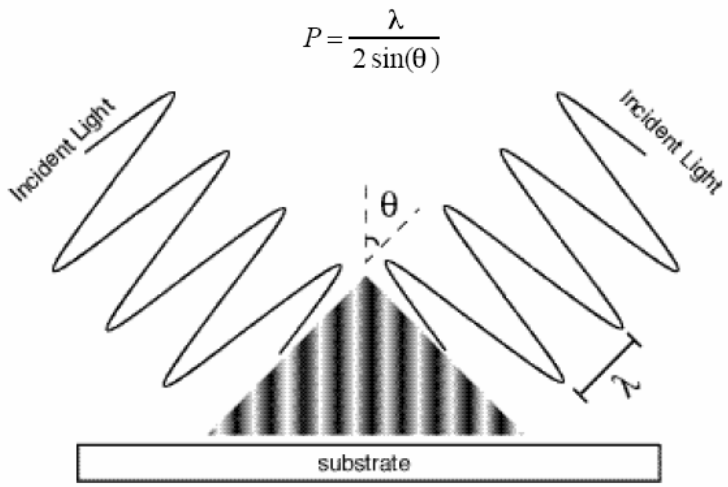

Figure 2.1: *Two-beam interference forms a standing wave.*

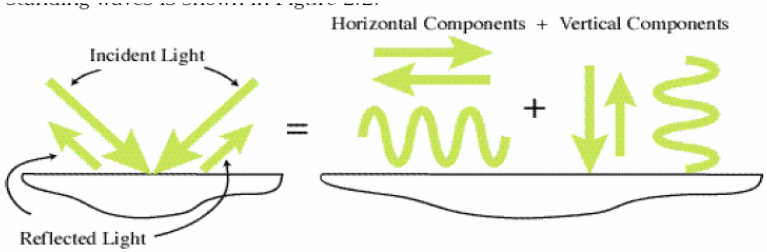

Figure 2.2: *The horizontal and vertical components combine separately to create the desired horizontal standing wave and the undesired vertical standing wave*

Interference Lithography

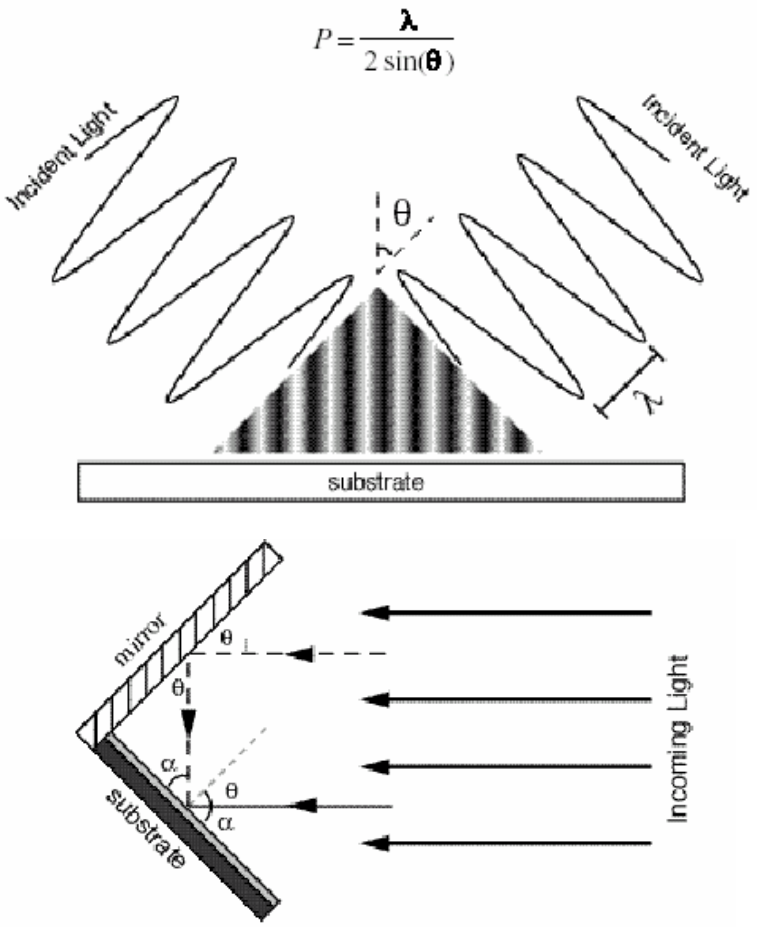

Figure 3.2) Basic Lloyd's mirror configuration

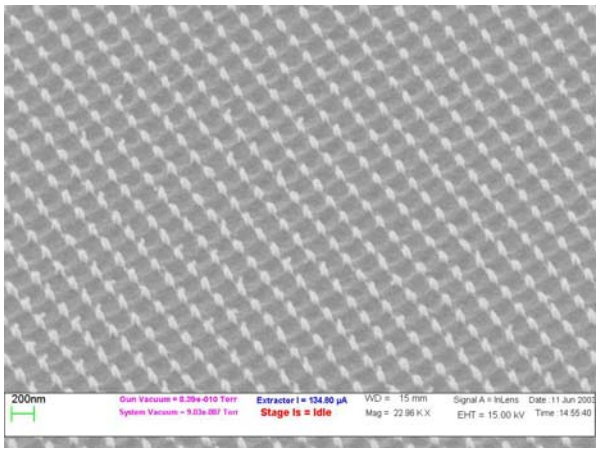

Holographic

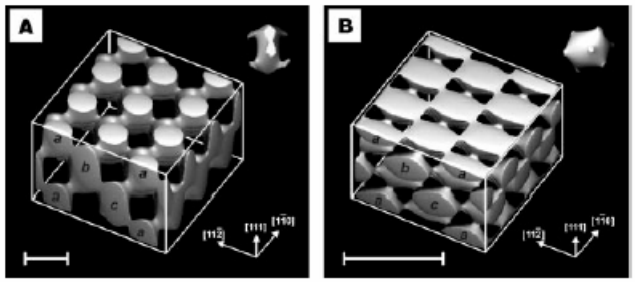

Figure 1 Calculated constant-intensity surfaces in four-beam laser interference patterns designed to produce photonic crystals for the visible spectrum from photoresist. The primitive basis (contents of a Wigner-Seitz unit cell) is shown inset in each case. **A**, f.c.c. pattern with lattice constant 922 nm, used to produce the structures shown in Fig. 3a–d and 4. The close-packed layers of the f.c.c. lattice are indicated on one side of the cube. **B**, f.c.c. pattern with lattice constant 397 nm. Scale bars, 500 nm.

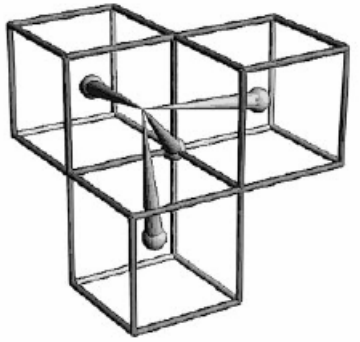

Figure 2 Beam geometry for an f.c.c. interference pattern. The wavevectors of the four laser beams are drawn as cones originating from lattice points in a b.c.c reciprocal lattice. The differences between the central beam wavevector $\mathbf{k}_0$, which originates from the common point of the three cubes shown, and the three wavevectors $\mathbf{k}_{1-3}$ originating from body-centre lattice points, are the primitive set of reciprocal lattice vectors $2\pi/d\langle\bar{1}11\rangle$.

Holographic

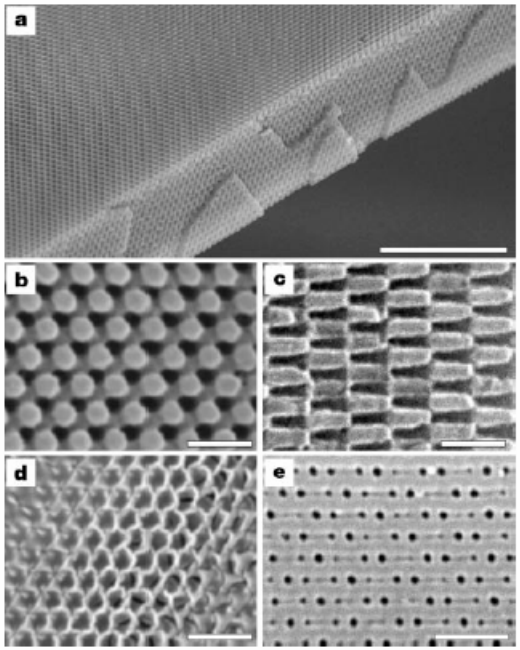

Figure 3 SEM images of photonic crystals generated by holographic lithography. **a**, Polymeric photonic crystal generated by exposure of a 10-μm film of photoresist to the interference pattern shown in Fig. 1A. The top surface is a (111) plane; the film has been fractured along the (11$\bar{1}$) cleavage planes. Scale bar, 10 μm. **b**, Close-up of a (111) surface. Scale bar, 1 μm. **c**, Close-up of a (11$\bar{1}$) surface. Scale bar, 1 μm. **d**, Inverse replica in titania made by using the polymeric structure as a template. The surface is slightly tilted from the (111) plane. Scale bar, 1 μm. **e**, ($\bar{1}$02) surface of a b.c.c. polymeric photonic crystal. Scale bar, 1 μm.

Micro- and Nanofluidic

Lab-on-a-Chip

Potential Benefit of Miniaturization

- Improve performance (reduced diffusion length, shorter separation distance, less band broadening, high field strength, parallel system)
- Integration (all in one)
- Added functionality (2D separation)
- Versatility (compact, portable, easy to use, low energy an chemical consumption)

How much miniaturization make sense ?

NATURE MEDICINE, VOLUME 1, NUMBER 10, OCTOBER 1995

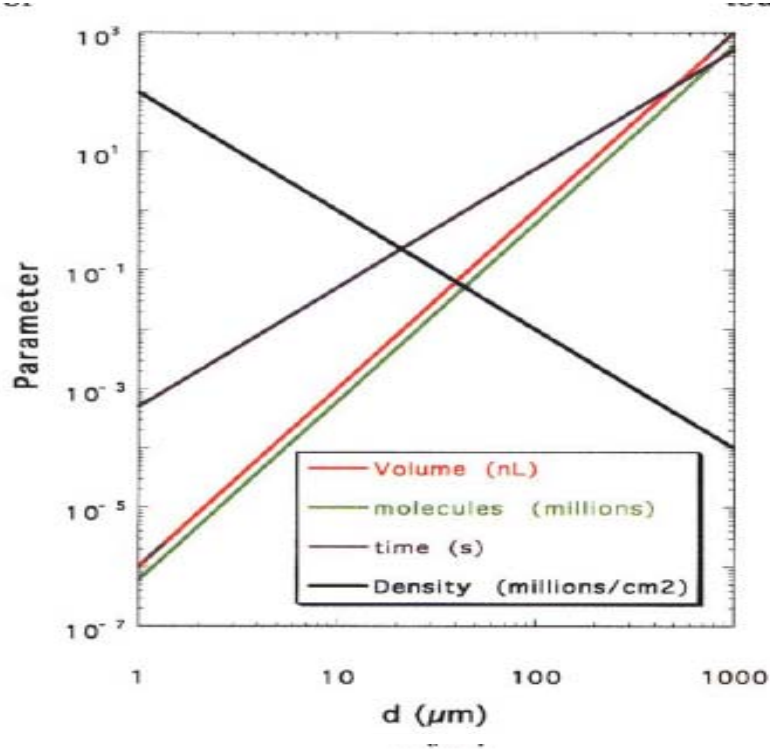

Fig. 1 Scaling of various parameters with dimensional cross section. It is assumed that an analysis is performed within a cube with a side of length *d*. The volume of fluid, number of analyte molecules, time to diffusively mix, and spatial density are shown as a function of dimension *d*. A concentration of one nanomolar and a diffusion coefficient of 10^{-5} cm^2 s^{-1} are assumed. See text for discussion.

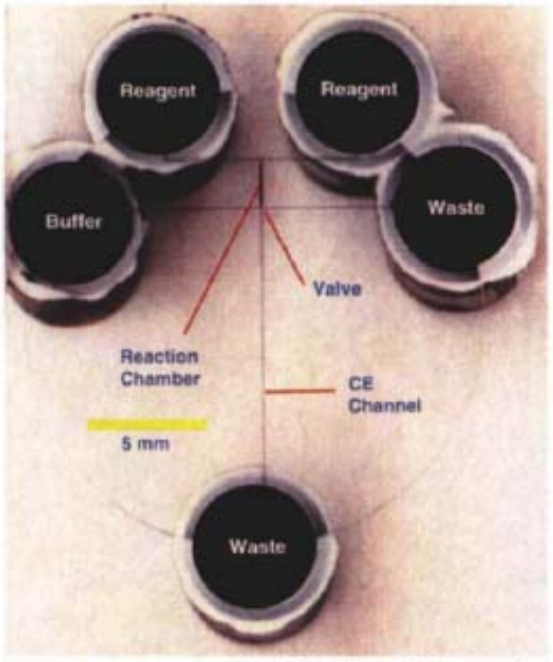

Micromachining a Miniaturized Capillary Electrophoresis-Based Chemical Analysis System on a Chip

D. Jed Harrison,* Karl Fluri, Kurt Seiler, Zhonghui Fan,
Carlo S. Effenhauser, Andreas Manz

SCIENCE • VOL. 261 • 13 AUGUST 1993

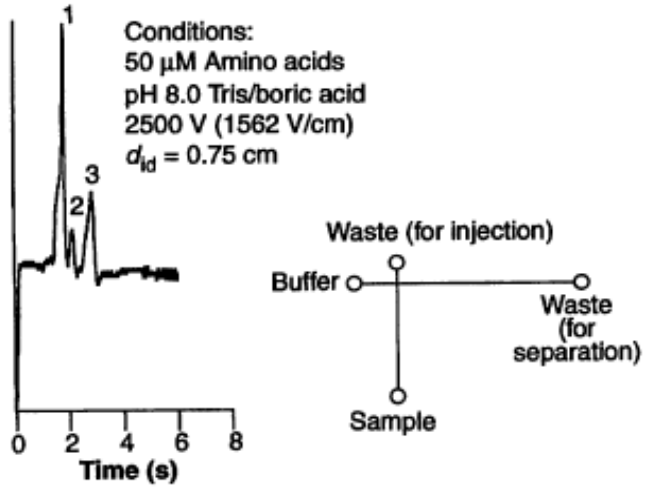

Fig. 3. Electropherogram of 10 μM FITC-labeled Arg, Phe, and Glu (peaks 1, 2, and 3, respectively) in pH 8.0 buffer in a device 1 cm by 2 cm, with an injection to detection distance of 0.75 cm.

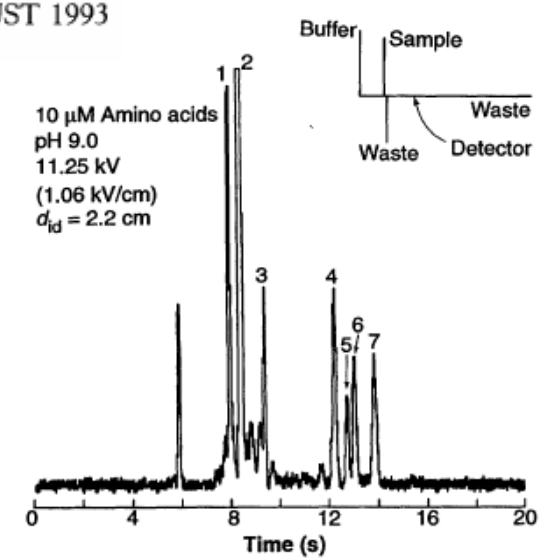

Fig. 2. Electropherogram of six FITC-labeled amino acids in pH 9.0 buffer with 2330 V applied between the injection and detection points and a potential applied to the side channels to reduce leakage of the sample. The peaks were identified by the separate injection of each component and are as follows: 1, Arg; 2, FITC hydrolysis product; 3, Gln; 4, Phe; 5, Asn; 6, Ser; and 7, Gly. The inset shows the approximate layout of the device, with a buffer to separation channel–waste distance of 10.6 cm.

Flow in small dimension

- Types of flow
  - Turbulent flow
  - Laminar flow
  - Creeping flow
- Generation of flow
  - Electroosmotic flow (plug flow)
  - Pressure driven flow (Poiseuille flow)
  - Shear-driven flow (Couette flow)

Newtonian Fluid

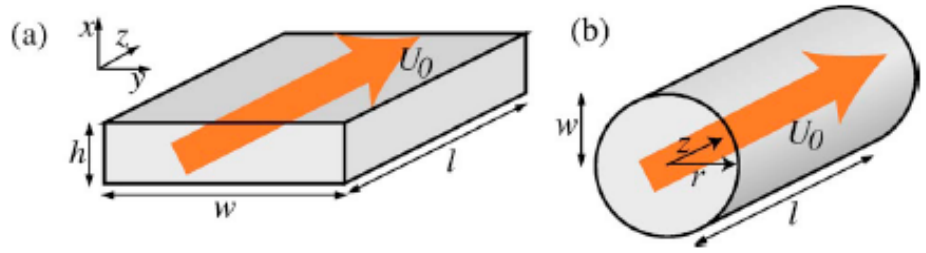

FIG. 2. (Color in online edition) Model (a) rectangular and (b) circular microchannels, through which fluid flows with characteristic velocity scale U_0. Channel length will be denoted l, width (or radius) w, and height (shortest dimension) h. The coordinate z points downstream, y spans the width, and x spans the height.

continuum version of $\mathbf{F}=m\mathbf{a}$ on a per unit volume basis:

$$\rho\left(\frac{\partial \mathbf{u}}{\partial t}+\mathbf{u}\cdot\nabla\mathbf{u}\right)=\nabla\cdot\vec{\vec{\sigma}}+\mathbf{f}=-\nabla p+\eta\nabla^2\mathbf{u}+\mathbf{f}, \qquad (1)$$

$$\rho\frac{\partial \mathbf{u}}{\partial t}=\nabla\cdot\boldsymbol{\sigma}+\mathbf{f}=-\nabla p+\eta\nabla^2\mathbf{u}+\mathbf{f}.$$

$$\frac{\partial \rho}{\partial t}+\nabla\cdot(\rho\mathbf{u})=0,$$

incompressibility condition $\nabla\cdot\mathbf{u}=0$

Basic

- Reynolds number

$$Re = \frac{\rho v_s L}{\mu} = \frac{v_s L}{\nu} = \frac{\text{Inertial forces}}{\text{Viscous forces}}$$

*v*s - mean fluid velocity,
L - characteristic length,
μ - (absolute) dynamic fluid viscosity,
ν - kinematic fluid viscosity: $\nu = \mu / \rho$,
ρ - fluid density.

- Hydraulic diameter

$$D_h = \frac{4A}{U}$$

A is the cross sectional area
U is the wetted perimeter of the cross-section

Laminar flow

- Sometimes known as streamline flow, occurs when a fluid flows in parallel layers, with no disruption between the layers. In fluid dynamics, laminar flow is a flow regime characterized by high momentum diffusion, low momentum convection, and pressure and velocity independence from time. It is the opposite of turbulent flow. In nonscientific terms laminar flow is "smooth," while turbulent flow is "rough."
- The (dimensionless) Reynolds number is an important parameter in the equations that describe whether flow conditions lead to laminar or turbulent flow. In laminar flow, the Reynolds number is less than 2100. Creeping motion or Stokes flow, an extreme case of laminar flow where viscous (friction) effects are much greater than inertial forces, occurs when the Reynolds number is much less than 1.

Turbulent flow

- In fluid dynamics, **turbulence** or **turbulent flow** is a flow regime characterized by chaotic, stochastic property changes. This includes low momentum diffusion, high momentum convection, and rapid variation of pressure and velocity in space and time. a Reynolds number above about 2300 will be turbulent.

How large must u be before turbulent flow (Re > 2000)

	d = 100 μm	10 μm
ρ_{air} = 0.0012 g/cm^3	u= 333 m/s	3333 m/s
η_{air} = 0.0002 g/s cm		
	Mach 1	Mach 10
ρ_{water} = 0.998 g/cm^3	u= 20m/s	200 m/s
η_{water} = 0.01 g/s cm		
ρ_{oil} = 0.8 g/cm^3	u= 2500 m/s	25000 m/s
η_{oil} = 1.0 g/s cm		

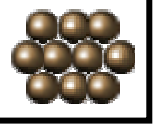

Forward (advective) vs. transverse (diffusive) transport

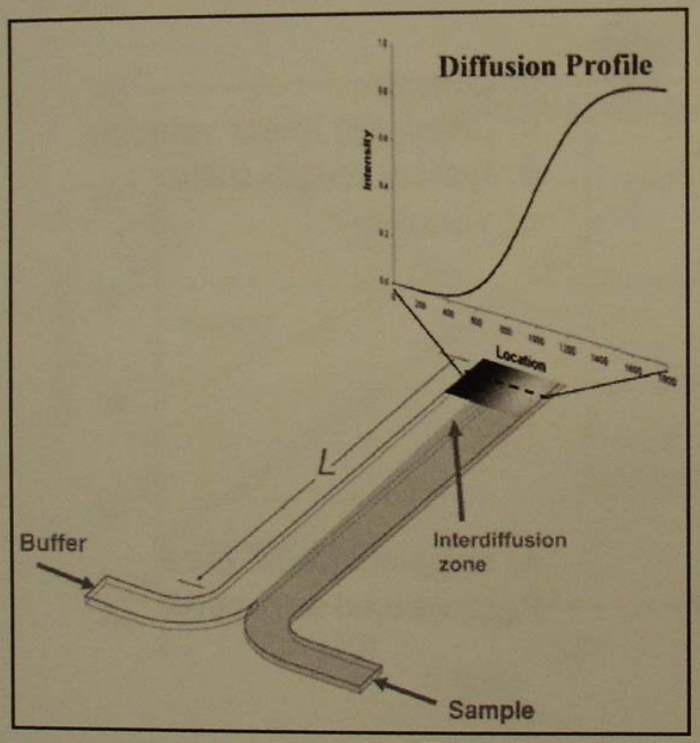

figure from Paul Yager, U. Washington

Einstein-Schmoluchowski equation:

$$x = \sqrt{2Dt}$$

x: distance diffused
D: diffusion coefficient
t: time

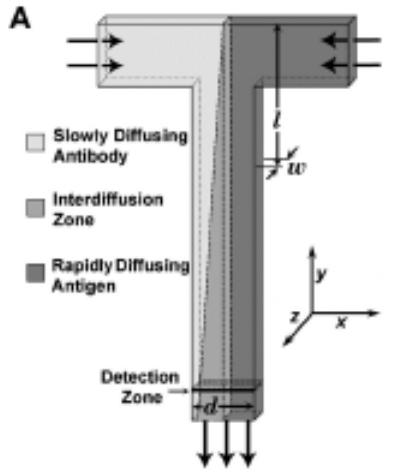
A
Slowly Diffusing Antibody
Interdiffusion Zone
Rapidly Diffusing Antigen
Detection Zone
l
w
d
y
z
x

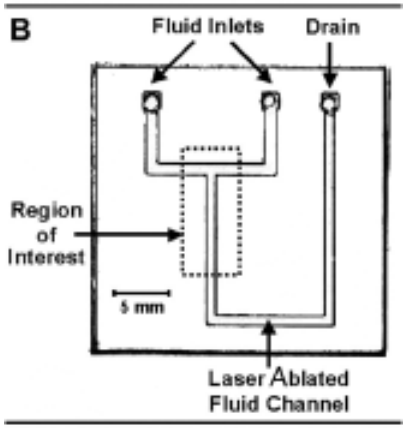
B
Fluid Inlets
Drain
Region of Interest
5 mm
Laser Ablated Fluid Channel

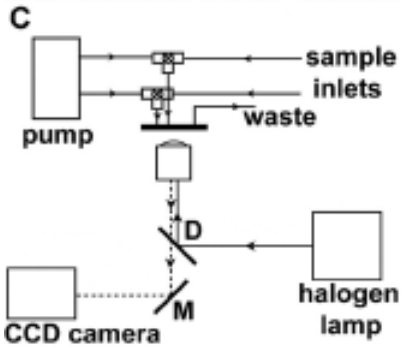
C
sample
inlets
waste
pump
D
halogen lamp
M
CCD camera

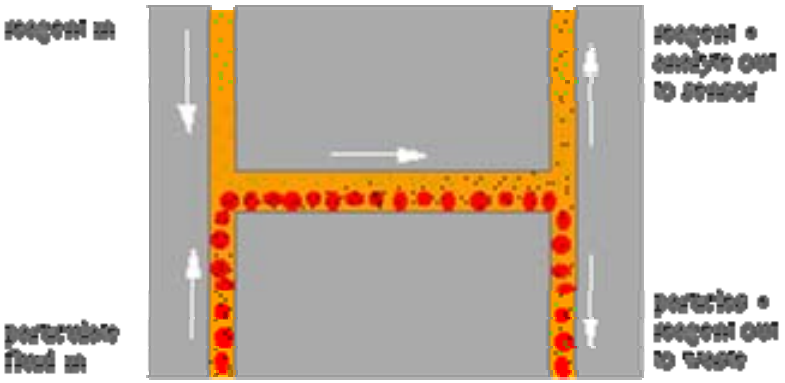

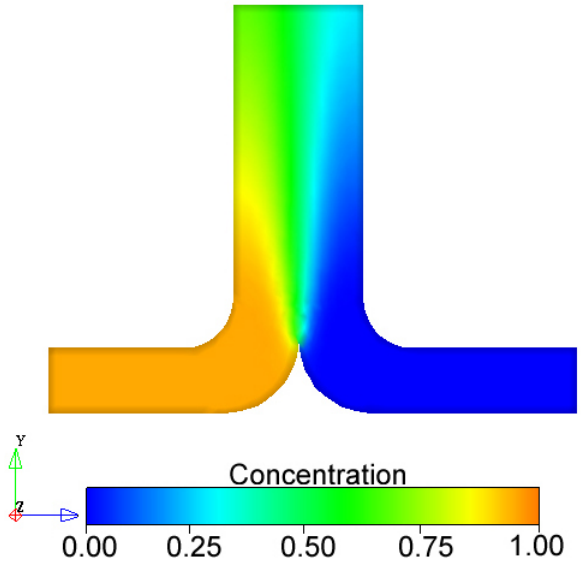
Y
Z
Concentration
0.00
0.25
0.50
0.75
1.00

Pressure Driven Flow

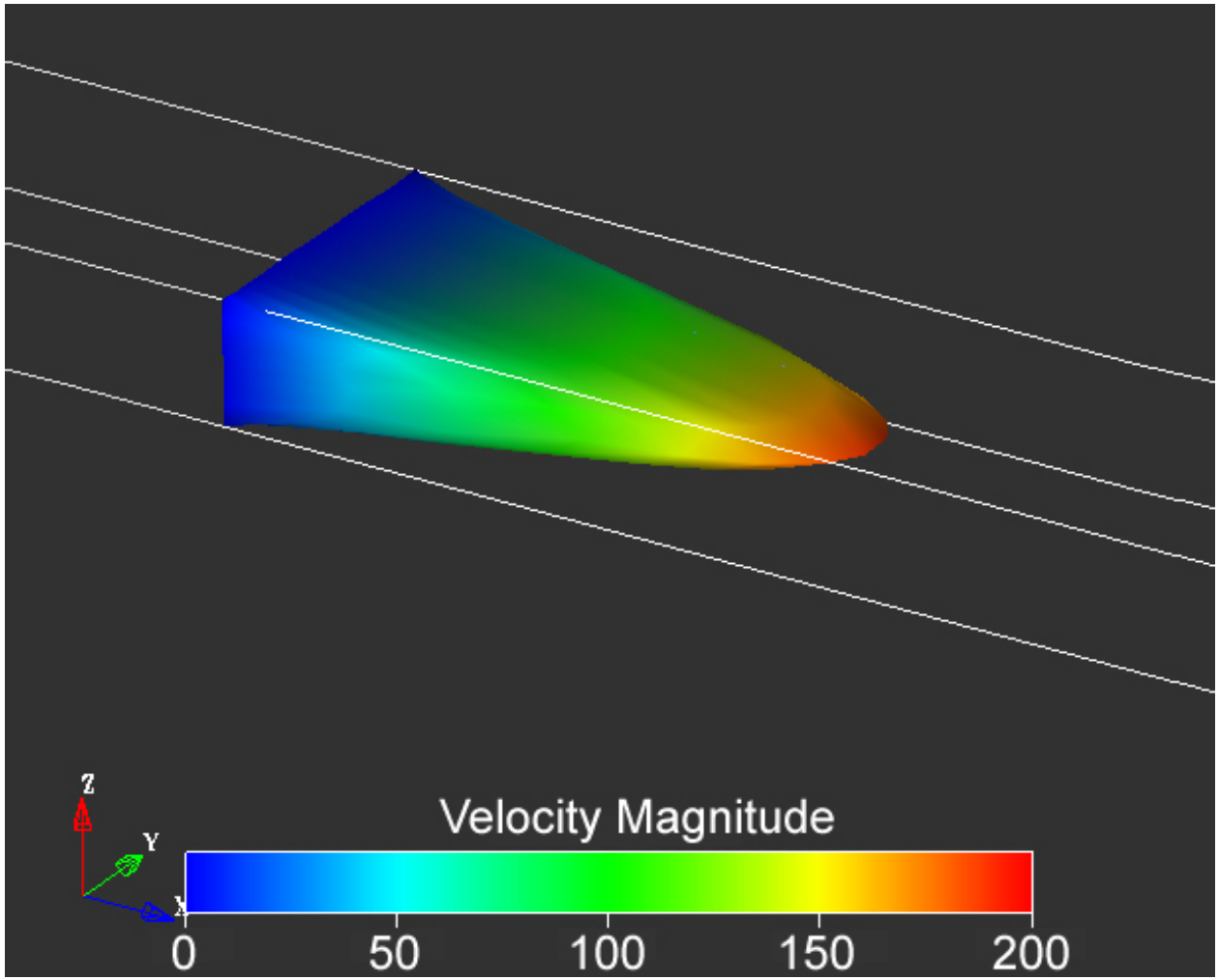

Microfluidics - basics

J. P. Kutter
µ-TAS group
DTU

Pressure-driven flow (Poiseuille flow)

Volume flow rate:

$$Q = \frac{\pi r_0^4}{8\eta L}\Delta P$$

Average linear velocity:

$$\bar{u} = \frac{r_0^2}{8\eta L}\Delta P$$

Velocity distribution:

$$u(r) = (r_0^2 - r^2)\frac{\Delta P}{4\eta L}$$

for a cylindrical tube of radius r_0 and length L

Pressure Driven Flow

$$v = \frac{\Delta P\, R^2}{8\eta\, L}$$

ΔP=100kPa (1atm)
$\eta=10^{-3}$ kgm^{-1}s^{-1}
L = 100 μm

R= 1 μm v= 30 mm s^{-1}

R=100 nm V = 300 μms^{-1}

L= 10 mm, R = 10 μm v= 3 mm s^{-1} **ΔP=100kPa**
L= 10 mm, R = 100 nm v= 3 mm s^{-1} **ΔP= 1 GPa**

Microfluidic design

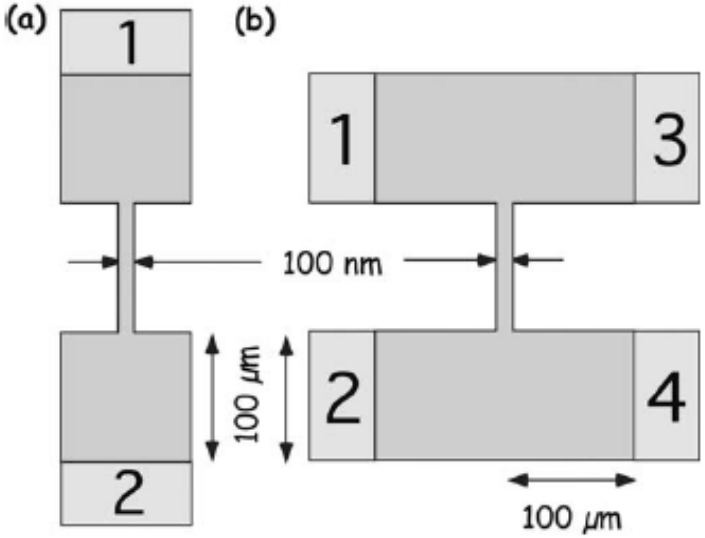

Fig. 5a, b Two microfluidic designs. The access holes are labeled *1–4*. Typical values for the dimensions of the channels are: cross sections 100 nm×100 nm and length 100 μm for the small channels and 1 μm×100 μm×200 μm (depth×width×length) for the larger ones. The submicron channels are not drawn to scale. Assume standard conditions with an applied pressure difference of 100 kPa and water at 20°C so that the viscosity $\eta = 10^{-3}$ kg m^{-1} s^{-1}. The cycle time is defined as the time it takes to introduce a new liquid and pump it through the nanochannel. For a simple two-reservoir device (a), all liquid in the large-channel area must be pumped through the nanochannel until the next liquid sample can be introduced giving a cycle time of the order of an hour. In the double T-junction design (b), the liquid is first moved quickly in the microchannel into position close to the nanoscale channels by applying a pressure difference from *left* to *right* in the *upper channel* between *reservoirs 1* and *3*. Then the required amount is passed through the nanochannels by applying a pressure difference between the *upper reservoirs 1* and *3* on one side and *lower reservoirs 2* and *4* on the other. This gives us a cycle time of less than a second, which is more than three orders of magnitude faster

Anal Bioanal Chem (2004) 378 : 1678–1692

Electrokinetic Flow

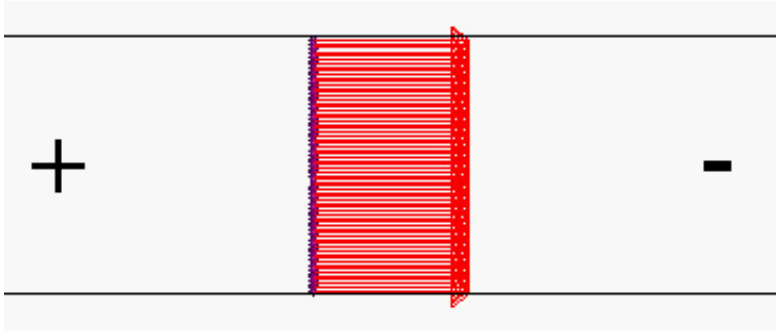

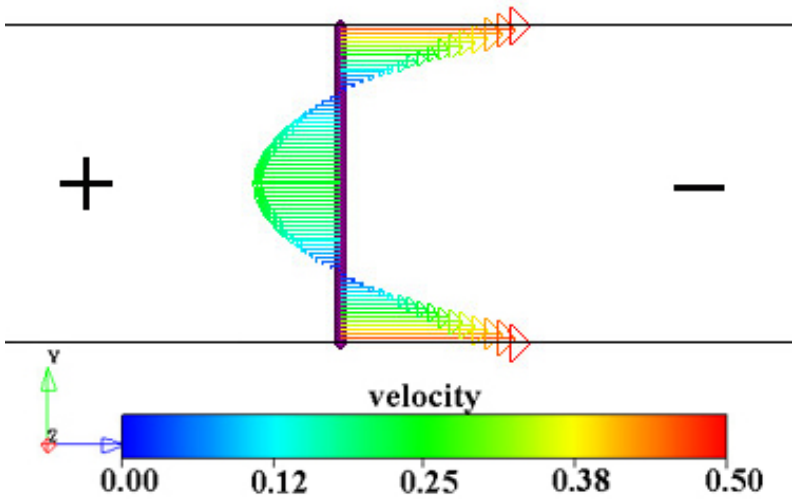

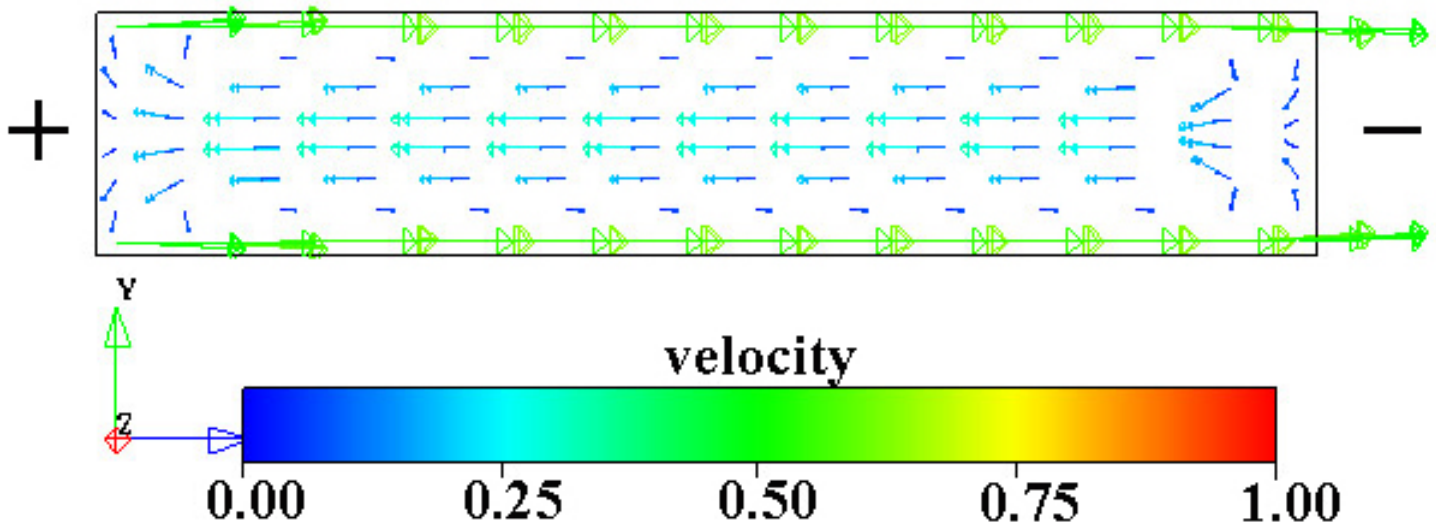

Electrophoresis

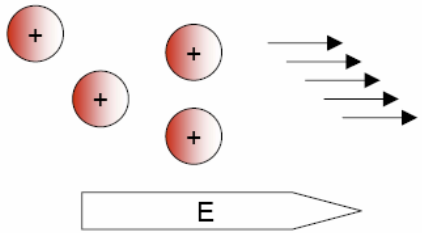

The ion will feel an electrical force:

$$F_{electric} = qE$$

and a frictional force

$$F_{friction} = vf,$$

where $f = 6\pi\eta a$. In a constant electric field, the forces will balance out, thus we can define a steady-state velocity as

$$v = \frac{qE}{f} \qquad (1)$$

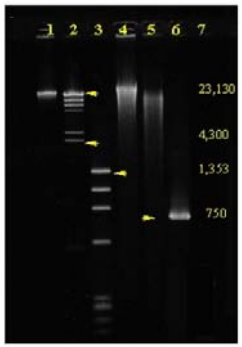

We can also define an ion's electrophoretic mobility, μ, as

$$\mu = \frac{v}{E} = \frac{q}{f} \qquad (2)$$

For a spherical molecule of charge ze and radius a

$$\mu = \frac{ze}{6\pi\eta a} \qquad (3)$$

Electroosmotic flow

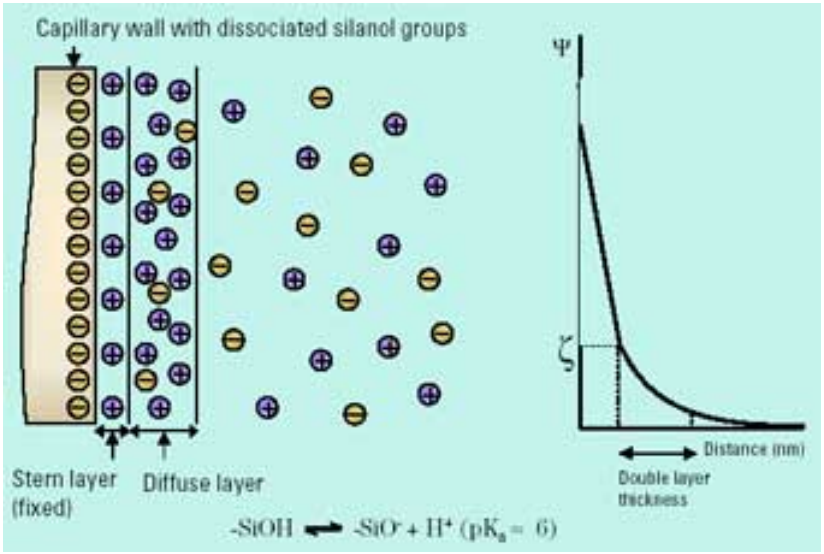

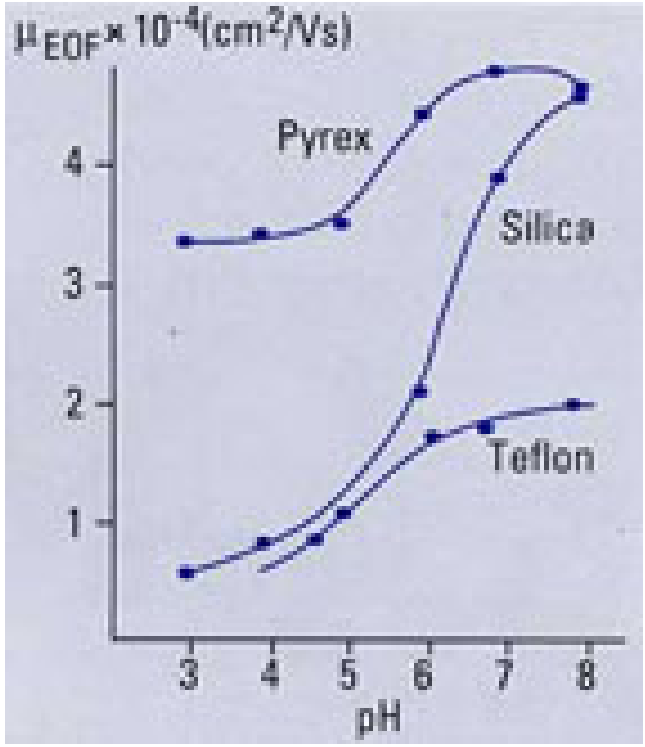

Microfluidics - basics

J. P. Kutter
µ-TAS group
DTU

Electroosmotic flow

Interfacial phenomenon based on a charge separation which leads to a potential at the shear plane between a fixed and a mobile ion layer = ζ-potential

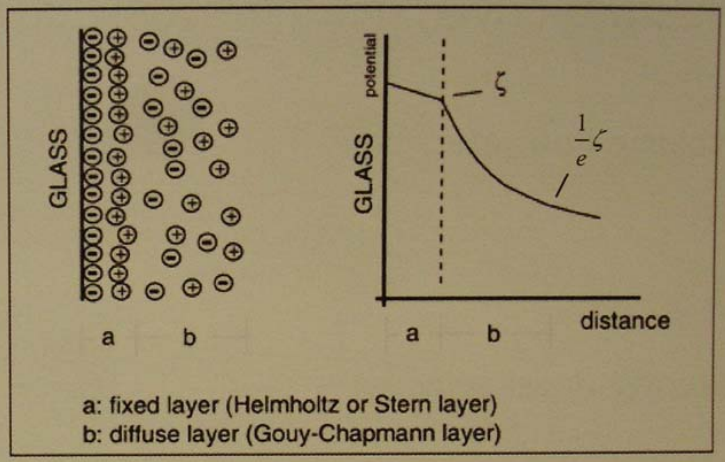

a: fixed layer (Helmholtz or Stern layer)
b: diffuse layer (Gouy-Chapmann layer)

Electroosmotic velocity

$$u_{eo} = \mu_{eo} E = \frac{\zeta \varepsilon}{4\pi\eta} E$$

μ_{eo}: electroosmotic mobility;
E: field strength; ε: dielectric constant

Double layer thickness

$$\delta = \sqrt{\frac{\varepsilon RT}{2F^2 z^2 c}}$$

R: gas constant; F: Faraday constant
z: charge; c: concentration

Electroosmotic flow

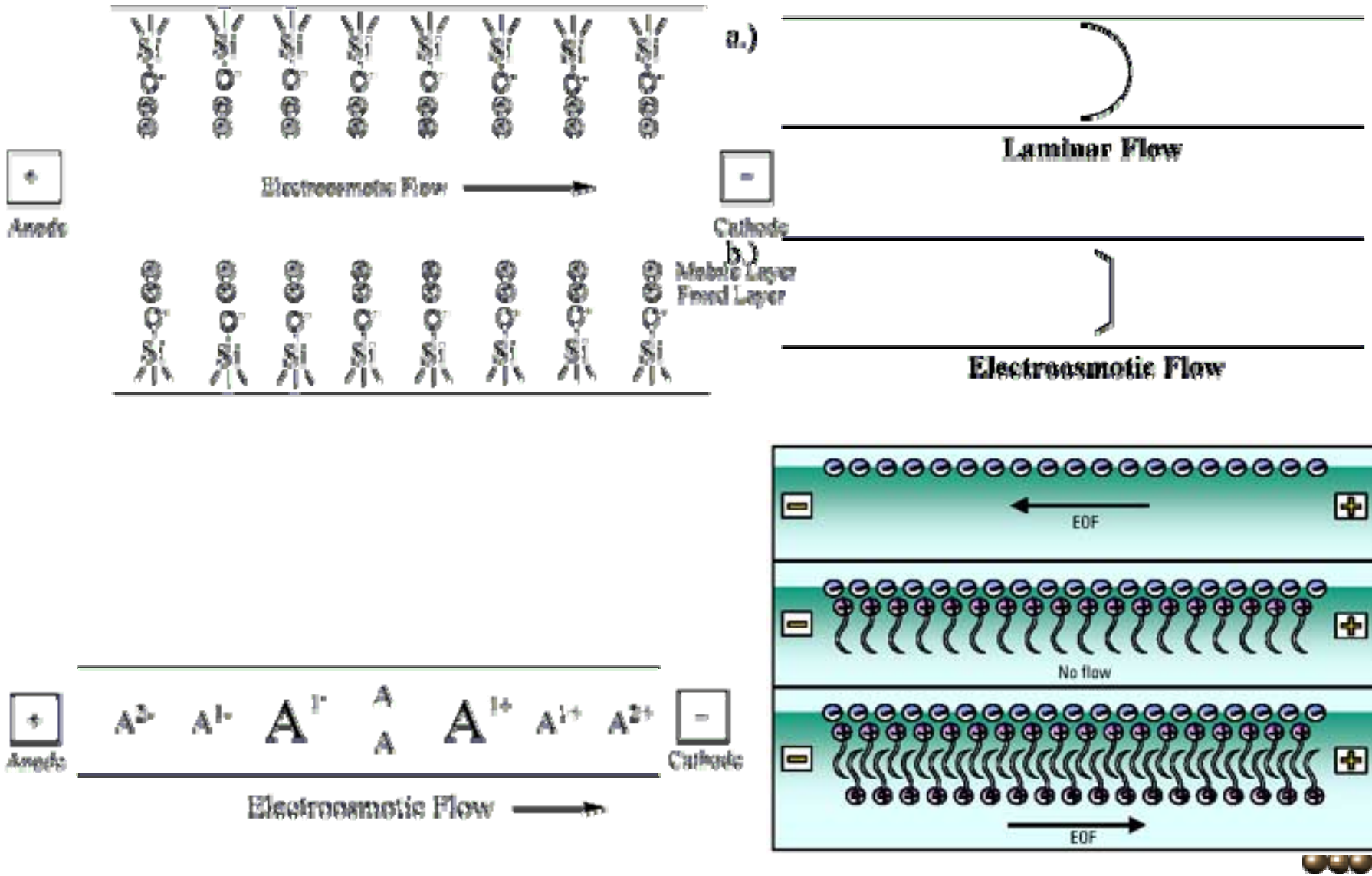

Dielectrophoresis

$$F_{dep} = \frac{\pi a^2 b}{3} \epsilon_m \mathrm{Re}\left\{\frac{\epsilon_p^* - \epsilon_m^*}{\epsilon_m^*}\right\} \nabla \left|\vec{E}\right|^2$$

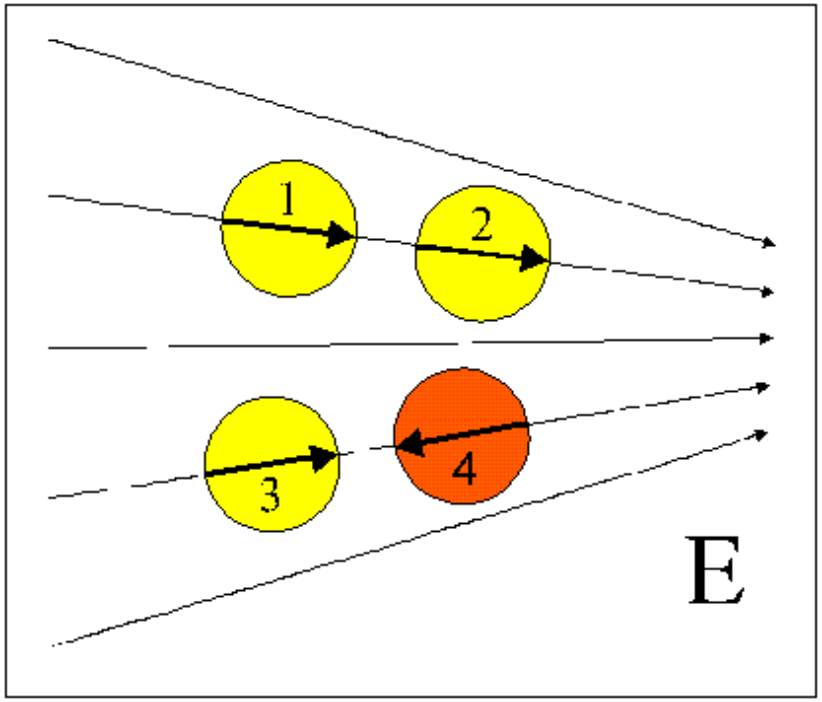

F_{DEP} =

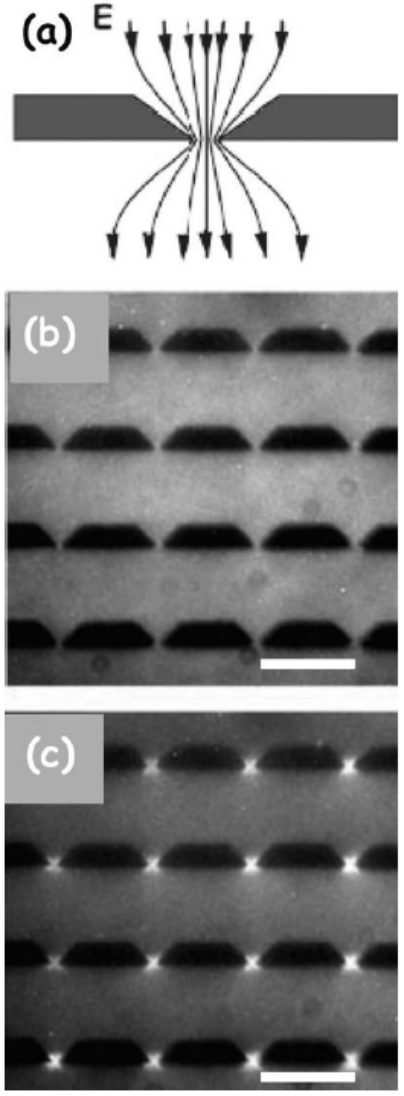

On-chip manipulation of free droplets

NATURE | VOL 426 | 4 DECEMBER 2003 |

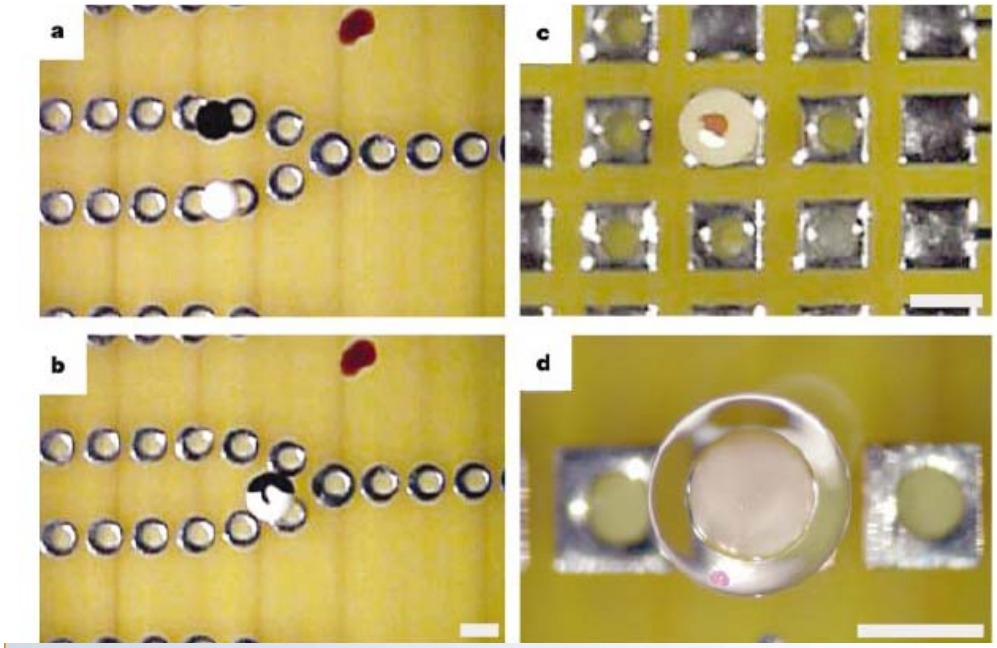

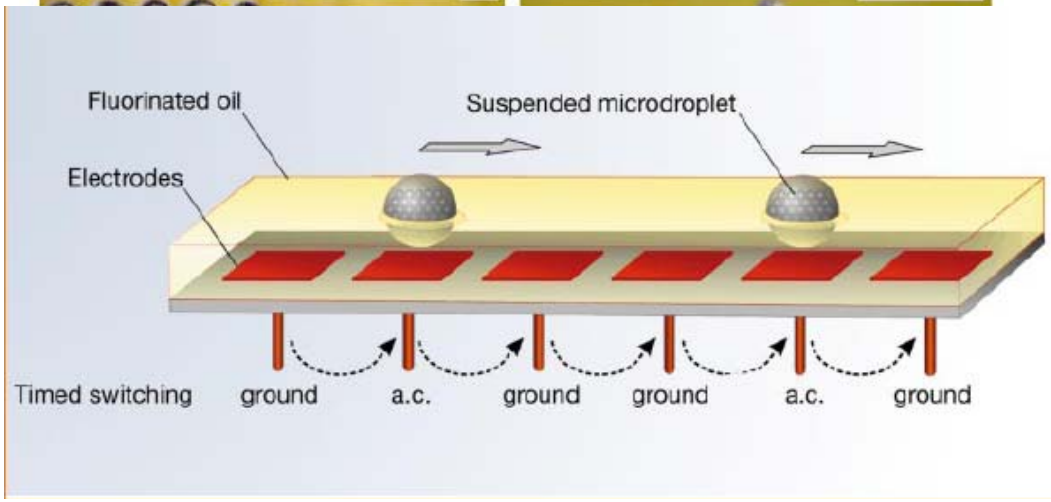

Dimensionless Numbers

TABLE I. Dimensionless numbers used in this review.

Re	Reynolds	$\frac{\rho U_0 L_0}{\eta}$	inertial/viscous	Eq. (5)
Pe	Péclet	$\frac{U_0 L_0}{D}$	convection/diffusion	Eq. (7)
Ca	capillary	$\frac{\eta U_0}{\gamma}$	viscous/interfacial	Eq. (19)
Wi	Weissenberg	$\tau_p \dot{\gamma}$	polymer relaxation time/shear rate time	Eq. (24)
De	Deborah	$\frac{\tau_p}{\tau_{\text{flow}}}$	polymer relaxation time/flow time	Eq. (25)
El	elasticity	$\frac{\tau_p \eta}{\rho h^2}$	elastic effects/inertial effects	Eq. (26)
Gr	Grashof	$\frac{\rho U_b L_0}{\eta}$	Re for buoyant flow	Eq. (30)
Ra	Rayleigh	$\frac{U_b L_0}{D}$	Pe for buoyant flow	Eq. (29)
Kn	Knudsen	$\frac{\beta}{L_0}$	slip length/macroscopic length	Eqs. (36) and (38)

Reynolds Number

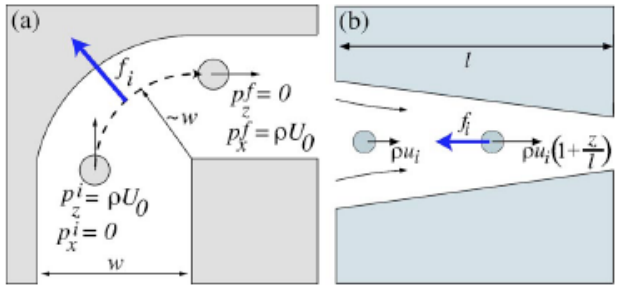

FIG. 3. (Color in online edition) Inertial forces exerted by accelerating fluid elements. (a) A small fluid element rounding a corner loses ρU_0 of momentum during the time $\tau_0 \sim w/U_0$ required to turn the corner, giving a centrifugal force density of order $f_i \sim \rho U_0^2/w$. (b) A fluid element flowing through a contraction with velocity gradient $du/dz \sim U_0/l$ gains momentum density at a rate $f_i \sim \rho U_0^2/l$. In both cases, the inertial force exerted on the fluid is equal and opposite to the force required to accelerate each fluid element, and is the same for flows in either direction.

turn time $\tau_0 \sim w/U_0$,

corner loses momentum density ρU_0

force density $f_i \sim \rho U_0/\tau_0 = \rho U_0^2/w$.

velocity increases as $u \sim U_0(1+z/l)$

$$f_i \sim \rho \frac{du}{dt} = \rho U_0 \frac{du}{dz} \sim \frac{\rho U_0^2}{l}.$$

gradients in viscous stress

$f_v \sim \eta U_0/L_0^2$, where L_0 is a typical length scale

$$\frac{f_i}{f_v} = \frac{\rho U_0 L_0}{\eta} \equiv \mathrm{Re}$$

velocities of 1 μm/s–1 cm/s

channel radii of 1–100 μm

→ $\mathcal{O}(10^{-6})$ and $\mathcal{O}(10)$

Water Properties

TABLE II. Physical properties of water at 20 °C and 1 atm pressure (Lide, 1999).

Density	ρ	1.0 g/cm^3
Shear viscosity	η	1.0×10^{-2} g/cm s
Kinematic viscosity	ν	1.0×10^{-2} cm^2/s
Surface tension (in air)	γ	73 g/s^2
Thermal variation of γ	$d\gamma/dT$	–0.15 g/s^2 °C
Thermal diffusivity	κ_H	1.4×10^{-3} cm^2/s
Compressibility	α_ρ	-4.6×10^{-11}/ba
Coefficient of thermal expansion	α_T	2.1×10^{-4}/°C

TABLE III. Typical diffusivities for various tracers in water at room temperature.

	Characteristic diffusivities	
Particle	Typical size	Diffusion constant
Solute ion	10^{-1} nm	2×10^3 μm^2/s
Small protein	5 nm	40 μm^2/s
Virus	100 nm	2 μm^2/s
Bacterium	1 μm	0.2 μm^2/s
Mammalian/human cell	10 μm	0.02 μm^2/s

Forward (advective) vs. transverse (diffusive) transport

Peclet number:

$$Pe = \frac{ud}{D}$$

Dispersion: distortion of a plug due to various processes

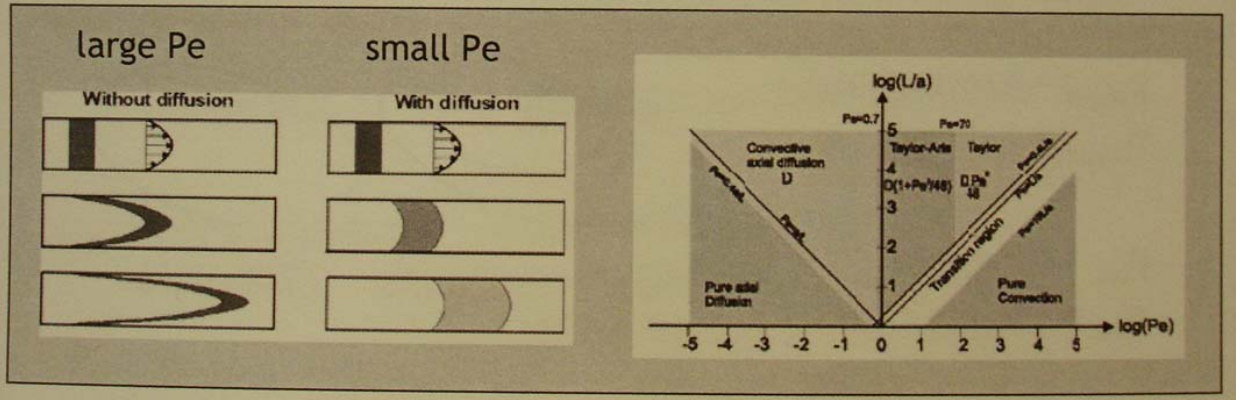

figures courtesy of F. R. Hansen, MIC

Peclet Number

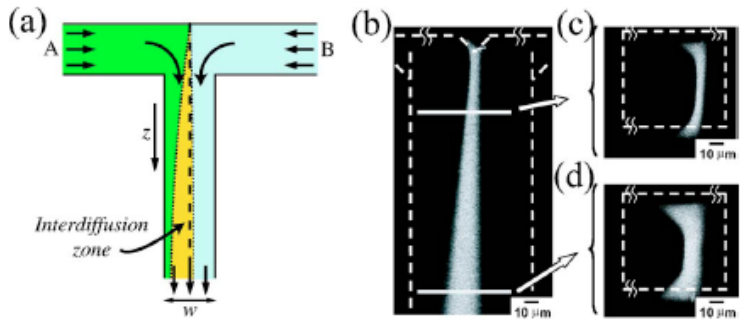

FIG. 5. (Color in online edition) (a) The microfluidic T sensor (Kamholz *et al.*, 1999). Different fluids are brought together at a T junction to flow alongside each other down the channel. A simple estimate suggests that the interdiffusion zone spreads diffusively, with the square root of time (or downstream distance), although (b)–(d) show this naive argument to break down near the "floor" and "ceiling" of the channel. Confocal microscopy reveals the three-dimensional nature of the spreading of the interface in the T sensor (Ismagilov *et al.*, 2000). (b) Fluorescent tracers mark reactions occurring in the interdiffusion zone, here seen from above. (c), (d) The no-slip nature of the top and bottom walls of the channel affect the flow profile, so that tracer molecules near the boundaries diffuse and spread with $z^{1/3}$, rather than $z^{1/2}$. Reprinted with permission from Ismagilov *et al.*, 2000. ©2000, AIP.

the channel is homogenized? A simple estimate requires the particles or molecules to diffuse across the entire channel, giving a time $\tau_D \sim w^2/D$, where w is the width of the channel. During this time, the stripe will have moved a distance $Z \sim U_0 w^2/D$ down the channel, so that the number of channel widths required for complete mixing would be of order

$$\frac{Z}{w} \sim \frac{U_0 w}{D} \equiv \mathrm{Pe}. \qquad (7)$$

100-μm channel at 100 μm/s

Pe ~250 channel widths (approximately 2.5 cm and 4 min)

Capillary Number

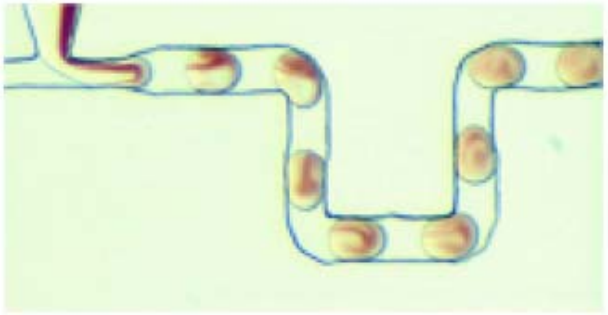

FIG. 16. (Color in online edition) Chaotic advection in a pumped droplet. A droplet driven down a channel experiences a dipolar, circulating flow; when the channel changes direction, the axis of the dipole changes as well. Alternating dipolar flows drive rapid mixing by chaotic advection, with mixing lengths that vary logarithmically with Pe. Reprinted with permission from Song, Bringer, *et al.*, 2003. ©2003, AIP.

face (Taylor, 1934). Capillary stresses of magnitude γ/R balance viscous stresses $\eta U_0/h$, giving a characteristic droplet size

$$R \sim \frac{\gamma}{\eta U_0} h = \frac{h}{\mathrm{Ca}}. \tag{15}$$

Here we have introduced the capillary number

$$\mathrm{Ca} = \frac{\eta U_0}{\gamma}, \tag{16}$$

a dimensionless parameter found whenever interfacial stresses compete with viscous stresses.

Capillary Number

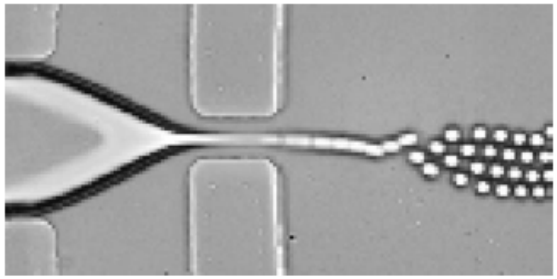

FIG. 14. Capillary instabilities in a microfluidic two-phase flow. A stream of water flows between streams of oil and is geometrically focused into a narrow cylindrical jet. The jet is destabilized by the Rayleigh-plateau instability and forms small, monodisperse droplets. Reprinted with permission from Ar

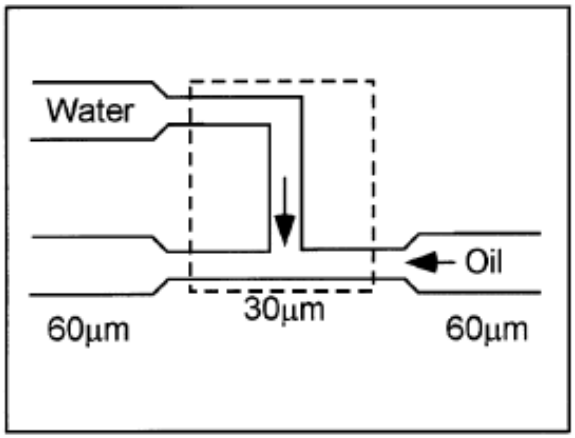

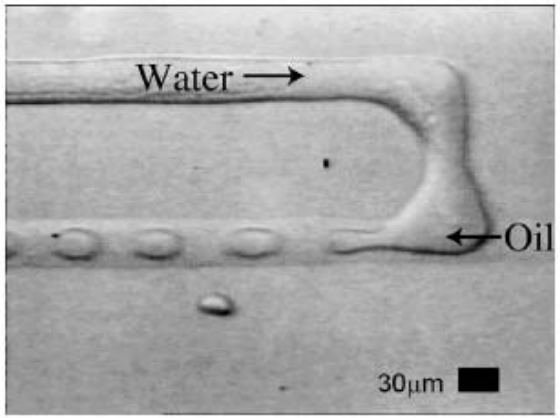

FIG. 15. Monodisperse microdroplet generation in a simple microfluidic device. The interface between flowing immiscible fluids is driven by competing stresses: viscous shear stresses tend to extend and drag the interface, whereas surface tension tends to reduce the interfacial area. The competition between the two leads to drop sizes (scaled by the channel height h) of order $R \sim \mathrm{Ca}^{-1}$. Adapted with permission from Thorsen *et al.*, 2001.

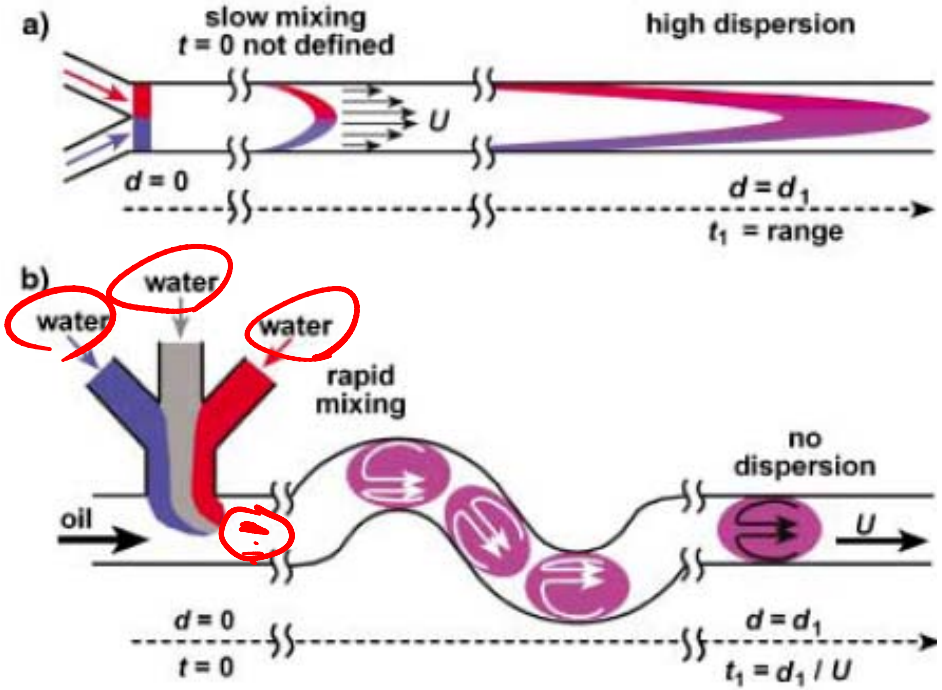

Figure 1. Schematic comparison of a reaction A + B conducted in a standard pressure-driven microfluidic system device (a) and in the microfluidic device described here (b). a) Reaction time $t \neq d/U$. b) Reaction time $t = d/U$. Two aqueous reagents (red, A and blue, B) can form laminar streams separated by a gray "divider" aqueous stream in a microchannel. When the three streams enter the channel with a flowing immiscible fluid, they form droplets (plugs). The reagents come into contact as the contents of the droplets are rapidly mixed. Internal recirculation within plugs flowing through channels of different geometries is shown schematically by arrows.

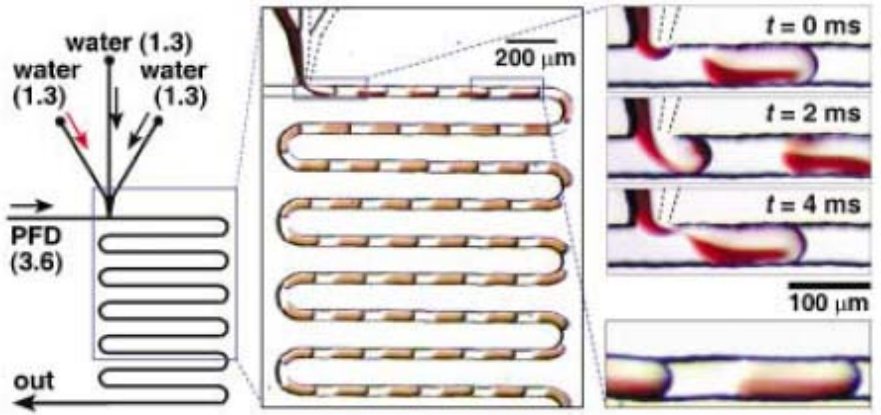

Figure 2. Spontaneous formation of uniform plugs out of multiple aqueous streams. Left: Schematic diagram of the microchannel network. Volumetric flow rates for all streams (in $\mu L\,min^{-1}$) are given in parenthesis. Middle: Microphotograph (10 μs exposure) of plug formation and transport. Right: Magnified microphotographs (10 μs exposure) of the plug-forming region at different time points. All microchannels had $50 \times 50\ \mu m^2$ cross sections. Total flow rate in the main channel: $7.5\ \mu L\,min^{-1}$ ($50\ mm\,s^{-1}$ average flow velocity); $Re \sim 2.5$ (water), ~0.93 (PFD). PFD here stands for a 10:1 mixture of perfluorodecaline and $C_6F_{11}C_2H_4OH$. Red stream: solution of $[Fe(SCN)_x]^{(3-x)+}$ prepared by mixing 0.067 M $Fe(NO_3)_3$ with 0.2 M KSCN; colorless streams: 0.2 M KNO_3.

Sieving

- Ogston sieving
  - R < d
- Entropic trapping
  - R>d
- Electrostatic sieving
  - Debye length

- pI < pH ➔ positively charged
- pI > pH ➔ negatively charged

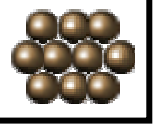

DNA Length

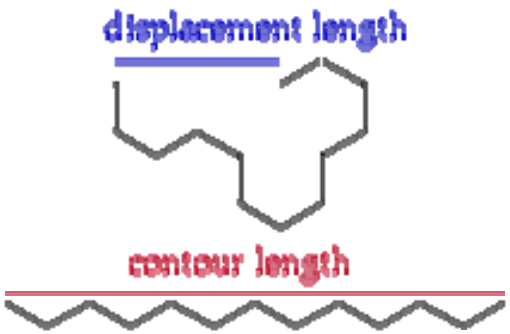

- Contour length
- Persistence length
  - The **persistence length** is a basic mechanical property quantifying the stiffness of a macromolecule of a polymer. It is defined as the length over which correlations in the direction of the tangent are lost.
- Radius of gyration
  - The **radius of gyration** *Rg* describes the distribution of particles (or infinitesimal elements) in a *D*-dimensional space by relating it to an equivalent distribution in a *D*-dimensional sphere, usually a circular (*D*=2) or spherical (*D*=3) distribution
- Kuhn length
  - The **Kuhn length** is a theoretical treatment of a real chain divided into *N* **Kuhn segments** with Kuhn length *b*, so that each Kuhn segments can be thought of as if they are freely joined with each other. The contour length $L = Nb$

Microfluidics - basics

J. P. Kutter
µ-TAS group
DTU

Electroosmotic flow

Interfacial phenomenon based on a charge separation which leads to a potential at the shear plane between a fixed and a mobile ion layer = ζ-potential

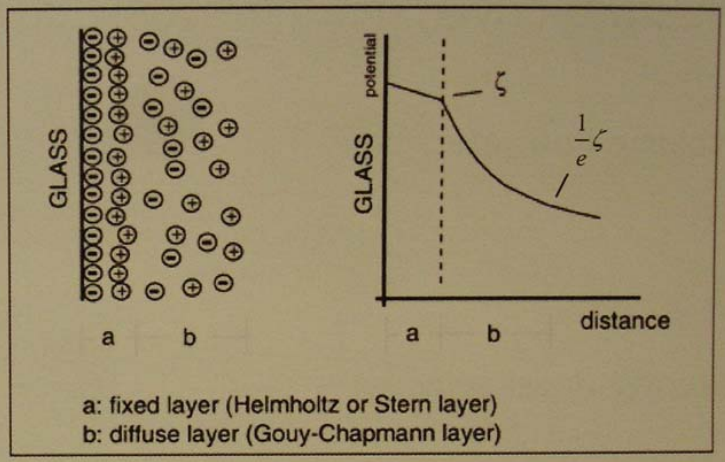

a: fixed layer (Helmholtz or Stern layer)
b: diffuse layer (Gouy-Chapmann layer)

Electroosmotic velocity

$$u_{eo} = \mu_{eo} E = \frac{\zeta \varepsilon}{4\pi\eta} E$$

μ_{eo}: electroosmotic mobility;
E: field strength; ε: dielectric constant

Double layer thickness

$$\delta = \sqrt{\frac{\varepsilon RT}{2F^2 z^2 c}}$$

R: gas constant; F: Faraday constant
z: charge; c: concentration

Debye Strength

$$I = \frac{1}{2}\sum_{i=1}^{n} c_i z_i^2$$

1 M NaCl => 0.5*1*1^2+0.5*1*1^2=1M

$$\lambda_D = \sqrt{\frac{\varepsilon_0 \varepsilon_r k T}{2 N_A e^2 I}}$$

$$\varepsilon_0 = \frac{1}{c^2 \mu_0} \approx 8.8541878176 \times 10^{-12}\ \mathrm{F/m}\ (\text{or}\ \mathrm{C^2/(J\ m)}),$$

80.1

5x TBE => I = ~130 mM ➔ Debye Length = 0.84 nm
0.05 x TBE => I = 1.3 mM ➔ Debye Length = 8.4 nm

Application of nanofluidic channels

- Single cell studies
  - E-coli: 10 fL
  - Eukaryotic cell: 10 pL
- Control factor
  - DNA-protein interaction
- Genetic contents
  - SNP
  - Genome
- Length distribution

A DNA prism for high-speed continuous fractionation of large DNA molecules

nature biotechnology • VOLUME 20 • OCTOBER 2002

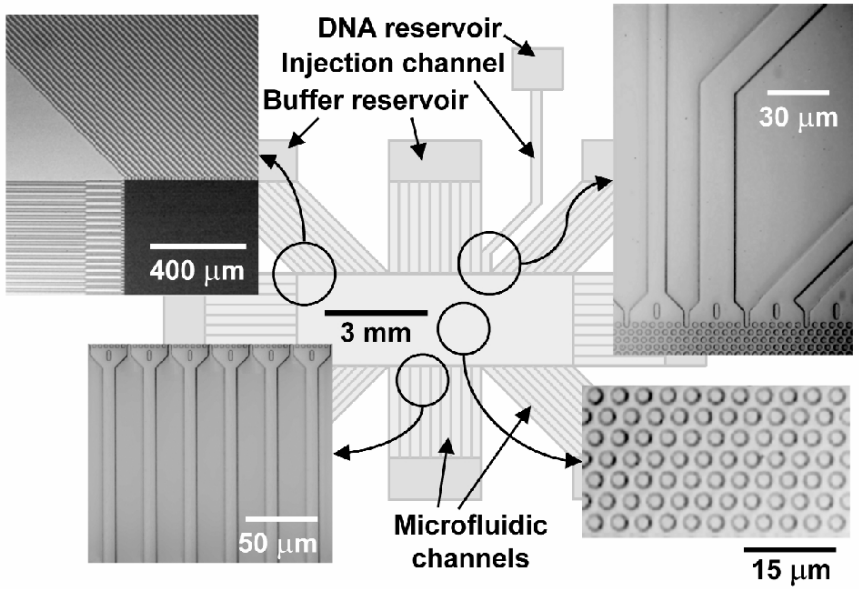

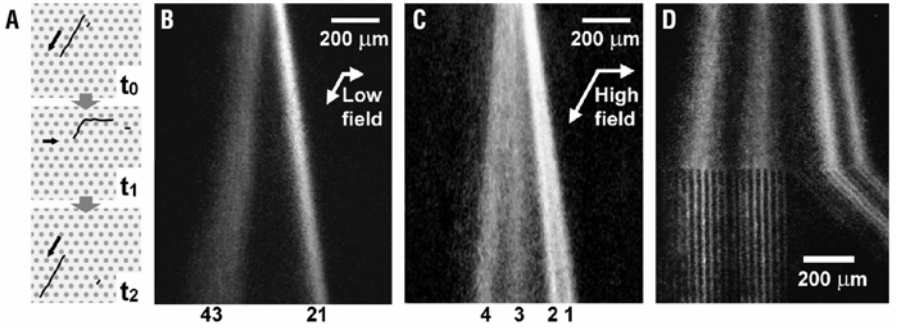

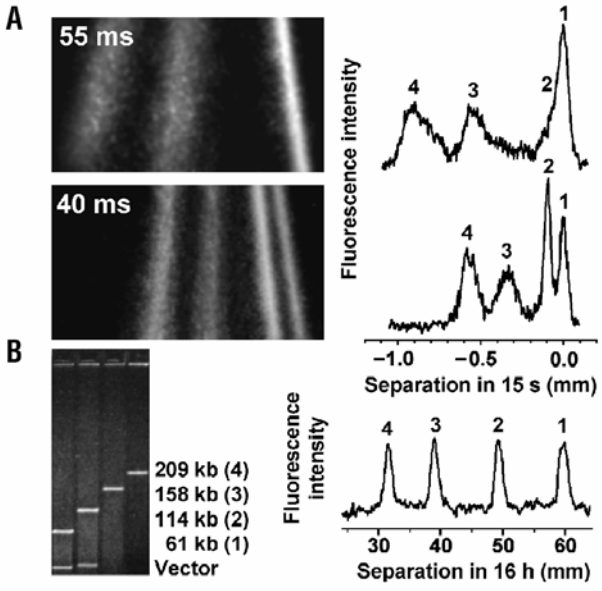

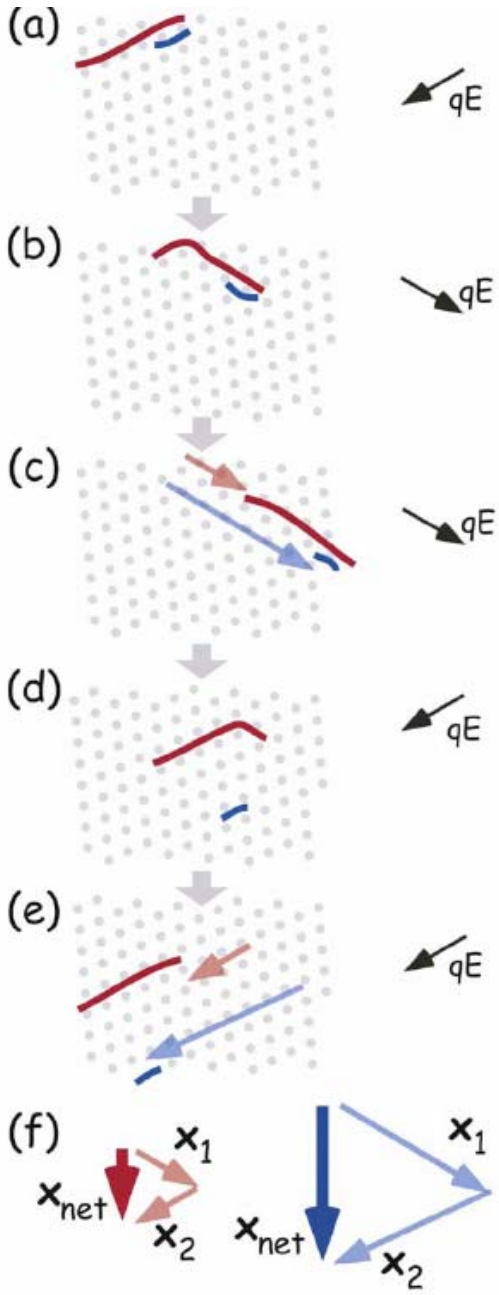
(a)
qE
(b)
qE
(c)
qE
(d)
qE
(e)
qE
(f)
x1
xnet
x2
x1
xnet
x2

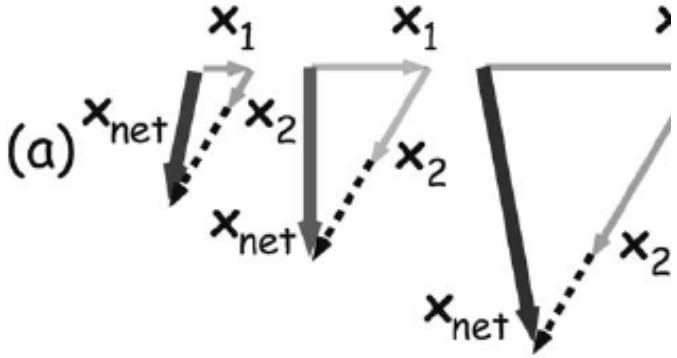
(a)
x1
xnet
x2
x1
x2
xnet
x2
xnet


(b)

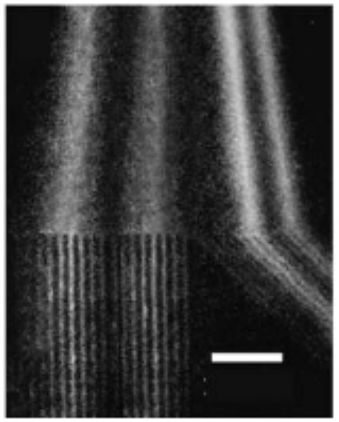
(c)

Continuous Particle Separation Through Deterministic Lateral Displacement

SCIENCE VOL 304 14 MAY 2004

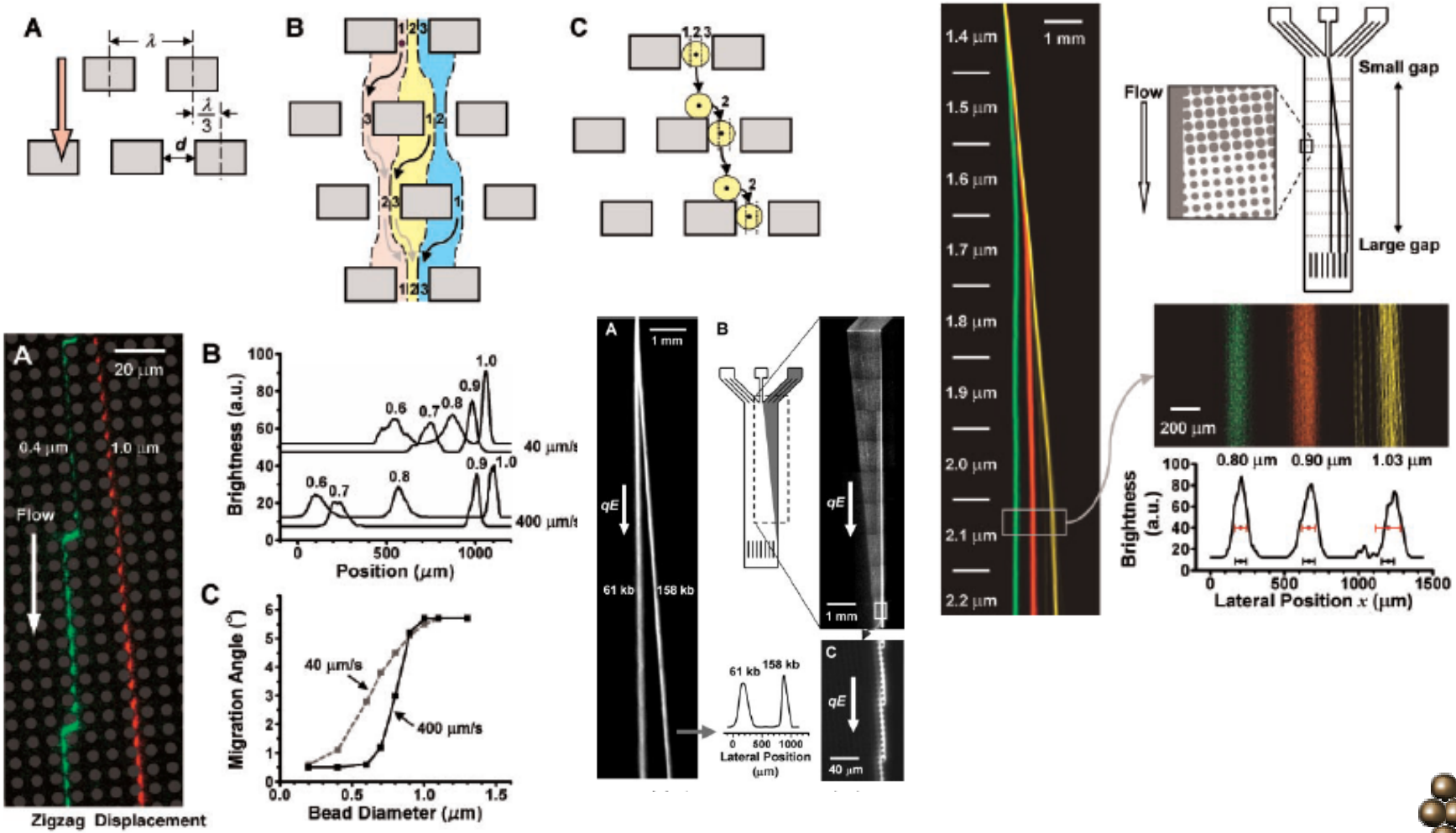

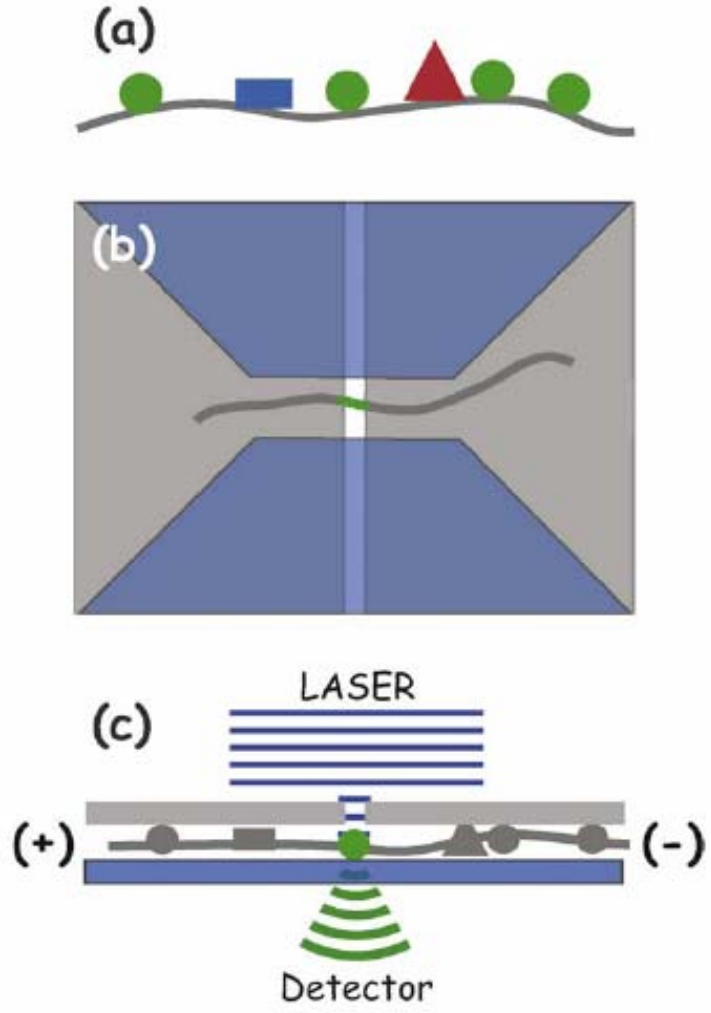
(a)
(b)
(c)
LASER
(+)
(-)
Detector

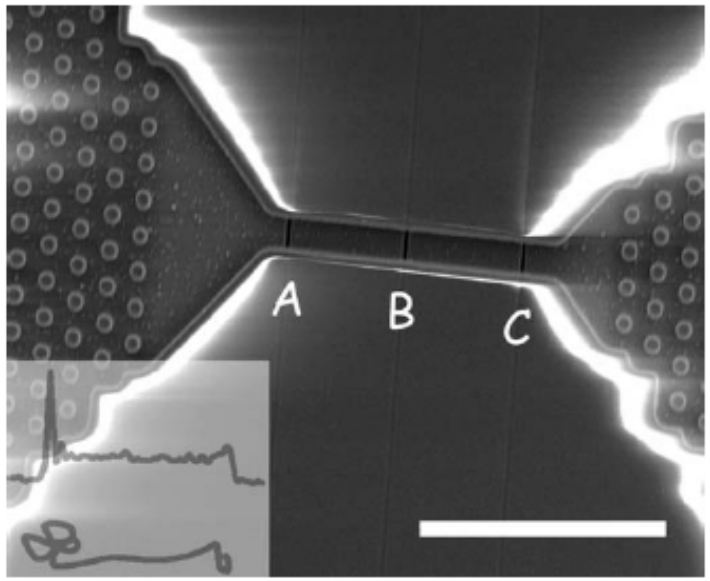
A
B
C

Separation of Long DNA Molecules in a Microfabricated Entropic Trap Array

12 MAY 2000 VOL 288 SCIENCE

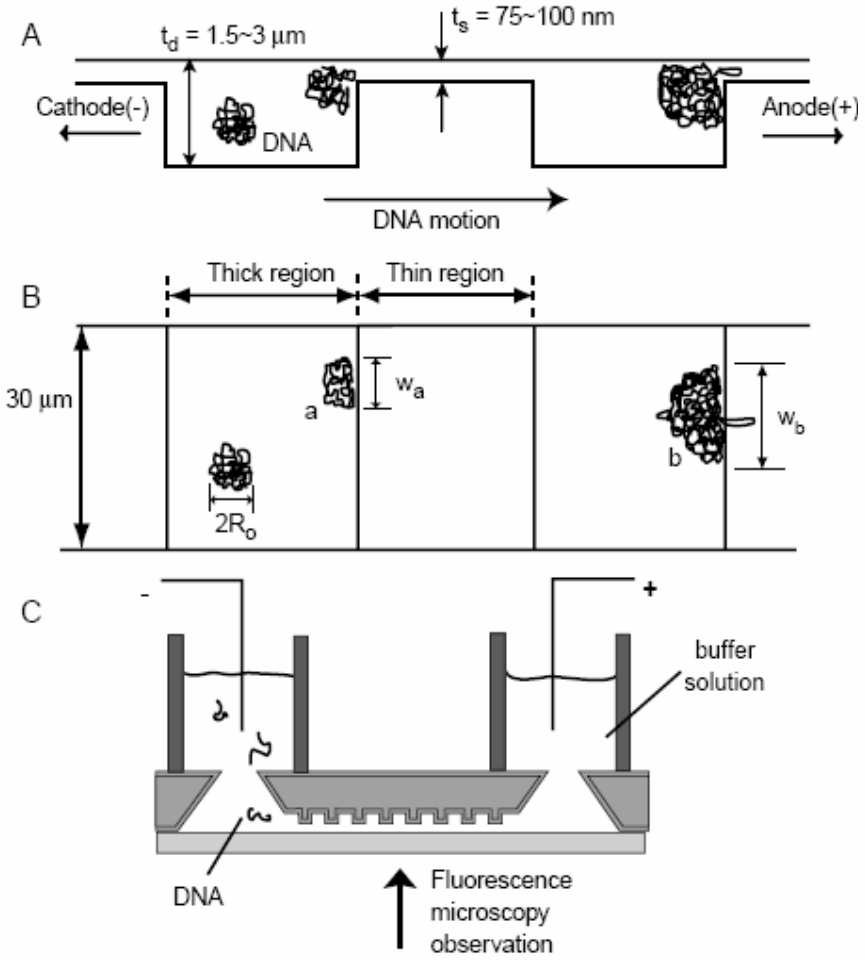

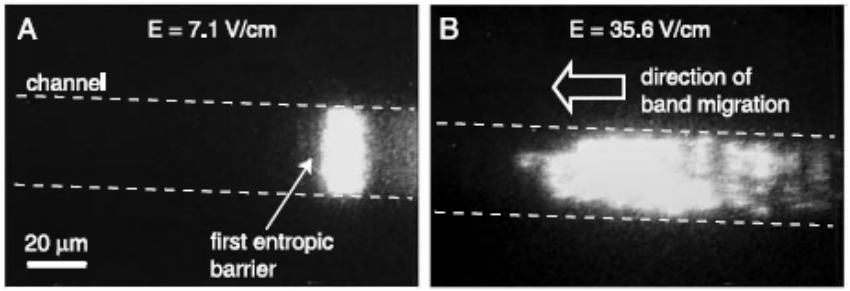

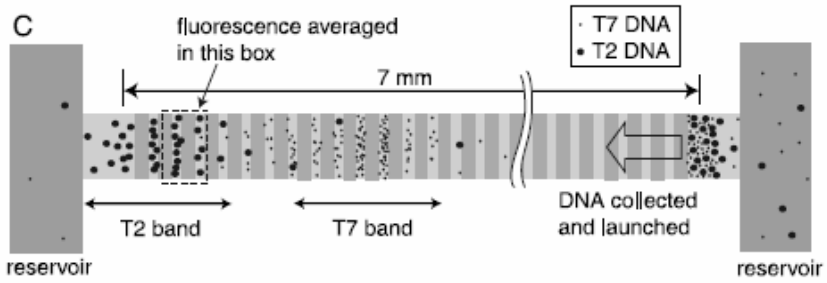

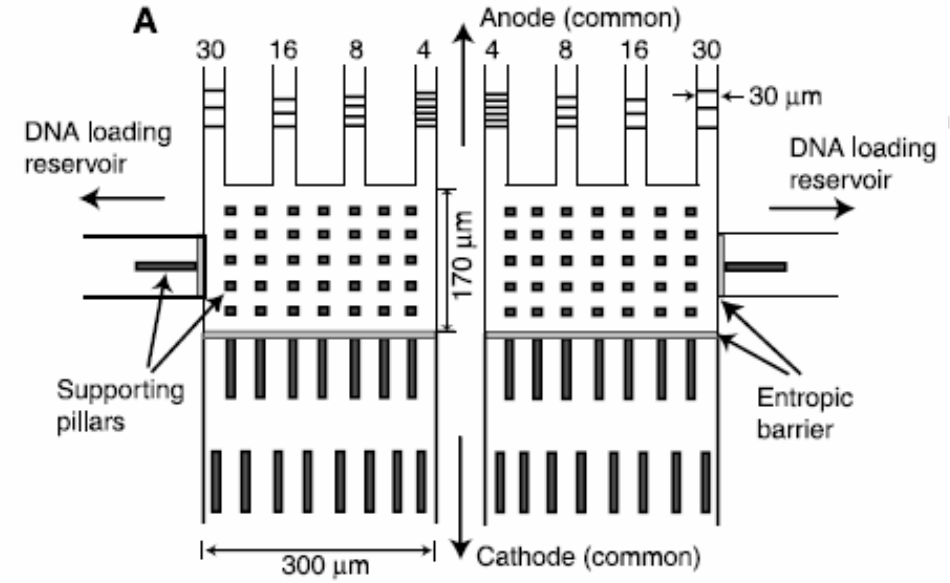
A
Anode (common)
30
16
8
4
4
8
16
30
30 µm
DNA loading reservoir
DNA loading reservoir
170 µm
Supporting pillars
Entropic barrier
300 µm
Cathode (common)

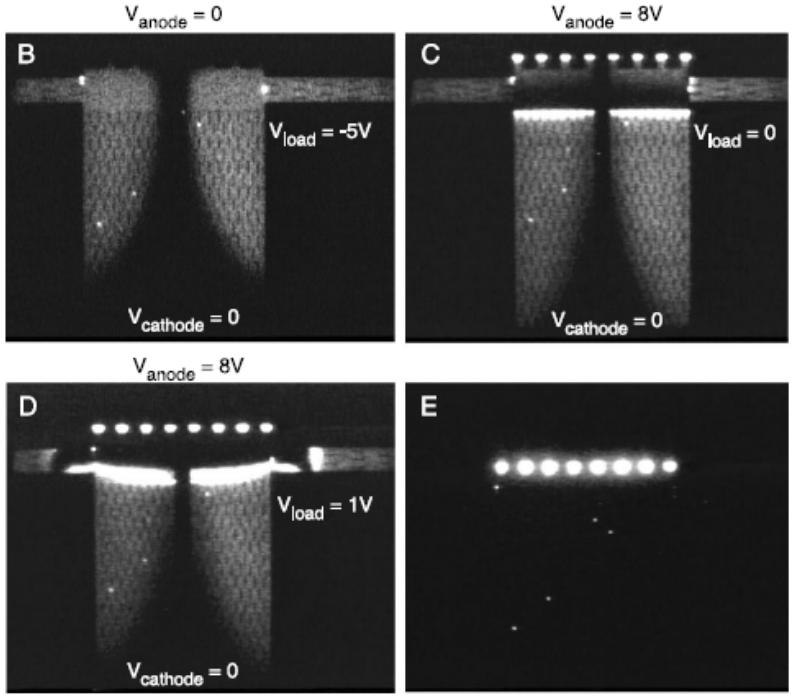
V anode = 0
B
V load = -5V
V cathode = 0
V anode = 8V
C
V load = 0
V cathode = 0
V anode = 8V
D
V load = 1V
V cathode = 0
E

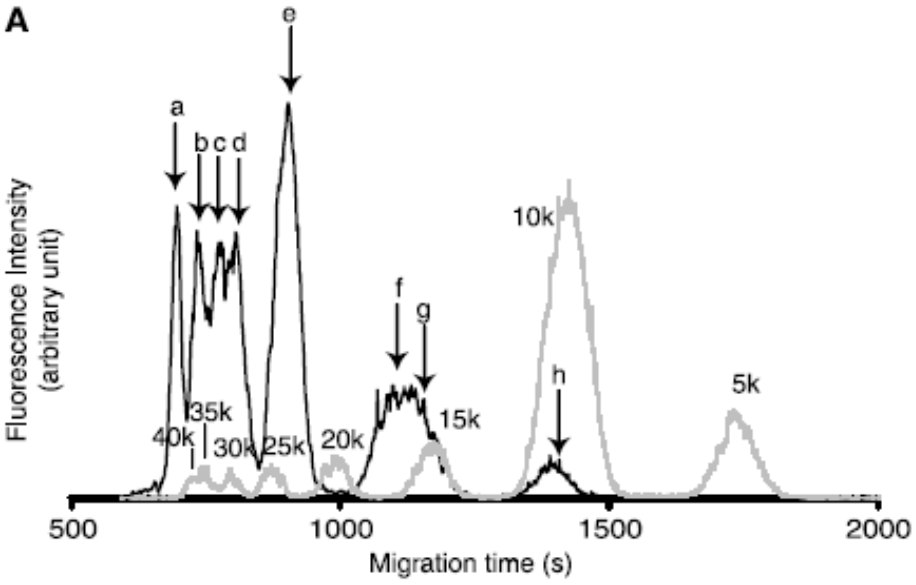
A
a
b c d
e
f
g
h
10k
5k
40k
35k
30k
25k
20k
15k
Fluorescence Intensity (arbitrary unit)
500
1000
1500
2000
Migration time (s)

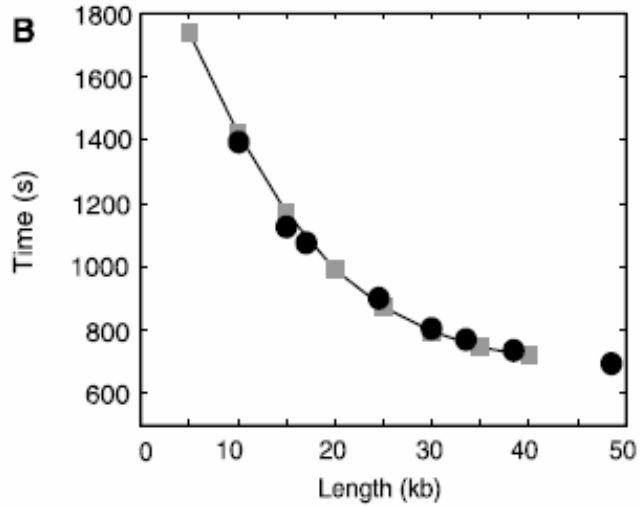
B
1800
1600
1400
1200
1000
800
600
Time (s)
0
10
20
30
40
50
Length (kb)

Nanofilter array chip for fast gel-free biomolecule separation

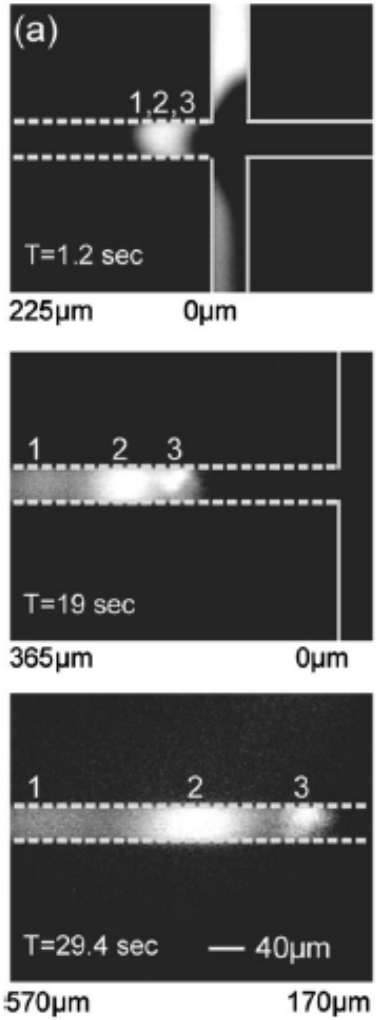

(b) SDS-Protein

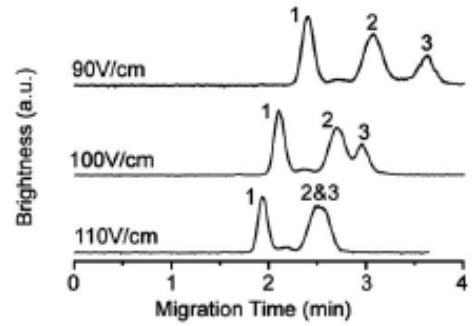

	$R_{S,12}$	$R_{S,23}$	N_1	H_1	N_1/L
90V/cm	2.16	1.61	1523	3.28	$3X10^5$

(c) dsDNA

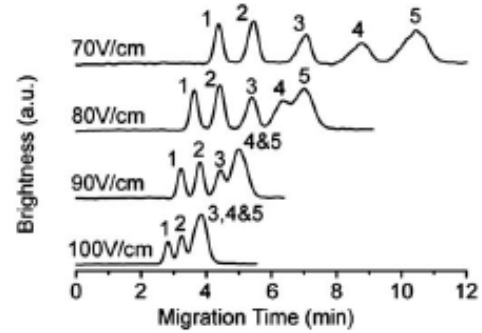

	μ_1	μ_2	μ_5	$R_{S,12}$	$R_{S,25}$
70V/cm	2.72	2.17	1.14	2.17	5.41
100V/cm	2.95	2.57	2.17	1.14	1.05

APPLIED PHYSICS LETTERS **87**, 263902 (2005)

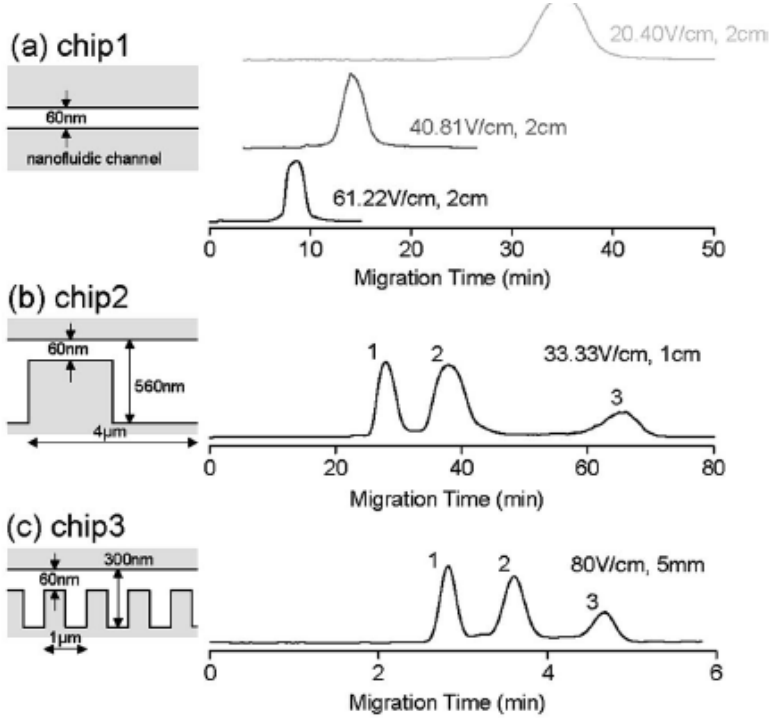

PRL 97, 018103 (2006)

Molecular Sieving in Periodic Free-Energy Landscapes Created by Patterned Nanofilter Arrays

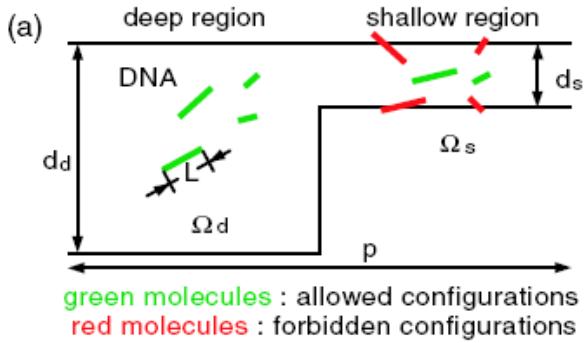

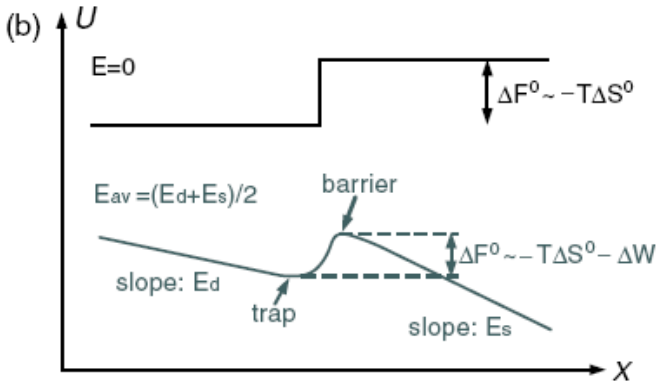

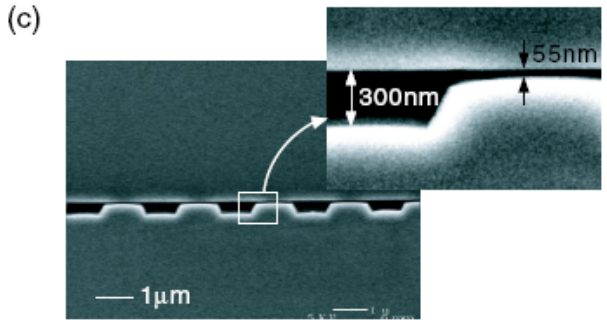

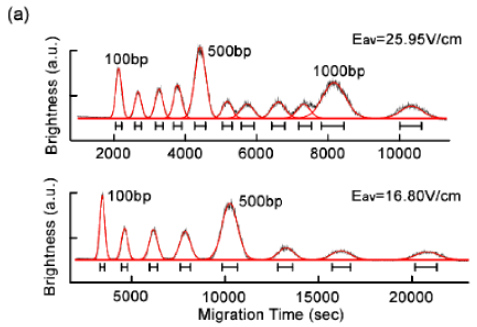

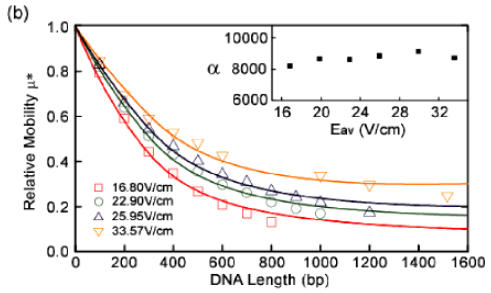

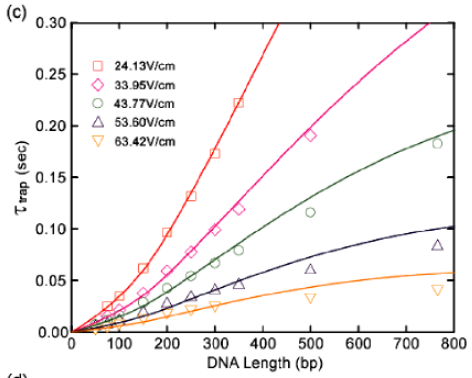

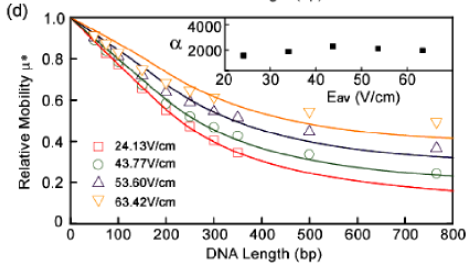

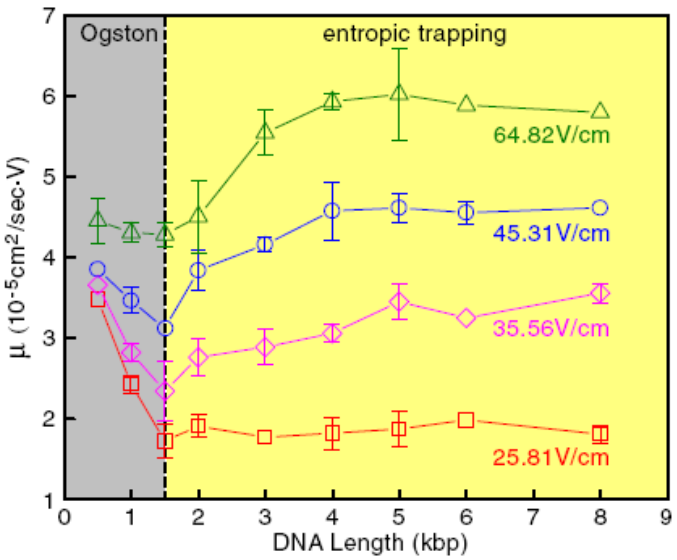

A patterned anisotropic nanofluidic sieving structure for continuous-flow separation of DNA and proteins

nature nanotechnology | VOL 2 | FEBRUARY 2007

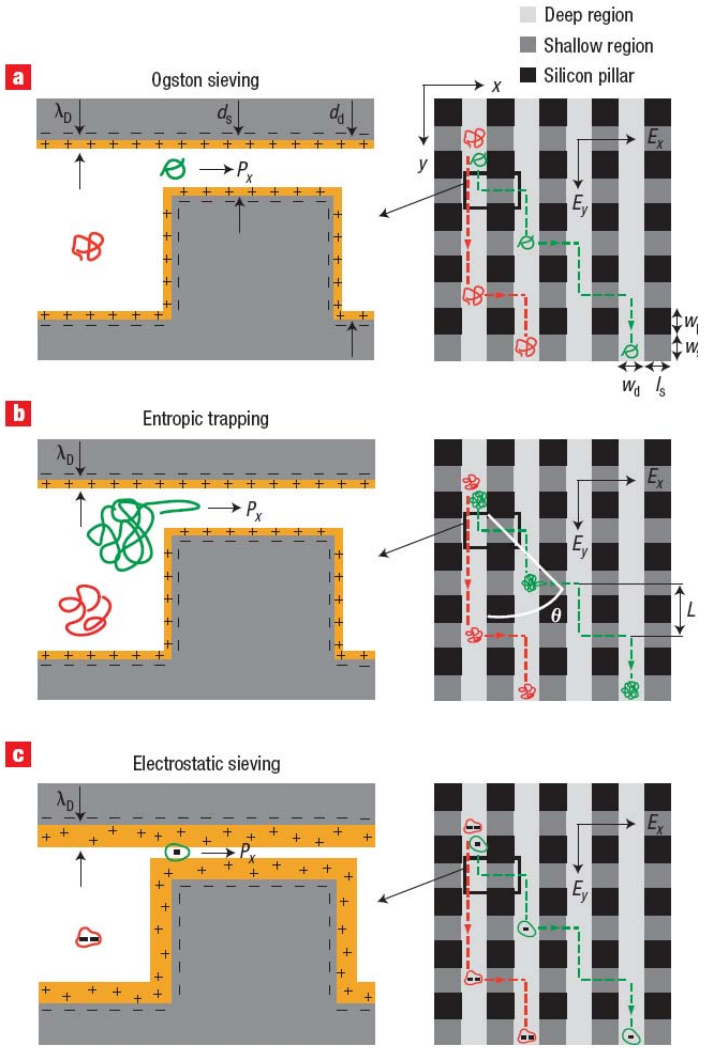

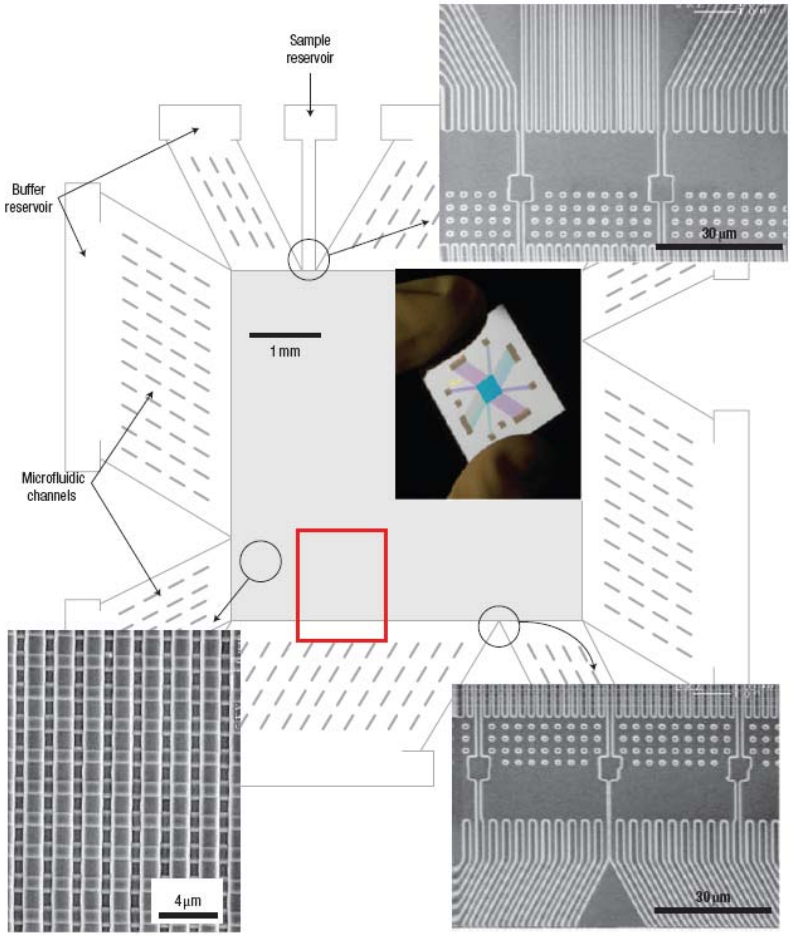

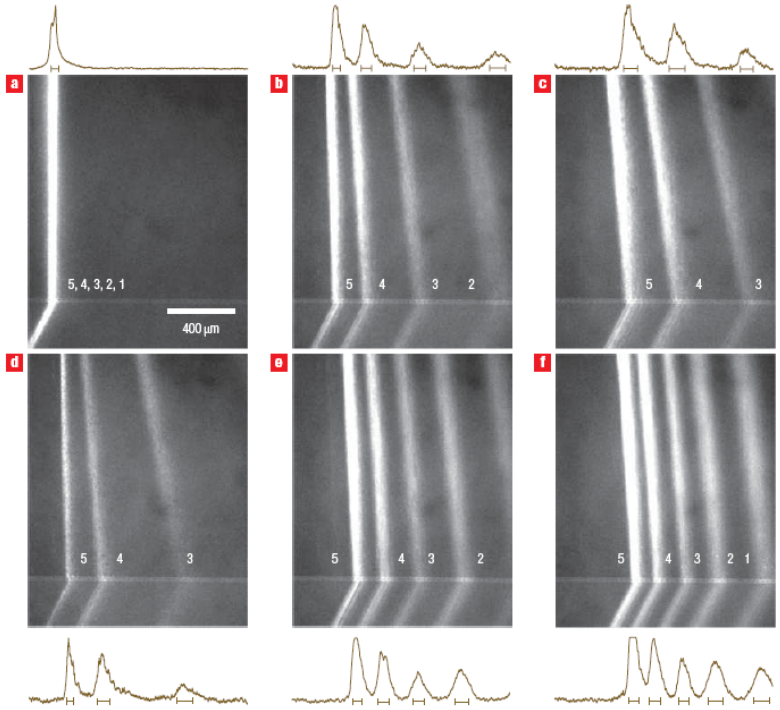
a
b
c
d
e
f
5, 4, 3, 2, 1
400 μm
5 4 3 2
5 4 3
5 4 3 2
5 4 3 2 1

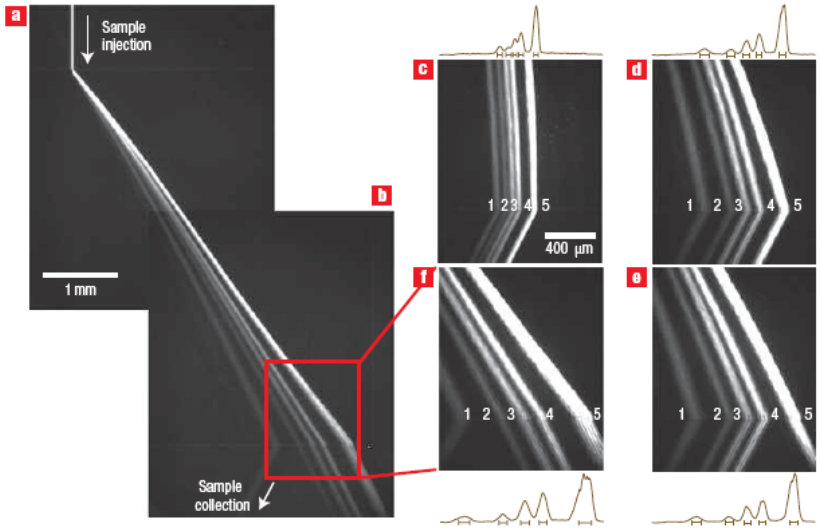
a
Sample injection
1 mm
Sample collection
b
c
1 2 3 4 5
400 μm
d
1 2 3 4 5
e
1 2 3 4 5
f
1 2 3 4 5

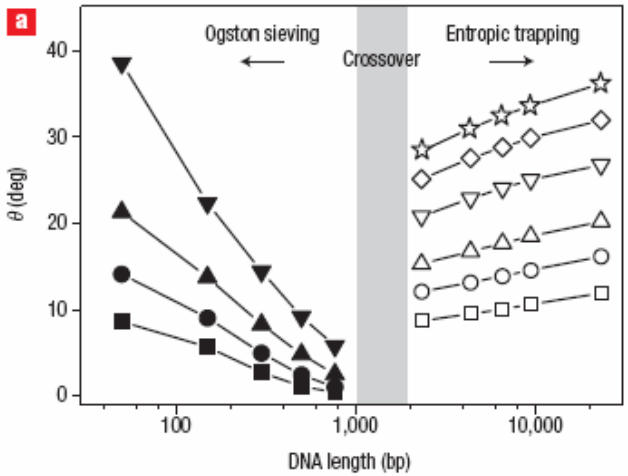
a
Ogston sieving
Crossover
Entropic trapping
θ (deg)
40
30
20
10
0
100
1,000
10,000
DNA length (bp)

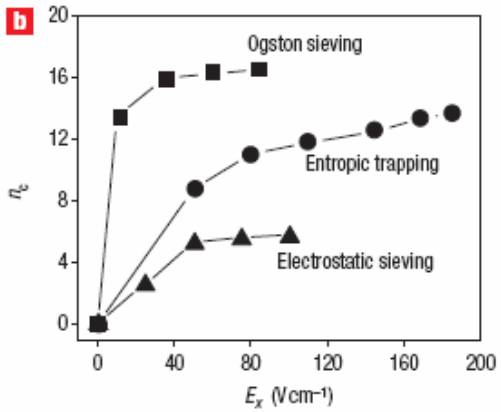
b
20
16
12
8
4
0
n_c
Ogston sieving
Entropic trapping
Electrostatic sieving
0
40
80
120
160
200
E_x (Vcm⁻¹)

Chapter 26
SPR/SERS

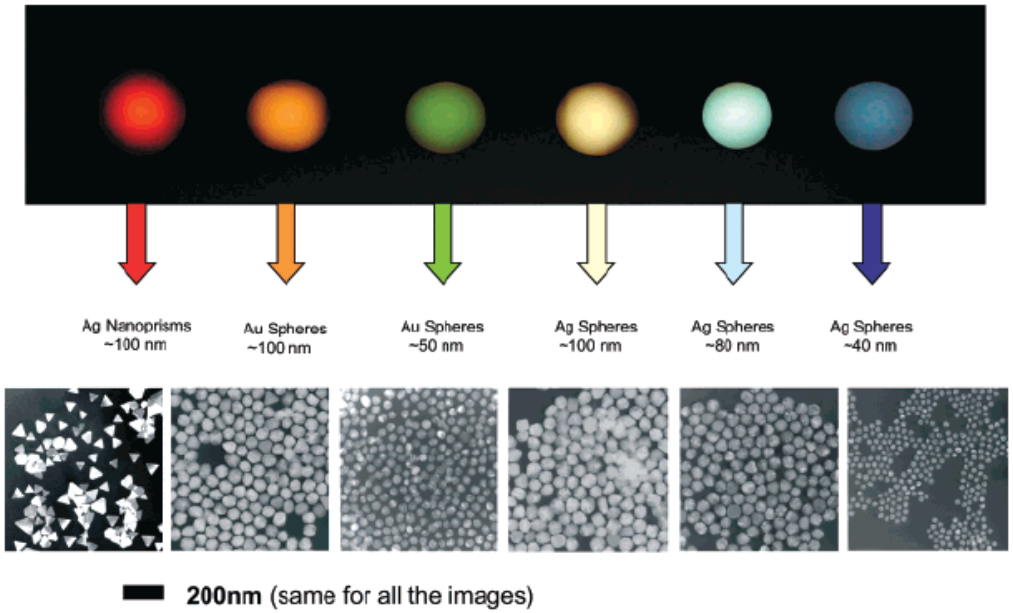

Figure 1. Sizes, shapes, and compositions of metal nanoparticles can be systematically varied to produce materials with distinct light-scattering properties.

Shape-Controlled Synthesis and Surface Plasmonic Properties of Metallic Nanostructures

MRS BULLETIN • VOLUME 30 • MAY 2005

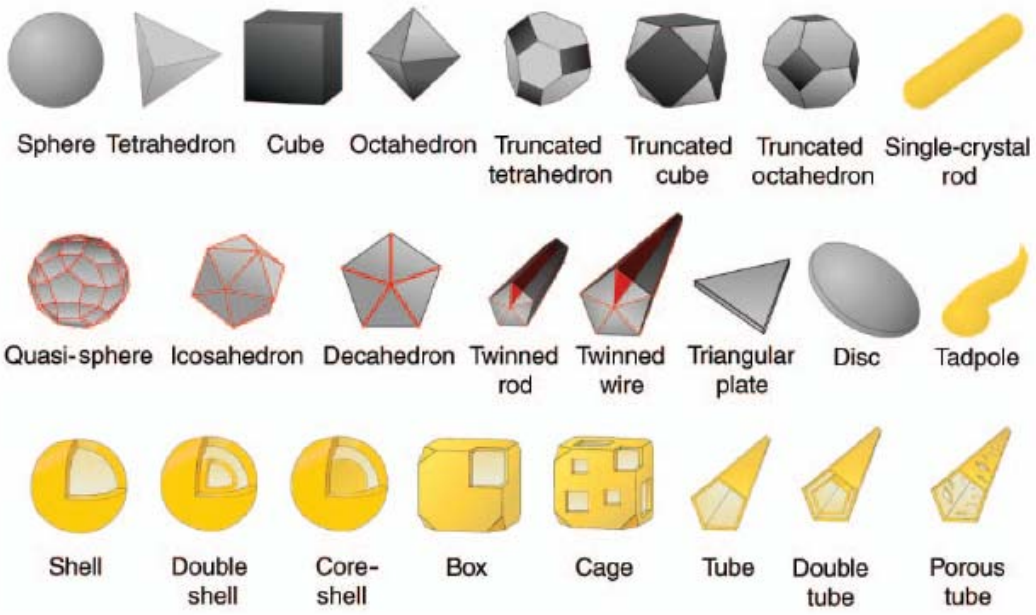

Figure 1. Schematic illustration of nanostructure shapes. The shapes in the top row are single crystals, in the second row are particles with twin defects or stacking faults, and in the third row are gold shells. All twinned and single-crystal shapes shown, with the exception of the octahedron, can be synthesized in solution. Control of shape allows control of optical and catalytic properties, as well as suitability for electronic applications in the case of wires, tubes, and possibly rods. Dark facets are (100) planes, light gray are (111) planes, and {111} twin planes are shown in red. Gold shapes represent gold particles, and gray shapes represent silver particles, although spheres, twinned rods, icosahedrons, and cubes can also be made from gold.

For a bulk metal with infinite sizes in all three dimensions, ω_p can be expressed as

$$\omega_p = (Ne^2/\varepsilon_0 m_e)^{1/2}, \quad (1)$$

where N is the number density of electrons, ε_0 is the dielectric constant of a vacuum, and e and m_e are the charge and effective mass of an electron, respectively. Quantized plasma oscillations are called *plasmons*.

Drift: Drude model

$$F = ma$$

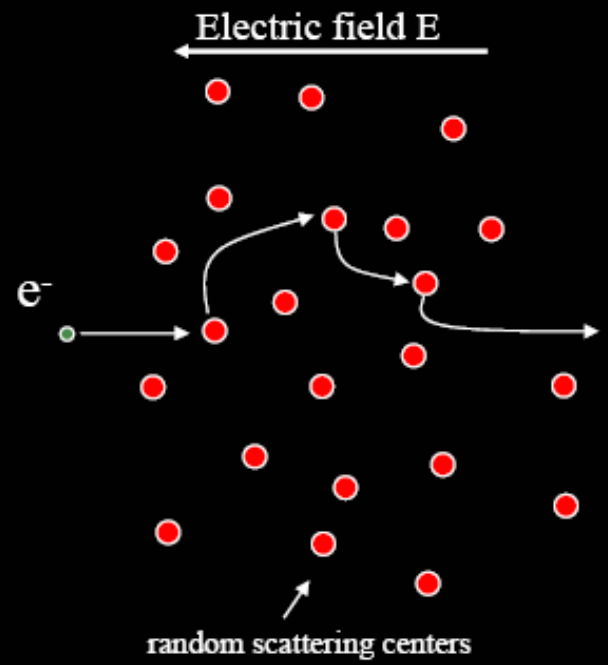

$$eE = m \frac{\partial v}{\partial t}$$

$$v_{avg} = \underbrace{\frac{e\tau}{m}}_{\mu} E$$

$$j = nev_{avg} = \underbrace{\frac{ne^2\tau}{m}}_{\sigma} E$$

$$m\frac{\partial}{\partial t}\langle \vec{v} \rangle = q\vec{E} - \gamma \langle \vec{v} \rangle$$

$$\sigma(\omega) = \frac{\sigma_0}{1 + i\omega\tau}$$

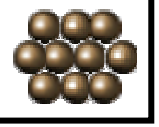

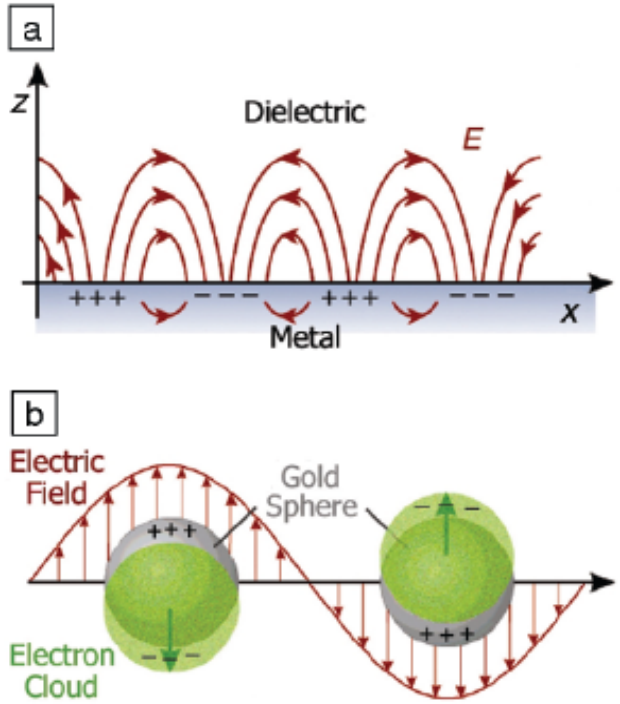

Figure 2. Schematic illustration of the collective oscillations of free electrons for (a) a metal–dielectric interface and (b) a spherical gold colloid. Excited by the electric field of incident light, the free electrons can be collectively displaced from the lattice of positive ions (consisting of nuclei and core electrons). While the plasmon shown in (a) can propagate across the surface as a charge density wave, the plasmon depicted in (b) is localized to each particle. (Courtesy of R. Van Duyne and T. Schatz, Northwestern University.)

Thin film
Nanoparticle
Nanoparticle array